

## Article

# Mechanical Characterization of Anhydrous Microporous Aluminophosphate Materials: Tridimensional Incompressibility, Ductility, Isotropy and Negative Linear Compressibility

Francisco Colmenero <sup>1,2,\*</sup> , Álvaro Lobato <sup>1</sup>  and Vicente Timón <sup>2</sup>

<sup>1</sup> Department of Chemical-Physics, Facultad de Ciencias Químicas, Universidad Complutense de Madrid, 28040 Madrid, Spain

<sup>2</sup> Instituto de Estructura de la Materia, Consejo Superior de Investigaciones Científicas, 28006 Madrid, Spain

\* Correspondence: francolm@ucm.es

**Abstract:** Here, a detailed mechanical characterization of five important anhydrous microporous aluminophosphate materials (VPI-5, ALPO-8, ALPO-5, ALPO-18, and ALPO-31) is performed using first principles methods based on periodic density functional theory. These materials are characterized by the presence of large empty structural channels expanding along several different crystallographic directions. The elasticity tensors, mechanical properties, and compressibility functions of these materials are determined and analyzed. All of these materials have a common elastic behavior and share many mechanical properties. They are largely incompressible at zero pressure, the compressibilities along the three crystallographic directions being frequently smaller than 5 TPa<sup>-1</sup>. Notably, the compressibilities of ALPO-5 and ALPO-31 along the three principal directions are smaller than this threshold. Likewise, the compressibilities of ALPO-18 along two directions are smaller than 5 TPa<sup>-1</sup>. All of the considered materials are shear resistant and ductile due to the large bulk to shear moduli ratio. Furthermore, all of these materials have very small mechanical anisotropies. ALPO-18 exhibits the negative linear compressibility (NLC) phenomenon for external pressures in the range  $P = 1.21$  to  $P = 2.70$  GPa. The minimum value of the compressibility along the [1 0 0] direction,  $k_a = -30.9$  TPa<sup>-1</sup>, is encountered for  $P = 2.04$  GPa. The NLC effect in this material can be rationalized using the empty channel structural mechanism. The effect of water molecule adsorption in the channels of ALPO-18 is assessed by studying the hydrated ALPO-18 material (ALPO-18W). ALPO-18W is much more compressible and less ductile than ALPO-18 and does not present NLC effects. Finally, the effect of aging and pressure polymorphism in the mechanical properties of VPI-5 and ALPO-5 is studied. As hydration, aging leads to significant variations in the elastic properties of VPI-5 and increases substantially its compressibility. For ALPO-5, pressure polymorphism has a small impact in its elasticity at zero pressure but a large influence at high pressure.

**Keywords:** mechanical properties; compressibility; isotropy; ductility; negative linear compressibility; anhydrous microporous aluminophosphate materials



**Citation:** Colmenero, F.; Lobato, Á.; Timón, V. Mechanical Characterization of Anhydrous Microporous Aluminophosphate Materials: Tridimensional Incompressibility, Ductility, Isotropy and Negative Linear Compressibility. *Solids* **2022**, *3*, 457–499. <https://doi.org/10.3390/solids3030032>

Academic Editor: John D. Clayton

Received: 21 June 2022

Accepted: 4 August 2022

Published: 16 August 2022

**Publisher's Note:** MDPI stays neutral with regard to jurisdictional claims in published maps and institutional affiliations.



**Copyright:** © 2022 by the authors. Licensee MDPI, Basel, Switzerland. This article is an open access article distributed under the terms and conditions of the Creative Commons Attribution (CC BY) license (<https://creativecommons.org/licenses/by/4.0/>).

## 1. Introduction

Aluminophosphate (ALPO) compounds are important synthetic microporous materials whose structure is characterized by the presence of large structural channels expanding along several different crystallographic directions [1]. Due to their high surface area and pore volume, ALPO materials have been employed in a wide range of important applications [1]. However, the full tensorial elasticity of these compounds, determining their behavior under stress and their mechanical performance in the applications, have surprisingly not been studied. A detailed mechanical characterization of a representative set of ALPO materials is performed in the present work. The set of materials considered

includes VPI-5 [2–5], ALPO-8 [6,7], ALPO-5, [8,9] ALPO-18 [10,11], and ALPO-31 [12]. Specifically, the ALPO materials studied in this paper have been extensively used for compound adsorption [13–23], encapsulation [13,18,24–26] and separation [27–29], synthesis and catalysis [30–44], sensor fabrication [45], and energy storage and heat transformation applications [46–49]. The most widely used ALPO material is ALPO-5, a highly versatile material [14,18,19,23–26,30–36,40,45] which is very well-known for its applications in the encapsulation of laser dyes [18,24] and as a host for the formation of single-walled carbon nanotubes [30–36]. The range of applicability of aluminophosphate microporous solids is being greatly extended from the well-known fields of absorption, catalysis, and ion exchange. Important applications investigate their potential use as catalysts in the manufacture of chemicals, for increasingly selective acid and oxidation catalysis, in biomedical applications as drug delivery, in devices that require special electronic or optical properties, and as advanced functional materials [1].

The mechanical properties of natural and synthetic materials exhibiting high porosity are extremely interesting from the point of view of applications, three important examples being those of zeolites [50–67], metal organic frameworks (MOF) [68–103], and 3D carbon (3DC) materials [104–116]. Since their mechanical properties vary substantially from one compound to other, they have a large spectrum of applications. Interesting enhanced mechanical characteristics found for these materials include increased flexibility [21,29,32,34,37,57–62] and responsible behavior upon guest molecule adsorption and under temperature and pressure perturbations [56,57,67,69,76,98,99,110,111,117–128]. These properties make these materials exceptionally appropriate for mechanical damping and mechanical energy storage [55,84–86,91,114,115,120], compound adsorption [70,98,99,110,111,117–122], separation and storage [113,123,124], drug-delivery [125], and sensing applications [45,116,120]. Furthermore, negative [64,71,73,74,77–79,92–101] or zero [55] linear compressibility and negative [51,54,65,66,74,83,100] or zero [100] Poisson's ratio phenomena have been encountered for many of these materials. The negative-linear compressibility (NLC) [129–131], zero linear compressibility (ZLC) [132–135] and negative Poisson's ratio phenomena (NPR) [136–139] have multiple potential applications [129,131,133–135,139–148], the most well-known being the development of ultrasensitive pressure sensors and actuators [129,139,140]. The relevance of the research on the behavior of highly porous materials under the effect of pressure in materials science has further increased since the application of high pressures to this type of materials has allowed for the design of new advanced functional materials, thus expanding the limits of conventional synthetic chemistry. Interesting amorphous materials, glasses, and crystalline compounds have been obtained from pressure induced phase transitions and structural rearrangements [149–164].

The enormous amount of research devoted to the synthesis and characterization of the microporous aluminophosphate materials by X-ray, neutron and synchrotron diffraction, NMR, and spectroscopic techniques and to the study of their thermal stability, thermodynamic, and general physical and chemical properties is strongly in contrast with the poor current mechanical characterization of these materials [165–172]. As far as we know, only the compressibility and phase transitions induced by the application of isotropic pressures in ALPO-5 [167], VPI-5 [168–170] and ALPO-17 [171,172] have been studied. Therefore, the number of ALPO materials whose elasticity has been investigated is very small and the only mechanical property considered is the compressibility. Although these studies provided interesting results, the understanding of the mechanics of these materials is strongly deficient. The importance of the knowledge of tensorial elastic properties of porous materials is well-known in Earth sciences, where the effect of porosity on the elasticity of rocks and minerals is an important topic of direct interest for applications in petroleum exploration and production [173–178], clay swelling and radioactive nuclear waste storage [179–188], and for characterizing mechanical instabilities as shear failures [183–188]. Knowledge of the full elastic tensor is fundamental for assessing the mechanical stability of a given material or structure [189–192]. In materials science and technology, mechanical engineering, the phar-

maceutical industry, and many other branches of science [193–240], the knowledge of the anisotropic mechanical properties, including the Young and shear moduli, Poisson's ratio, and elastic anisotropy measures, is fundamental for the assessment of many important properties of materials, composites and products as their hardness [193–197] ductility [198–204], anisotropy [205–212] shear strength [74,82,215–217,225–227] compaction, tableting and milling performance [88,217,218,221,222,227,234,235], durability and degradability [207,208,238,239], and for the material screening and selection [217–223,228,239,240]. As shown in this paper, the mechanical properties of different polymorphic forms of the same ALPO material vary significantly. The knowledge of the elastic properties of the different polymorphic forms of a given material is important for selecting the polymorph with the best performance for a given application [217–223,226–231,234,236,237]. For microporous materials, the importance of the analysis of the full tensorial elasticity has been highlighted by the study of the mechanical stability and mechanical properties of selected zeolites [51,54,60,61,64–66,241–243] and MOFs [73,74,80,81,83,90,100,101]. A wide range of experimental methods, complementary to the use of diamond anvil cells (DAC) under hydrostatic pressures, such as elastic wave propagation measurements [244–247], the inelastic X-ray scattering [242,243,248–251], Brillouin scattering [53,54,252,253], nanoindentation [68,80,81,83,220,224,229–231,254–259] and ellipsometry [81,260] techniques, impedance spectroscopy [261–264], real contact area measurements [265], or methods based on DAC with non-hydrostatic pressures [168,264–270] could be used to provide a more complete set of mechanical properties of ALPO materials. These techniques have already been used in some cases for zeolites and MOFs [53,54,68,80,81,241,254]. Alternatively, force field [51,52,65,90,243,271–273] or accurate first principles methods [60,61,64–66,68,71,87,100,101,264,274–276] could be employed. First-principles calculations based on density functional theory represent a versatile, efficient, and accurate method for calculating the mechanical properties of materials [60,61,100,101,264,270,277].

In the present work, first principles solid-state methodology is employed to determine the mechanical properties and compressibility functions of ALPO materials. From a physical point of view, the increase in porosity in a given material should reduce its bulk and shear moduli and isotropy, making the material weaker, more compressible, and less shear resistant. However, these expectations are largely unsatisfied in many cases and the mechanics of porous materials is highly variable. In the present work, anhydrous ALPO compounds are surprisingly found to be very incompressible, ductile, and isotropic materials. The ductility of these materials results from the high bulk to shear moduli ratios [198,200], even although the shear moduli are quite significant. The incompressibility, ductility, and isotropy of the anhydrous ALPO materials could make them advantageous in many practical applications with respect to other more compressible, brittle, or anisotropic materials due to their larger stability and controllability under operation. However, these characteristics are shown to be highly dependent on the pressure and humidity conditions and material aging. In recent works [100,101], the negative linear compressibility phenomenon was found in some microporous metal organic frameworks due to the presence of empty structural channels in their crystal structures. In these materials, the widening of the channels along the direction of minimum compressibility under the effect of pressure leads to an increase of the dimension of the crystal along this direction. This effect, however, could or could not be found in multi-channel materials due to compensation effects associated with the distinct compressional behavior of the different channels along the several crystallographic directions. However, the present results show that the NLC phenomenon is indeed observed in ALPO-18 material in which the compressional behavior of its largest channels is dominant and leads to a substantial NLC effect along the [1 0 0] crystallographic direction.

## 2. Methods

The mechanical properties and compressibility functions of the ALPO materials studied [2–12], were determined using first principles solid-state methods based on periodic density functional theory, employing plane wave basis sets and pseudopotential functions

for the description of the inner atomic electrons [278]. All of the computational works were carried out utilizing the Cambridge Serial Total Energy Program (CASTEP) computer code [279] interfaced with the Materials Studio program suite [280]. The main energy-density functional used in this work was the specialized version of Perdew-Becke-Ernzerhof (PBE) functional [281] for solid materials, PBEsol [282]. The PBE functional supplemented with D2 Grimme empirical correction [283] was also employed to assess the importance of the dispersion interactions in the structures and elastic properties of the selected ALPOs and for the description of ALPO-18 hydrated material (ALPO-18W) [11]. The good performance of PBEsol functional for anhydrous materials is well documented [284–290]. The pseudopotential functions utilized in this work were norm-conserving pseudopotentials [291] provided by the CASTEP program. Further computational details and material data of the compounds studied are given in Table S1 of the Supplementary Materials (SM). The Broyden–Fletcher–Goldfarb–Shanno (BFGS) method [292] was employed to optimize completely all of the atomic positions and unit cell parameters of the studied materials. The crystal structure optimizations were carried out, using the experimental structures as starting point, with stringent convergence criteria. The thresholds in the variation of the total energy, maximum atomic force, maximum atomic displacement and maximum stress are  $2.5 \times 10^{-6}$  eV/atom, 0.005 eV/Å,  $2.5 \times 10^{-4}$  Å, and 0.0025 GPa, respectively. The software REFLEX included in the Materials Studio program package [279] was used to derive the X-ray powder diffraction patterns [293] of the selected ALPOs from the experimental and computed crystal structures using  $\text{CuK}\alpha$  radiation ( $\lambda = 1.540598$  Å).

The elastic constants, the matrix elements of the stiffness tensor [294], needed to calculate the mechanical properties of the materials considered and to study the mechanical stability of their crystal structures, were determined from stress-strain relationships using the finite deformation method (FDM) [295]. The theory of elasticity in solid state physics, is a mathematically well-defined theory which relies on the quantum mechanical definition of the stress tensor [296]. In the FDM, the individual elastic constants are determined from the stress tensors resulting from the response of the material to finite programmed symmetry-adapted strains [295]. The FDM has been satisfactorily utilized to describe the elastic response of many solid materials, including uranyl-containing compounds [286,288,289,297–306], organic crystals [307–311], and metal-organic compounds [100,101,290,312–314]. The reliability of this method has been confirmed recently by the experimental verification of the negative area compressibility effect in silver oxalate [314] which was predicted using the first principles methodology [313]. The full set of elastic constants can also be computed using other methods [315–323] such as density functional perturbation theory (DFPT) [315–318] or the well-known strain or stress fluctuation formalisms from both Monte Carlo and molecular dynamics simulations [319–323]. The ELAM computer program [324] was employed to generate the tridimensional representations of the mechanical properties as a function of the orientation of the applied strain.

### 3. Results and Discussion

#### 3.1. Crystal Structures

The computed crystal structures of VPI-5, ALPO-8 and ALPO-31 are shown in Figure 1 and the structures of ALPO-18 and ALPO-18W are displayed in Figure 2. The structure of VPI-5 [2–5], consists of alternating  $\text{AlO}_4$  and  $\text{PO}_4$  tetrahedra [325] which share vertices to form four- and six-membered rings (4-MR and 6-MR). The four- and six-membered rings are linked together in the (0 0 1) plane to form exceptionally large hexagonal 18-membered rings (18-MR) with horizontal and vertical dimensions  $\omega = 13.84$  Å and  $h = 15.84$  Å measured as the distances between opposite oxygen atoms (see Figure 1A) These rings delimitate empty structural channels expanding along [0 0 1], the 18-MR channels having hexagonal cross-sections. The corresponding horizontal and vertical pore apertures for the 18-MR channels can be obtained by discounting two times the oxygen ionic radii ( $R(\text{O}) = 1.33$  Å),  $p_\omega = 11.2$  Å, and  $p_h = 13.2$  Å.

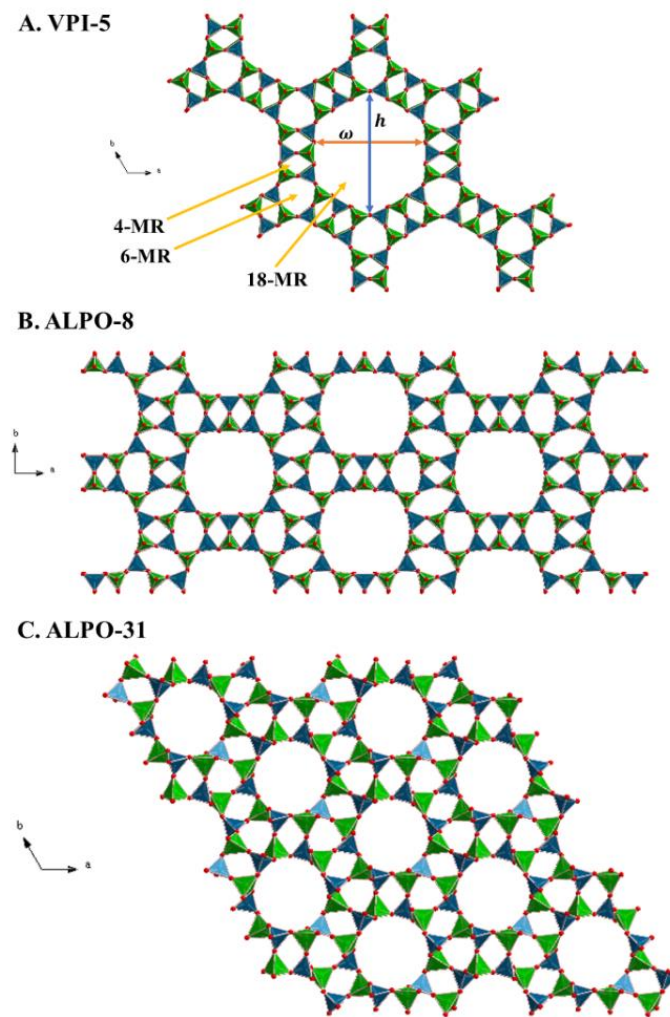


**Figure 1.** Views of crystal structures of (A) VPI-5; (B) ALPO-8; and (C) ALPO-31 from  $[0\ 0\ 1]$ . The images show  $2 \times 2 \times 2$  supercells of each material. Color code: Al-Green; P-Blue; O-red.

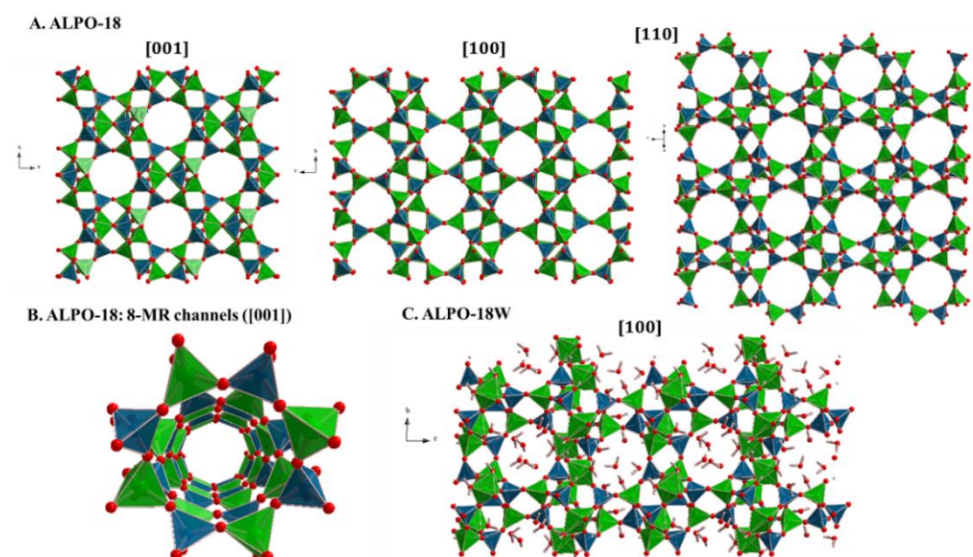


**Figure 2.** Views of the crystal structures ( $2 \times 2 \times 2$  supercells) of ALPO-18 and ALPO-18W: (A) ALPO-18 from  $[0\ 0\ 1]$ ,  $[1\ 0\ 0]$  and  $[1\ 1\ 0]$ ; (B) Perspective view of the 8-MR channels expanding along  $[0\ 0\ 1]$ ; (C) ALPO-18W from  $[1\ 0\ 0]$ . Color code: Al-Green; P-Blue; O-red.

The crystal structure of ALPO-8 [6,7], is formed by alternating corner sharing  $\text{AlO}_4$  and  $\text{PO}_4$  tetrahedra forming 4-, 6- and 14-membered rings as shown in Figure 1B. The 14-membered rings have a distorted rectangular shape and have horizontal and vertical dimensions of  $\omega = 11.40 \text{ \AA}$  and  $h = 10.55 \text{ \AA}$  (pore apertures of 8.7 and 7.9  $\text{ \AA}$ ). VPI-5 and ALPO-8 belong to a group of molecular sieves with framework structures containing very large channels. The term “extra-large pore” material was coined by Davis et al. [326] to specify microporous materials having channels with apertures larger than those of the classical 12-MR rings. ALPO-31 [12] contains one-dimensional channels circumscribed by 4-, 6- and 12-tetrahedrally coordinated atoms, that is, 4-, 6- and 12-membered rings in  $[0\ 0\ 1]$  plane (Figure 1C), the latter being nearly circular and having a diameter of  $d = 7.9 \text{ \AA}$  (pore aperture  $p_d = 5.2 \text{ \AA}$ ). ALPO-5,8-9 as ALPO-31, contains 4-, 6- and 12-MR channels expanding along  $[0\ 0\ 1]$ , the latter having a nearly circular cross section with a diameter of  $d = 10.1 \text{ \AA}$  (pore aperture  $p_d = 7.4 \text{ \AA}$ ).

As shown in Figure 2A, the structure of ALPO-18 [10,11] exhibits 4- and 8-membered rings in  $(0\ 0\ 1)$  plane. The 8-membered nearly circular rings, have a diameter of  $d = 6.5 \text{ \AA}$ . A perspective view of the 8-MR channels is plotted in Figure 2B. The ALPO materials have commonly also channels expanding along several directions. While these channels have generally smaller apertures, the case of ALPO-18 is noticeable since also large channels are observed when the material is viewed from other directions. As can be observed in the second and third subfigures of Figure 2A, large 8-membered rings are also observed when the structure of ALPO-18 is seen from  $[1\ 0\ 0]$  and  $[1\ 1\ 0]$  directions. Figure 2C shows the crystal structure of hydrated ALPO-18 (ALPO-18W). Two water molecules per formula unit are adsorbed within the channels of ALPO-18. The structure of ALPO-18 changes significantly upon hydration. The space symmetry of this material changes from monoclinic ( $C2/c$ ) to triclinic ( $P1$ ). In fact, some of the aluminum atoms change their coordination environment from tetrahedral to octahedral to account for the presence of additional water molecules [11].

The computed lattice parameters for VPI-5, ALPO-8, ALPO-5, ALPO-18, ALPO-18W, and ALPO-31 along with the experimental parameters are reported in Table 1. The average difference of the computed and experimental unit cell volumes is quite good, 2.5 and 2.3%, for the PBE and PBEsol functionals. The impact of introduction of dispersion corrections in these materials is relatively small and the average difference of the computed and experimental unit cell volumes is reduced by only 0.3%. Since the improvement due to the inclusion of dispersion corrections was small, the PBEsol functional was used for all anhydrous materials to retain the ab initio character of the computations. Additional details about the impact of including dispersion interactions in the calculations will be given in Section 3.6.3. Dispersion corrections were only included for ALPO-18W since, as it is well-known [100,288–290], they significantly improve the hydrogen bond geometries in the structures of hydrated materials. The X-ray diffraction patterns of VPI-5, ALPO-8, ALPO-5, ALPO-18, and ALPO-31, generated from the computed and experimental structures [4,6,9,10,12], are compared in Figure 3. The agreement is excellent. A detailed comparison of the positions of the main reflections in the X-ray diffraction patterns for these ALPO materials is provided in Tables S2–S6 of the SM. Similarly, Tables S7–S11 of the SM provide a comparison of the computed and experimental interatomic distances in the crystal structures of these materials. The computed PO and AlO average distances are 1.52 and 1.72  $\text{ \AA}$ , respectively, which are in good agreement with the experimental values of 1.51 and 1.70  $\text{ \AA}$ .

**Table 1.** Computed and experimental unit-cell parameters of the selected aluminophosphate materials.

Parameter	$a$ (Å)	$b$ (Å)	$c$ (Å)	$\alpha$ (deg)	$\beta$ (deg)	$\gamma$ (deg)	Vol. (Å <sup>3</sup> )	$\rho$ (g/cm <sup>3</sup> )
<b>VPI-5 (<i>P6<sub>3</sub>cm</i>)</b>								
PBE	18.5665	18.5665	8.5330	90.0	90.0	120.0	2547.3630	1.431
PBE + Disp	18.5253	18.5253	8.5234	90.0	90.0	120.0	2533.2330	1.439
PBEsol	18.5430	18.5430	8.5398	90.0	90.0	120.0	2542.9495	1.433
Exp [4]	18.6005(6)	18.6005(6)	8.3664(4)	90.0	90.0	120.0	2506.7931	1.455
<b>ALPO-8 (<i>Cmc2<sub>1</sub></i>)</b>								
PBE	33.5899	14.7280	8.5334	90.0	90.0	90.0	4221.5557	1.727
PBE + Disp	33.3954	14.6915	8.5222	90.0	90.0	90.0	4181.1994	1.744
PBEsol	33.5175	14.7223	8.5398	90.0	90.0	90.0	4213.9746	1.730
Exp [6]	33.29(2)	14.76(2)	8.257(4)	90.0	90.0	90.0	4057.1628	1.797
<b>ALPO-5 (<i>P6cc</i>)</b>								
PBE	13.8671	13.8671	8.5350	90.0	90.0	120.0	1421.3670	1.710
PBE + Disp	13.8401	13.8401	8.5261	90.0	90.0	120.0	1414.3565	1.718
PBEsol	13.8645	13.8645	8.5382	90.0	90.0	120.0	1421.3642	1.710
Exp [9]	13.718(1)	13.718(1)	8.4526(5)	90.0	90.0	120.0	1377.5347	1.765
<b>ALPO-18 (<i>C2/c</i>)</b>								
PBE	13.5704	12.6773	18.4699	90.0	90.01	90.0	3177.4870	1.529
PBE + Disp	13.5561	12.6613	18.4442	90.0	90.02	90.0	3165.7084	1.535
PBEsol	13.5788	12.6705	18.4592	90.0	90.01	90.0	3175.9001	1.530
Exp [10]	13.7114(1)	12.7314(1)	18.5703(1)	90.0	90.01(1)	90.0	3241.7302	1.500
<b>ALPO-18 W (<i>P1</i>)</b>								
PBE	9.3276	9.4113	18.3376	88.24	91.77	88.97	1607.9391	1.957
PBE + Disp	9.2582	9.3513	18.2448	87.99	91.81	89.32	1577.6793	1.995
PBEsol	9.2487	9.3723	18.2507	88.66	91.93	88.54	1580.1187	1.992
Exp [11]	9.251	9.362	18.428	90.89	96.35	90.87	1585.7971	1.985
<b>ALPO-31 (<i>R3h</i>)</b>								
PBE	20.9724	20.9724	5.0778	90.0	90.0	120.0	1934.2242	1.884
PBE + Disp	20.9230	20.9230	5.0683	90.0	90.0	120.0	1921.5046	1.897
PBEsol	20.9635	20.9635	5.0767	90.0	90.0	120.0	1932.1567	1.886
Exp [12]	20.827(1)	20.827(1)	5.003(1)	90.0	90.0	120.0	1879.3798	1.940

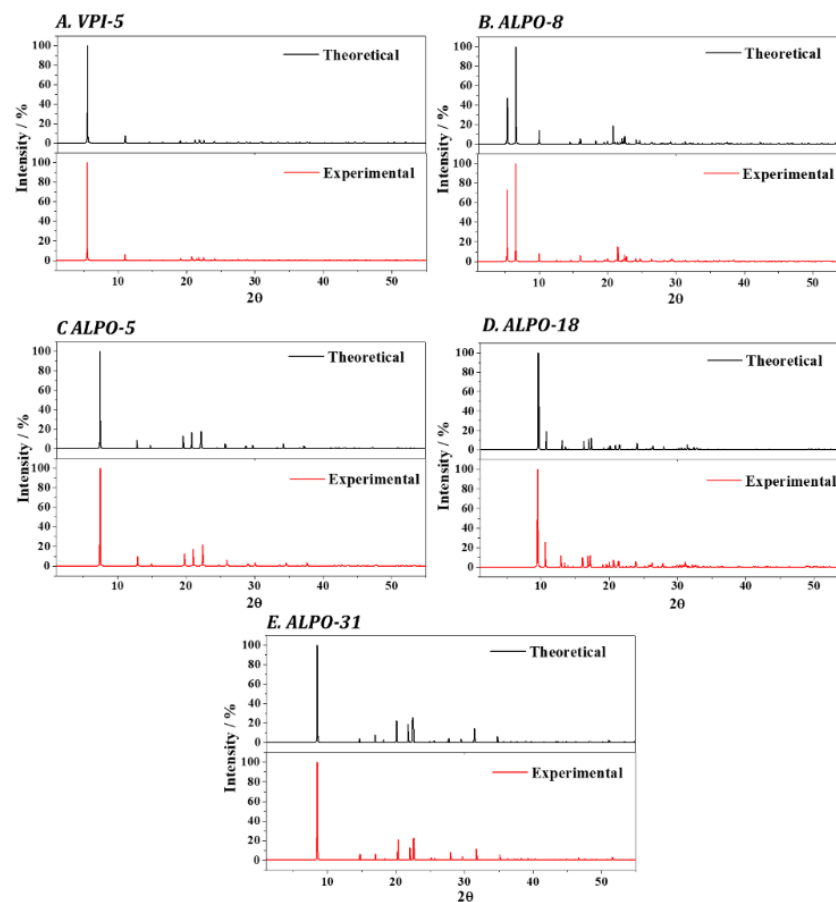


**Figure 3.** X-ray diffraction patterns of (A) VPI-5; (B) ALPO-8; (C) ALPO-5; (D) ALPO-18; and (E) ALPO-31, derived from the computed and experimental [4,6,9,10,12] crystal structures using  $\text{CuK}\alpha$  radiation ( $\lambda = 1.540598 \text{ \AA}$ ).

### 3.2. Stiffness Tensors and Mechanical Stability

The computed stiffness tensors of VPI-5, ALPO-8, ALPO-5, ALPO-18 and ALPO-31 are provided in Table 2. The number of non-vanishing and non-equivalent elements in the matrix representation of the symmetric stiffness tensor depends on the space symmetry of the corresponding crystal structure [192,325]. The  $P6_3cm$  and  $P6cc$  structures of VPI-5 and ALPO-5 are hexagonal and have nine non-vanishing elastic constants in their stiffness matrices, five of which are non-equivalent ( $C_{11}, C_{33}, C_{44}, C_{12}, C_{13}$ ). ALPO-8 is orthorhombic ( $Cmc2_1$ ) and, therefore, its stiffness tensor has nine non-vanishing elements all of which are non-equivalent. The number of nonvanishing elastic constants for the monoclinic structure of ALPO-18 ( $C2/c$ ), increases to thirteen due to its lower symmetry. For ALPO-31 (trigonal,  $R\bar{3}h$ ) there are fifteen non-vanishing elastic constants, seven of which are non-equivalent ( $C_{11}, C_{33}, C_{44}, C_{12}, C_{13}, C_{14}, C_{15}$ ). A crystal structure is mechanically stable, if and only if, the Born mechanical stability conditions are fulfilled [189–192]. The generic Born mechanical stability condition can be written in mathematical form as an algebraic condition on the eigenvalues of the matrix representation of the stiffness tensor: the elastic matrix must be positive definite, that is, all its eigenvalues must be greater than zero [192]. A numerical diagonalization of the stiffness tensors of all of the ALPO materials was carried out. Since all of the elastic matrix eigenvalues for all materials were positive, they are mechanically stable.

**Table 2.** Computed elastic constants of selected aluminophosphate materials. All of the values are given in GPa.

<i>ij</i>	$C_{ij}$				
	VPI-5 <i>P6<sub>3</sub>cm</i>	ALPO-8 <i>Cmc2<sub>1</sub></i>	ALPO-5 <i>P6<sub>cc</sub></i>	ALPO-18 <i>C2/c</i>	ALPO-31 <i>R3h</i>
11	85.17	82.23	124.23	105.68	109.15
22	85.17	102.00	124.23	98.33	109.15
33	158.27	187.62	192.56	105.82	138.05
44	19.10	23.94	26.24	13.99	30.81
55	19.10	25.96	26.24	18.71	30.81
66	21.79	23.35	28.22	28.90	23.01
12	41.59	53.01	67.80	68.62	63.13
13	43.66	48.05	59.70	57.17	61.58
14	0.0	0.0	0.0	0.0	5.76
15	0.0	0.0	0.0	−2.42	0.46
16	0.0	0.0	0.0	0.0	0.0
23	43.66	51.17	59.70	52.13	61.58
24	0.0	0.0	0.0	0.0	−5.76
25	0.0	0.0	0.0	−1.73	−0.46
26	0.0	0.0	0.0	0.0	0.0
34	0.0	0.0	0.0	0.0	0.0
35	0.0	0.0	0.0	3.16	0.0
36	0.0	0.0	0.0	0.0	0.0
45	0.0	0.0	0.0	0.0	0.0
46	0.0	0.0	0.0	−1.21	−0.46
56	0.0	0.0	0.0	0.0	5.76

### 3.3. Mechanical Properties

The computed stiffness tensors were employed to determine the mechanical properties of polycrystalline aggregates of the considered ALPO materials using the Voigt [327], Reuss [328] and Hill [329] schemes. The corresponding formulas for these approximations may be found in several sources (for example, Weck et al. [330]). The results obtained using the three approaches were quite similar for all materials. As was found in many previous papers [100,101,286,288,290,298–313,331], the values of the calculated bulk moduli in the Reuss approximation gave the best approximation to the single crystal bulk moduli of these materials. The mechanical properties for VPI-5, ALPO-8, ALPO-5, ALPO-18 and ALPO-31 in the Reuss approximation are given in Table 3. As can be observed, these five materials are characterized by very small elastic anisotropies, since the universal anisotropy indices ( $A^U$ ) [212] are 0.66, 0.83, 0.49, 0.46, and 0.36, respectively. The similarity of the computed mechanical properties in the Voigt, Reuss, and Hill approximations is a direct consequence of the low mechanical anisotropy. For crystalline systems with strong anisotropy, large differences should be expected [286,330,331]. The single-crystal bulk moduli,  $B^{sc}$ , reported in Table 3, were not determined from fits of calculated pressure-volume data to high-order Birch-Murnaghan equations of state [332], as was customary in previous works [100,101,286,288,290,298–313,331], since the fitting parameters were rather dependent on the range of pressure employed. Similar difficulties were found in the study of the compressibility of several minerals [333]. The computed bulk moduli were derived from the compressibility functions reported in Sections 3.5 and 3.6, which were determined from accurate six order polynomial fits to pressure-volume data in the pressure range from 0 to 5 GPa.

**Table 3.** Computed mechanical properties of selected aluminophosphate materials. The values of the bulk, shear and Young's moduli ( $B$ ,  $G$  and  $E$ ) are given in in GPa. The single-crystal bulk moduli ( $B^{sc}$ ) are also given in the last row of the table for comparison.

Property		VPI-5 <i>P6<sub>3</sub>cm</i>	ALPO-8 <i>Cmc2<sub>1</sub></i>	ALPO-5 <i>P6cc</i>	ALPO-18 <i>C2/c</i>	ALPO-31 <i>R3h</i>
$B$	Bulk modulus	60.49 ± 0.56	68.27 ± 0.87	88.22 ± 0.60	73.56 ± 0.95	80.17 ± 1.16
$G$	Shear modulus	22.67	25.56	30.24	19.34	26.41
$E$	Young's modulus	60.46	68.18	81.43	53.35	71.39
$\nu$	Poisson's ratio	0.33	0.33	0.35	0.38	0.35
$D$	Ductility index	2.66	2.67	2.92	3.80	3.04
$D^I$	Intrinsic ductility index	0.37	0.43	0.51	1.02	0.45
$H$	Hardness index	0.94	1.22	1.13	0.63	0.70
$A^U$	Universal anisotropy	0.66	0.83	0.49	0.46	0.36
$B^{sc}$	Bulk modulus (SC)	60.74 ± 0.81	72.60 ± 0.42	87.27 ± 1.36	73.85 ± 2.92	90.14 ± 1.56

The computed values of the bulk modulus,  $B$ , the inverse of compressibility, are significant: 60.49, 68.27, 88.22, 73.56, and 80.17 GPa for VPI-5, ALPO-8, ALPO-5, ALPO-18 and ALPO-31, respectively. This means that these materials are very incompressible under the effect of external isotropic pressures. ALPOs are also resistant with respect to the application to uniaxial pressures since the values of the Young's moduli, 60.46, 68.18, 81.43, 53.35, 71.39 GPa, respectively, are substantial. The shear modulus,  $G$ , represents the resistance to plastic deformation. The calculated values of  $G$ , 22.67, 25.56, 30.24, 19.34, and 26.41 GPa, respectively, are quite large in comparison with the values found for other microporous materials [53,54,64,66,72–75,80–82,100]. Therefore, ALPOs are resistant with respect to the application of external uniform and uniaxial pressures and shear stresses.

The Cauchy pressure term, defined in terms of the elastic constants as  $CP = (C_{11} - C_{44})$ , was proposed by Pettifor [199] as an indicator of the angular character of atomic bonding. The values of  $CP$  are positive and large, 22.49, 29.07, 41.56, 54.63, and 32.32 GPa, for VPI-5, ALPO-8, ALPO-5, ALPO-18, and ALPO-31, respectively, reflecting a largely angular bonding in these materials. The value of the Cauchy pressure term is particularly large for ALPO-18.  $CP$  is also related with the brittle/ductile character of crystals [198,200–204]. Large values of  $CP$  are associated with highly ductile materials. The ductility index,  $D = B/G$ , was proposed by Pugh [198], as a standard measure of the ductility of a material. A value of  $D = 1.75$ , separates the brittle and ductile materials [201,208]. All of the computed values of  $D$ , 2.66, 2.67, 2.92, 3.80, and 3.04, for VPI-5, ALPO-8, ALPO-5, ALPO-18, and ALPO-31, respectively, are much larger than 1.75. Therefore, the five materials are ductile. An improved ductility criterium has been provided recently by Niu et al. [200]. In their work, these authors noticed that the intrinsic ductility index, defined as the ratio of the Cauchy pressure term to the Young's modulus,  $D^I = (C_{11} - C_{44})/E$ , is strongly correlated hyperbolically with the Pugh's ratio. As shown in Table 3, the values obtained for the intrinsic ductility index for the ALPO materials considered ranges from 1.02 to 0.18 and are in the same range as that for common metals [200]. The value of  $D^I$  for ALPO-18, 1.02, is close to that of Pt ( $0.98 \pm 0.01$ ) or Nb ( $1.00 \pm 0.01$ ). For ALPO-5,  $D^I = 0.51$ , coincides with that of K ( $0.51 \pm 0.01$ ). The intrinsic ductility indices of ALPO-31 and ALPO-8, 0.45, and 0.43, respectively, are close to the ductility for Al ( $0.44 \pm 0.04$ ). Finally, the value of  $D^I$  for VPI-5, 0.37, is near to that of Cu ( $0.38 \pm 0.04$ ).

The Vickers hardness ( $H$ ) measures the resistance of a given material to indentation. A series of representative values of  $H$  for interesting materials may be obtained from several published papers [193–197]. As a reference, talc and halite ( $H = 0.26$  and  $0.30$ ) are very weak, calcite and sphalerite ( $H = 1.5$  and  $1.8$ ) are weak, fluorite and apatite ( $H = 3.0$  and  $5.1$ ) have medium hardness, quartz and zirconia ( $H = 11.1$  and  $13.0$ ) are hard and corundum and diamond ( $H = 21.5$  and  $96.0$ ) are very hard. The computed values of  $H$  for VPI-5,

ALPO-8, ALPO-5, ALPO-18, and ALPO-31 are 0.94, 1.22, 1.13, 0.63, and 0.70, respectively, which correspond to relatively weak materials.

### 3.4. Mechanical Properties as a Function of the Orientation of the Applied Strain

In the previous subsection, a general view of the elasticity of the ALPO materials was achieved and average values of the elastic moduli, Poisson's ratios, and ductility, hardness, and elastic anisotropy indices were reported. A more detailed understanding of the elasticity of these materials is provided by the analysis of the variation of the mechanical properties with the strain orientation. Three dimensional representations of the dependence of the elastic moduli and Poisson's ratios for VPI-5, ALPO-8, ALPO-5, ALPO-18 and ALPO-31 with respect to the direction of the applied strain are displayed in Figures 4–8, respectively. These figures explain the low elastic anisotropy of these materials since all elastic moduli have a smooth variation with respect to the direction of the applied strain. The elastic properties of VPI-5 and ALPO-5 (with hexagonal space symmetries) show a nice orientational dependence which is axially symmetric around  $z$  axis.

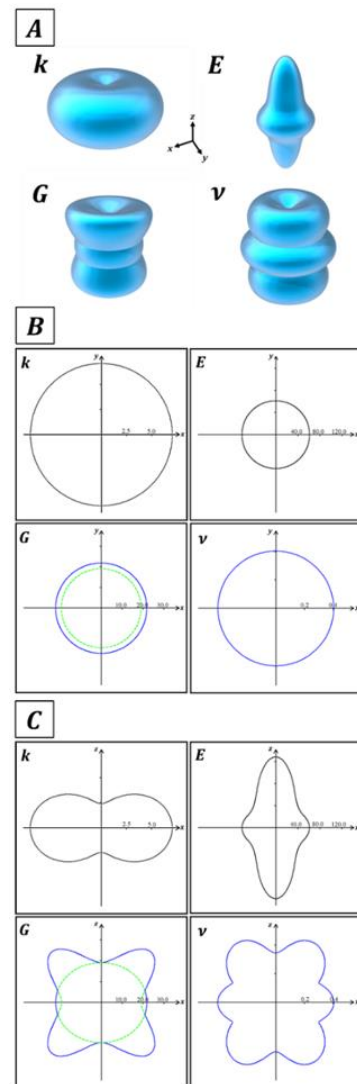


**Figure 4.** (A) Mechanical properties of VPI-5 ( $P6_3cm$ ) as a function of the orientation of the applied strain:  $k$ -compressibility,  $E$ -Young modulus,  $G$ -Maximum shear modulus, and  $\nu$ -Maximum Poisson's ratio; (B) bidimensional projections on the  $xy$  plane; (C) bidimensional projections on the  $xz$  plane. The projections of the surface of minimum shear modulus are also displayed using green color in panels (B,C).

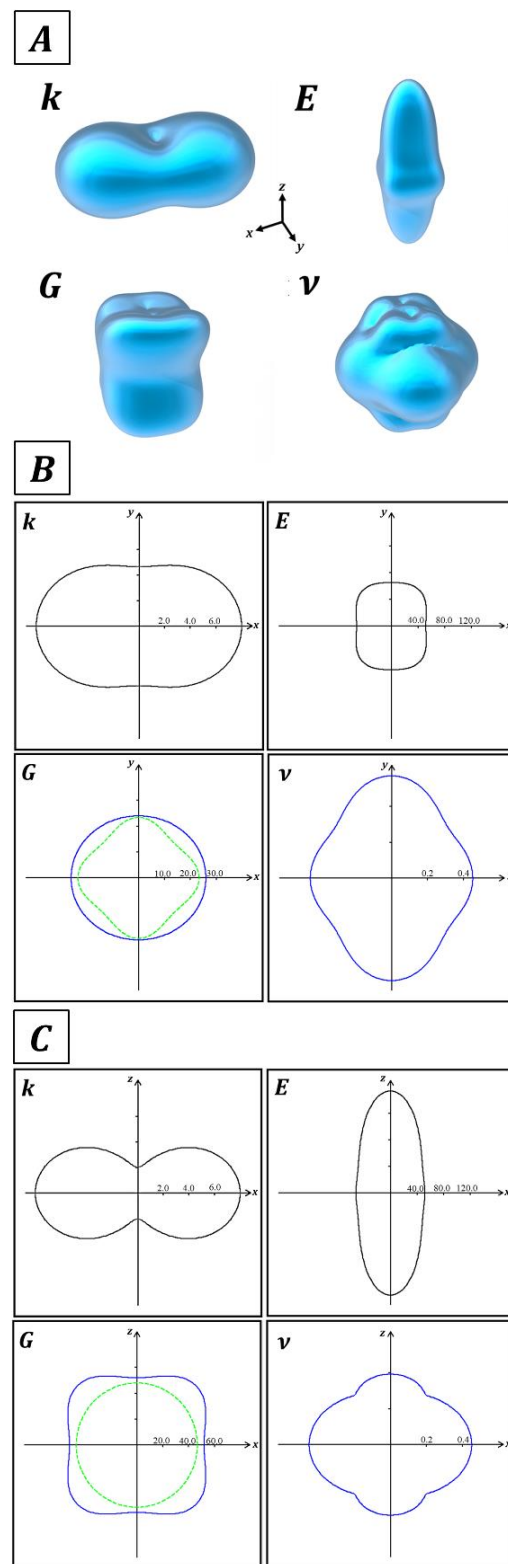


**Figure 5.** (A) Mechanical properties of ALPO-8 ( $Cmc2_1$ ) as a function of the orientation of the applied strain:  $k$ -compressibility,  $E$ -Young modulus,  $G$ -Maximum shear modulus, and  $\nu$ -Maximum Poisson's ratio; (B) bidimensional projections on the  $xy$  plane; (C) bidimensional projections on the  $xz$  plane. The projections of the surface of minimum shear modulus are also displayed using green color in panels (B,C).

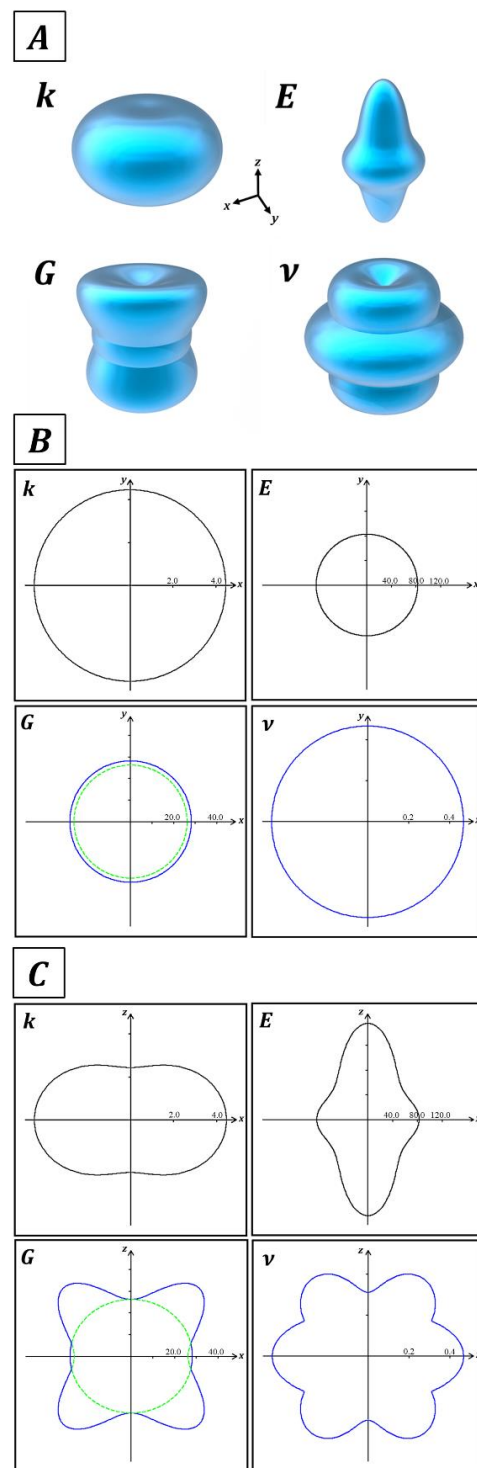


**Figure 6.** (A) Mechanical properties of ALPO-5 ( $P6cc$ ) as a function of the orientation of the applied strain:  $k$ -compressibility,  $E$ -Young modulus,  $G$ -Maximum shear modulus,  $\nu$ -Maximum Poisson's ratio; (B) bidimensional projections on the  $xy$  plane; (C) bidimensional projections on the  $xz$  plane. The projections of the surface of minimum shear modulus are also displayed using green color in panels (B,C).

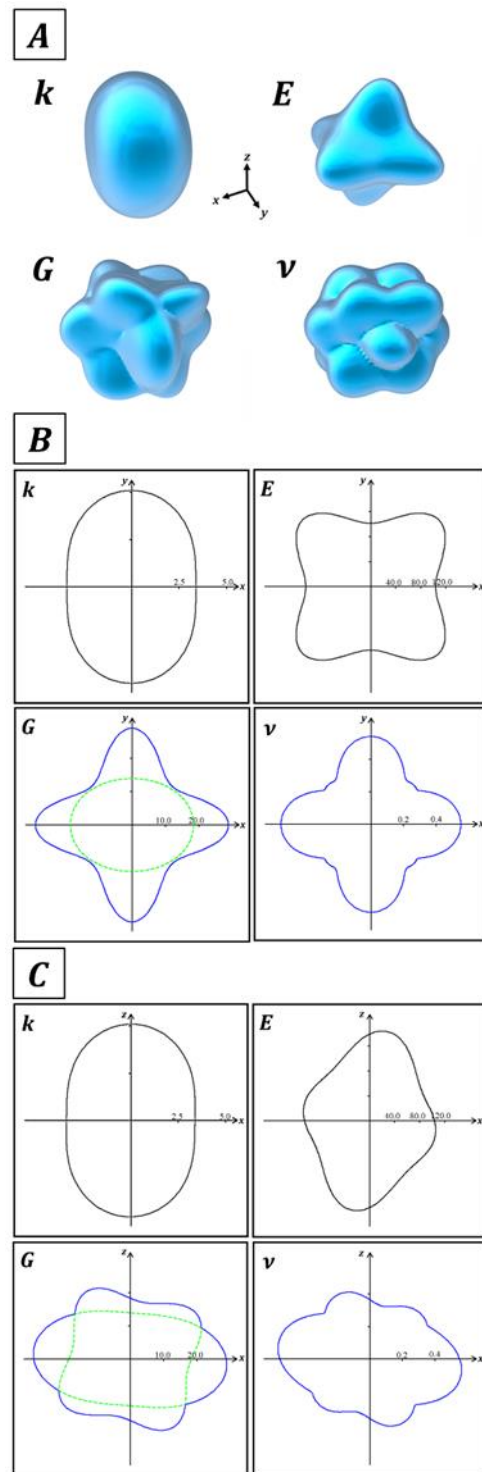


**Figure 7.** (A) Mechanical properties of ALPO-18 (C2/c) as a function of the orientation of the applied strain:  $k$ -compressibility,  $E$ -Young modulus,  $G$ -Maximum shear modulus, and  $\nu$ -Maximum Poisson's ratio; (B) bidimensional projections on the  $xy$  plane; (C) bidimensional projections on the  $xz$  plane. The projections of the surface of minimum shear modulus are also displayed using green color in panels (B,C).

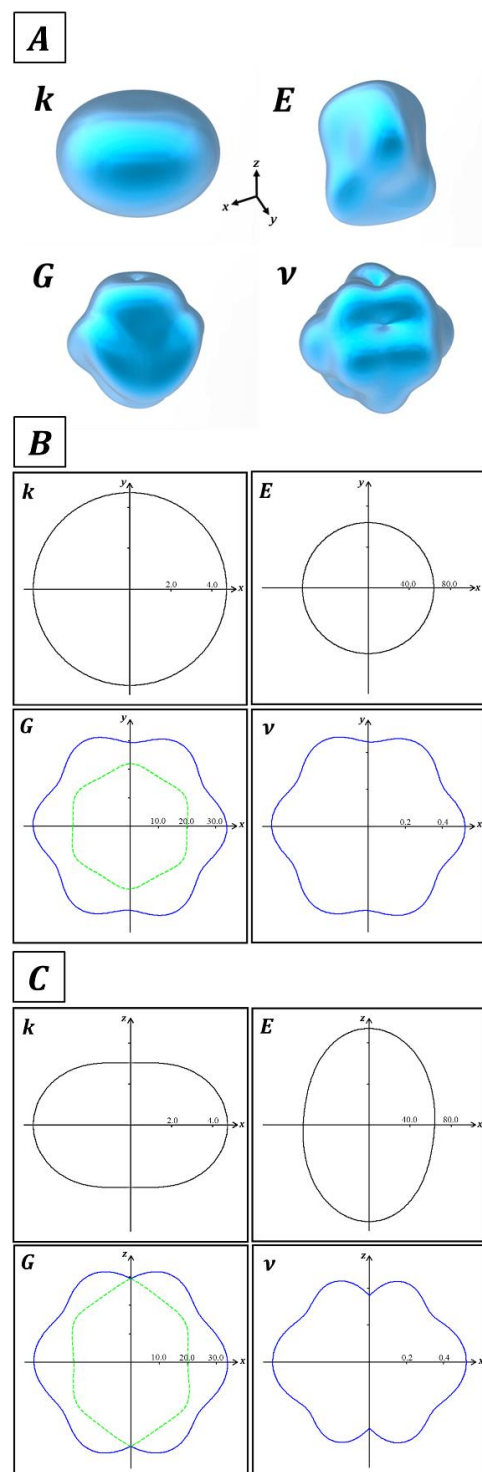


**Figure 8.** (A) Mechanical properties of ALPO-31 ( $R\bar{3}h$ ) as a function of the orientation of the applied strain:  $k$ -compressibility,  $E$ -Young modulus,  $G$ -Maximum shear modulus, and  $\nu$ -Maximum Poisson's ratio; (B) bidimensional projections on the  $xy$  plane; (C) bidimensional projections on the  $xz$  plane. The projections of the surface of minimum shear modulus are also displayed using green color in panels (B,C).

Figures 4–8 ( $k$  and  $E$ ) show that there are not preferred directions along which the compressibility and Young's modulus are negative, near to zero or particularly small. Therefore, ALPOs are very incompressible in all directions and there are not clear directions for material fracture when isotropic or uniaxial pressures are applied. Likewise, these

figures show a smooth directional dependence of the shear modulus ( $E$ ), without special directions associated with small values of this property (see the projections of the surfaces of minimum shear modulus). Therefore, there are not crystallographic planes along which shear failure can be predicted. The presence of shear slippages imposed serious limitations to the mechanical properties of some microporous materials including MOFs [72,75,80–82] and carbon nanotube composites [215,216]. No signs of auxeticity (negative Poisson's ratios [334]) were found for any of the materials investigated since the Poisson's ratios are always positive for all strain directions. This is in contrast with the elasticity of other microporous materials (for example for zeolites), for which negative or zero Poisson's ratios were frequently encountered [51–54,64–67].

### 3.5. Compressibility Functions

The crystal structures of VPI-5, ALPO-8, ALPO-5, ALPO-18, and ALPO-31 were fully optimized under different external isotropic pressures in the pressure range from  $-0.5$  to  $5.0$  GPa. The computed unit cell volumes and lattice parameters for VPI-5, ALPO-8, ALPO-5, ALPO-31 and ALPO-18 at different pressures are plotted in Figures 9–13, respectively. The calculated volumetric compressibilities,  $k_V = -1/V \cdot (\partial V / \partial P)_P$ , and the linear compressibilities,  $k_l = -1/l \cdot (\partial l / \partial P)_P$  ( $l = a, b, c$ ) along the three crystallographic directions between  $P = 0.0$  and  $P = 4.0$  GPa are also displayed in these figures. The values of the calculated unit cell volumes, lattice parameters and compressibilities are given in Tables S12–S21. The structure of ALPO-18 was also optimized under the effect of different uniaxial pressures (see Figure 14 and Tables S22 and S23). The calculated compressibilities of these materials at zero pressure are collected in Table 4. From this table, it follows that the volumetric compressibilities at zero pressure are very small, the most compressible material being VPI-5 ( $k_V = 16.46 \text{ TPa}^{-1}$ ) and the less compressible one being ALPO-31 ( $k_V = 11.06 \text{ TPa}^{-1}$ ).

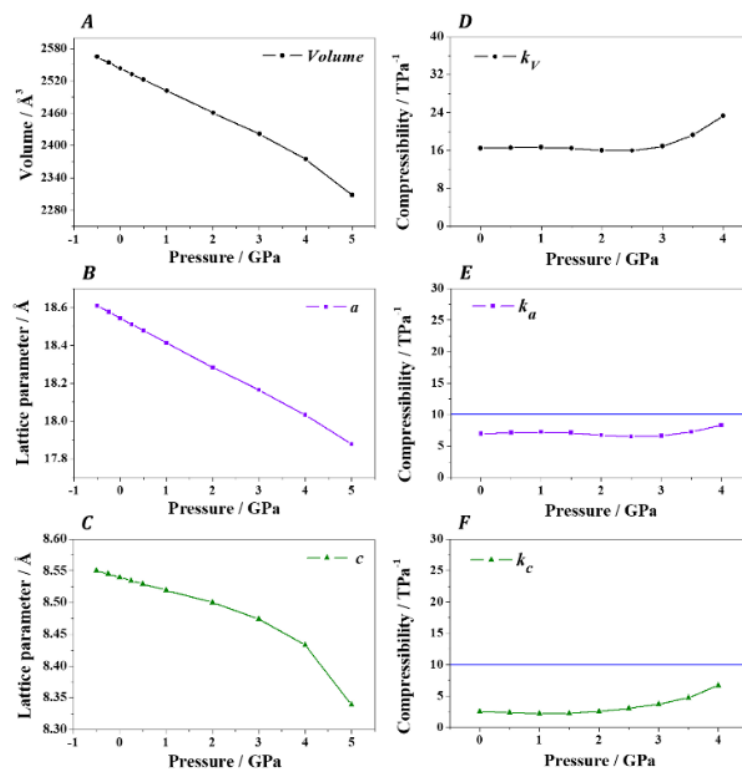


**Figure 9.** Computed unit cell volume (A) and lattice parameters  $a = b$  (B) and  $c$  (C) of VPI-5 ( $P6_3cm$ ) for different isotropic pressures. The volumetric compressibilities (D) and the linear compressibilities along  $a$  (E) and  $c$  (F) directions are shown in the panels of the right-hand side. The blue horizontal lines in panels (E,F) mark  $k_l = 10 \text{ TPa}^{-1}$ .

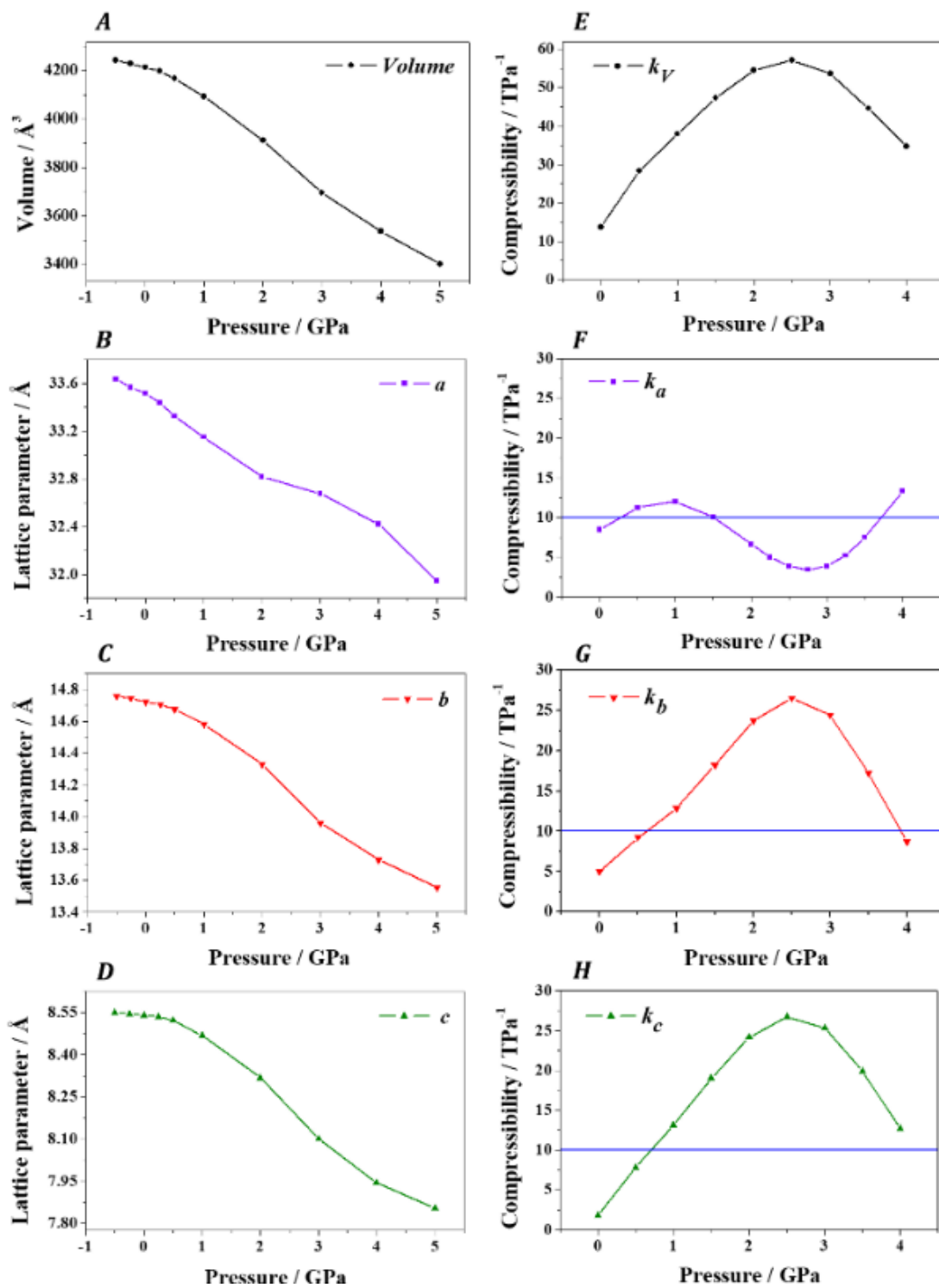


**Figure 10.** Computed unit cell volume (A) and lattice parameters (B–D) of ALPO-8 under different external isotropic pressures. The volumetric compressibilities (E) and the linear compressibilities along *a*, *b* and *c* (F–H) directions are shown in the panels of the right-hand side. The blue horizontal lines in panels (F–H) mark  $k_l = 10.0 \text{ TPa}^{-1}$ .

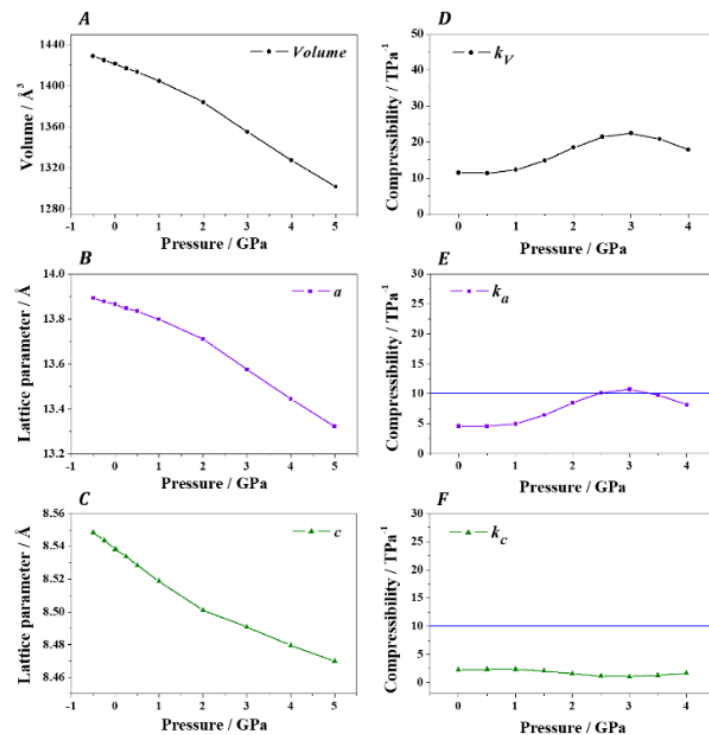


**Figure 11.** Computed unit cell volume (A) and lattice parameters  $a = b$  (B) and  $c$  (C) of ALPO-5 ( $P6cc$ ) for different isotropic pressures. The volumetric compressibilities (D) and the linear compressibilities along  $a$  (E) and  $c$  (F) directions are shown in the panels of the right-hand side. The blue horizontal lines in panels (E,F) mark  $k_l = 10.0 \text{ TPa}^{-1}$ .

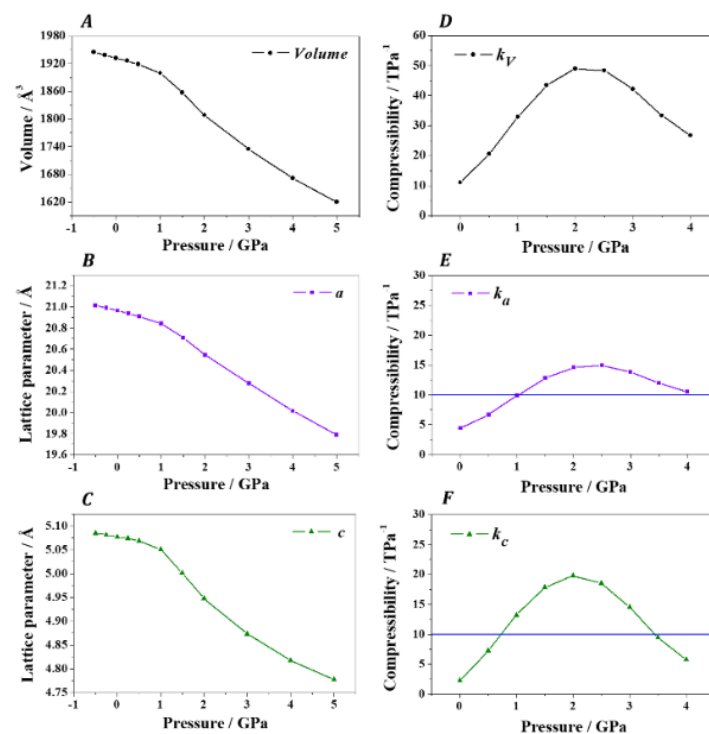


**Figure 12.** Computed unit cell volume (A) and lattice parameters  $a = b$  (B) and  $c$  (C) of ALPO-31 ( $R\bar{3}h$ ) for different isotropic pressures. The volumetric compressibilities (D) and the linear compressibilities along  $a$  (E) and  $c$  (F) directions are shown in the panels of the right-hand side. The blue horizontal lines in panels (E,F) mark  $k_l = 10.0 \text{ TPa}^{-1}$ .

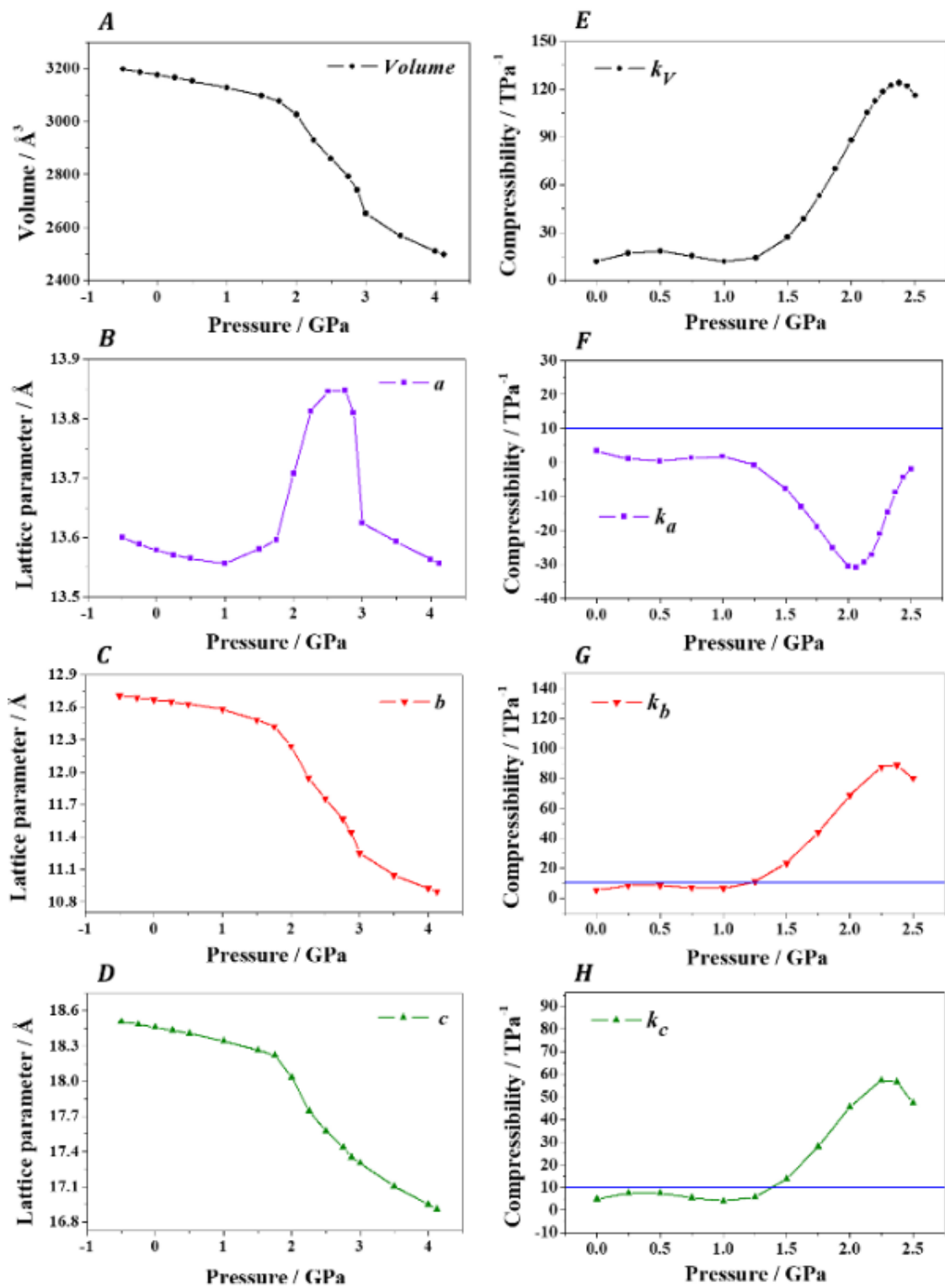


**Figure 13.** Computed unit cell volume (A) and lattice parameters (B–D) of ALPO-18 under different external isotropic pressures. The volumetric compressibilities (E) and the linear compressibilities along  $a$ ,  $b$  and  $c$  (F–H) directions are shown in the subgraphs of the right-hand side. The blue horizontal lines in panels (F–H) mark  $k_l = 10.0 \text{ TPa}^{-1}$ .

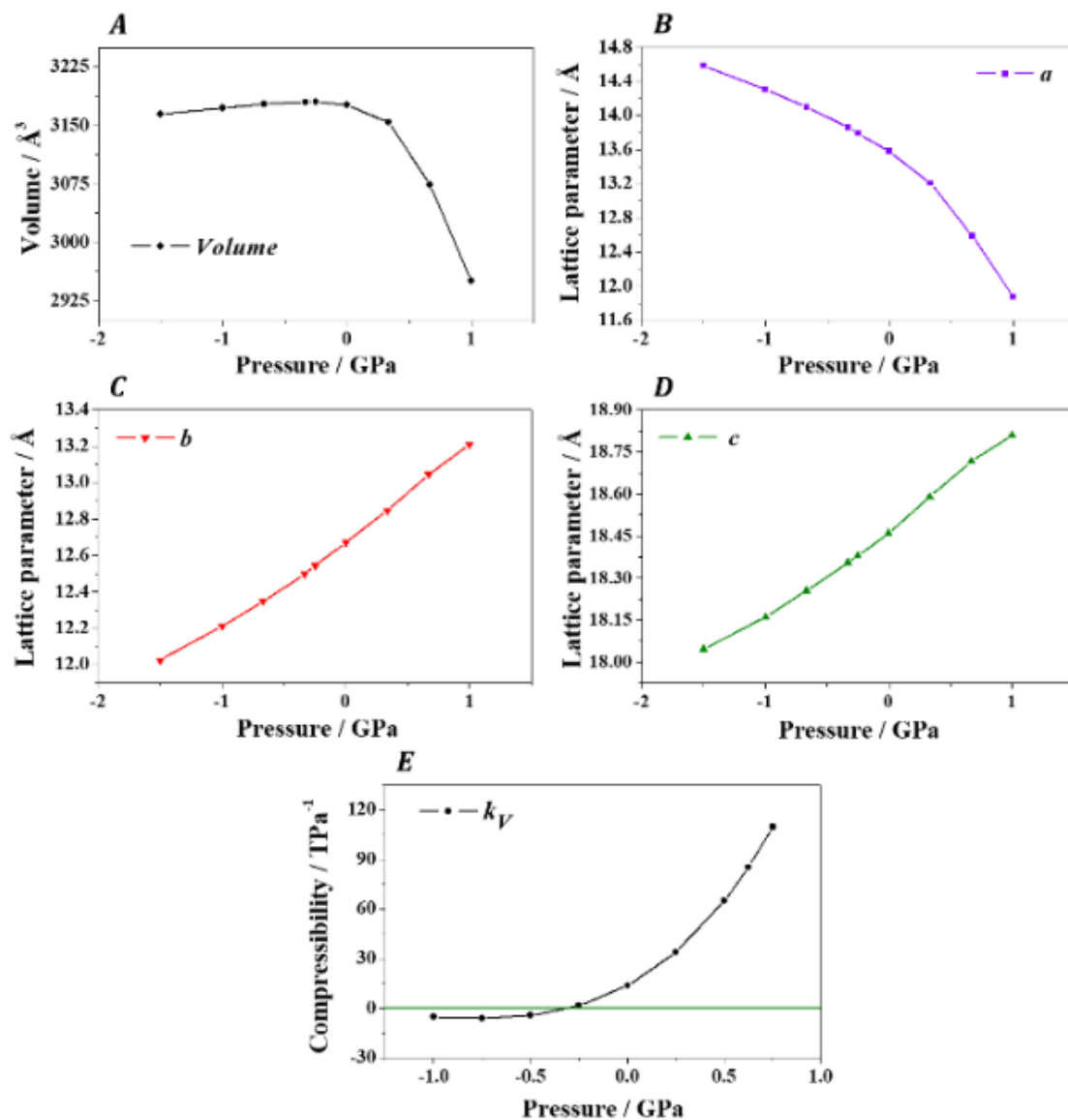


**Figure 14.** Computed unit cell volume (A) and lattice parameters (B–D) of ALPO-18 under different uniaxial pressures applied along the direction of minimum compressibility, [1 0 0]. The volumetric compressibilities are shown in panel (E) The green horizontal line in panel (E) mark  $k_V = 0.0 \text{ TPa}^{-1}$ .

**Table 4.** Calculated volumetric compressibilities and linear compressibilities at zero pressure for VPI-5, ALPO-8, ALPO-5, ALPO-18 and ALPO-31.

Material	$k_V(\text{TPa}^{-1})$	$k_a(\text{TPa}^{-1})$	$k_b(\text{TPa}^{-1})$	$k_c(\text{TPa}^{-1})$
VPI-5 ( $P6_3cm$ )	16.46	6.95	6.95	2.56
ALPO-8 ( $Cmc2_1$ )	13.77	6.93	5.04	1.81
ALPO-5 ( $P6cc$ )	11.45	4.61	4.61	2.25
ALPO-18 ( $C2/c$ )	13.54	3.40	5.17	4.97
ALPO-31 ( $R\bar{3}h$ )	11.09	4.43	4.43	2.23

The linear compressibilities along the different directions are frequently smaller than  $5 \text{ TPa}^{-1}$ . For ALPO-5 and ALPO-31, the three linear compressibilities are smaller than this threshold. The same occurs for two linear compressibilities of ALPO-18, although the compressibility along *b* direction is also very near to this limit ( $k_b = 5.17 \text{ TPa}^{-1}$ ). For VPI-5 and ALPO-8, only the compressibilities along *c* direction satisfy  $k_c < 5 \text{ TPa}^{-1}$ . However, the

value of  $k_c$  for ALPO-8 is the lowest linear compressibility found for all of the ALPO materials considered, ( $k_c = 1.81 \text{ TPa}^{-1}$ ). The criterium usually used for zero linear compressibility (ZLC) [102,103,132–135] is that the absolute value of the linear compressibility along a certain direction is smaller than  $1.0 \text{ TPa}^{-1}$ ,  $|k_l| \leq 1.0 \text{ TPa}^{-1}$  [133]. While this criterium is not met for ALPOs, the presence of three simultaneously small linear compressibilities is very infrequent. The term near zero tridimensional linear compressibility (NZTLC) is proposed for materials satisfying,  $1 \leq |k_l| \leq 5.0$  for  $l = a, b, c$ . ALPO-5, ALPO-31 and, in practical terms, ALPO-18 are NZTLC materials at zero pressure.

As shown in Figure 9, the compressibilities of VPI-5 along the three crystallographic directions are lower than  $10 \text{ TPa}^{-1}$  for the full range of pressure considered. The compressibility along the  $c$  direction is smaller than  $5 \text{ TPa}^{-1}$  from 0 to 4 GPa except for applied pressures near 4.0 GPa. Therefore, as shown in Figure S1, the isotropic compression of VPI-5, leads to very small changes of its structure. For ALPO-8 (Figure 10), although the linear compressibility along  $a$  direction remains small from 0 to 4 GPa and attains a minimum near  $P = 2.75 \text{ GPa}$  ( $k_a = 3.4 \text{ TPa}^{-1}$ ),  $k_b$  and  $k_c$  increase rapidly and reach maxima near  $P = 2.5 \text{ GPa}$ . Consequently, the volumetric compressibility increases from 0 to 2.5 GPa and then decreases up to 4 GPa. Since the compressibility along  $c$  direction is very small at zero pressure, and it is a strongly decreasing function as the pressure diminishes, the presence of negative values of  $k_a$  under tension (negative pressure) is highly probable. For ALPO-5 (Figure 11), as for VPI-5, the linear compressibilities remain small in the range from 0 to 4.0 GPa. However, for ALPO-31 (Figure 12), as for ALPO-8, the compressibilities increase largely as the pressure increases and the volumetric compressibility reach a maximum near  $P = 2.0 \text{ GPa}$ . The behavior of ALPO-18 under pressure is extremely anomalous and is studied in the next Subsection.

### 3.6. Negative Linear Compressibility (NLC) in ALPO-18

#### 3.6.1. Isotropic Negative Linear Compressibility (INLC)

The three lattice parameters of VPI-5, ALPO-8, ALPO-5, and ALPO-31 decrease invariably under isotropic compression. However, as can be observed in Figure 13B, the  $a$  lattice parameter of ALPO-18 increases sharply from  $P = 1.21$  to  $P = 2.70 \text{ GPa}$ . Therefore ALPO-18 exhibits the isotropic negative linear compressibility (INLC) phenomenon [129–131] in this pressure range. The minimum value of the compressibility along the  $a$  direction is encountered at  $P = 2.04 \text{ GPa}$ ,  $k_a = -30.9 \text{ TPa}^{-1}$ .

The INLC effect in ALPO-18 can be rationalized in terms of the empty channel structural mechanism [100,335]. The deformation of the crystal structure of ALPO-18 induced by the application of increasing isotropic pressures is illustrated in Figure 15. In this figure, the optimized crystal structures at five different pressures,  $P = 1.00, 1.75, 2.00, 2.25,$  and  $2.50 \text{ GPa}$ , are displayed.

As can be observed, the width and height of main 8-MR channels expanding along  $[0 0 1]$  increase and decrease substantially under increasing pressure. The widening of the channels along  $[1 0 0]$ , which coincides with the direction of minimum compressibility in ALPO-18 (see Figure 7), leads to an increase of the  $a$  lattice parameter and to the INLC effect in this material. The impact of the deformation of the channels expanding along  $[1 0 0]$  and  $[1 1 0]$  (Figure 2) in the dimensions of the crystal is much smaller, as shown in Figure S2. Therefore, the dominance of the deformation of the 8-MR channels expanding along  $[0 0 1]$  makes observable the NLC effect based in the empty structural mechanism in the multichannel ALPO-18 material.

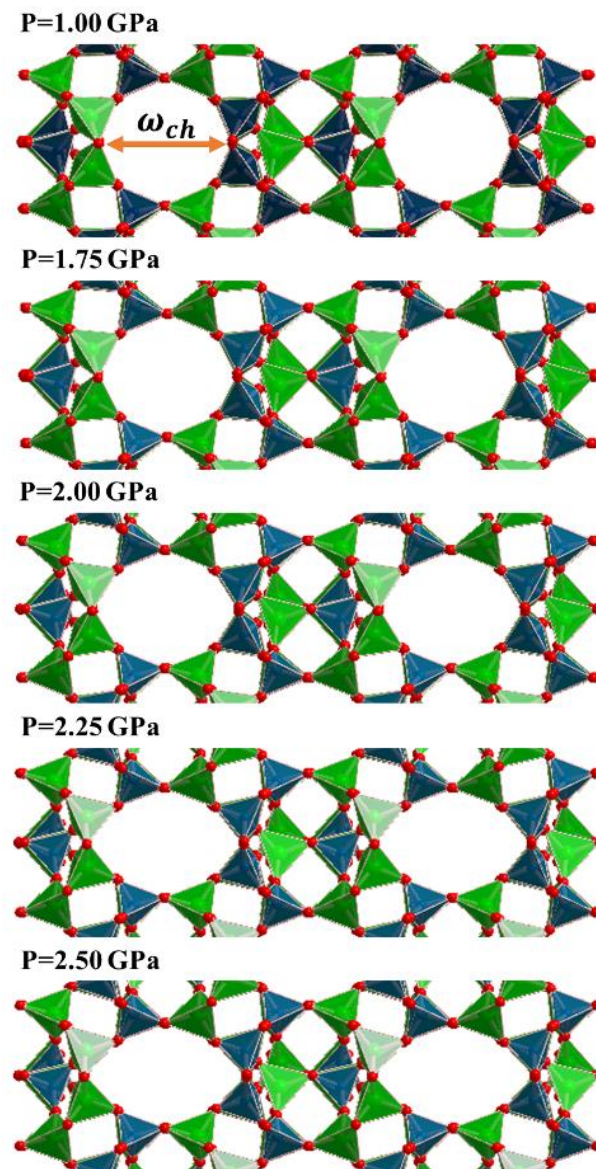


**Figure 15.** Two contiguous 8-MR channels expanding along [0 0 1] in the crystal structure of ALPO-18 under increasing isotropic pressures: 1.0, 1.75, 2.0, 2.25, and 2.50 GPa. The meaning of the width of a channel ( $\omega_{ch}$ ) as measured by the distance between two opposite oxygen atoms is illustrated in the structure at  $P = 1.0$  GPa. The values of  $\omega_{ch}$  are 6.453, 6.722, 7.049, 7.551, and 7.829 Å, respectively.

### 3.6.2. Anisotropic Negative Volumetric Compressibility (ANVC) Effect

In previous works, the INLC effect due to the empty channel structural mechanism was observed to be accompanied by the anisotropic volumetric NLC effect (ANLC) [100,336], i.e., the increase of the volume of a material when an external anisotropic pressure is applied to it. This effect was discovered in 2015 by Baughman and Fonseca [336] in porous materials and, independently, by Colmenero in 2019 for non-porous materials as the cyclic oxocarbon acids [307], oxalic acid [308] and uranyl squarate monohydrate [311]. The unit cell volumes, lattice parameters and compressibilities of ALPO-18 under the effect of increasing uniaxial pressures along the direction of minimum compressibility, [1 0 0], are shown in Figure 14 and provided in Tables S22 and S23 of the SM. As can be appreciated, the unit cell volume increases under tension from  $P = -1.0$  up to  $P = -0.20$  GPa. Therefore, ALPO-18 exhibits the ANVC effect in this pressure range. The minimum value of the compressibility is found at  $P = -0.76$  GPa,  $k_V = -6.0 \text{ TPa}^{-1}$ .

### 3.6.3. Effect of Dispersion Interactions in the NLC Effect of ALPO-18

In Section 3.1, the influence of dispersion interactions in the crystal structures of the considered ALPO materials was shown to be small. However, due to the relevance of the NLC phenomenon, the crystal structure of ALPO-18 was also completely optimized under the effect of different isotropic pressures using the PBE functional supplemented with Grimme's dispersion corrections [283]. The computed values of the  $a$  lattice parameter are compared with those obtained using the PBEsol functional in Figure 16. The results are quite similar, thus confirming the NLC effect in ALPO-18 and the good performance of the PBEsol functional for the description of anhydrous materials [191–284]. Using the dispersion corrected treatment, ALPO-18 displays an even larger isotropic NLC effect from  $P = 0.61$  GPa to  $P = 2.50$  GPa. The minimum value of the compressibility along the  $[1\ 0\ 0]$  direction is  $k_a = -38.7\ \text{TPa}^{-1}$  at  $P = 1.74$  GPa.

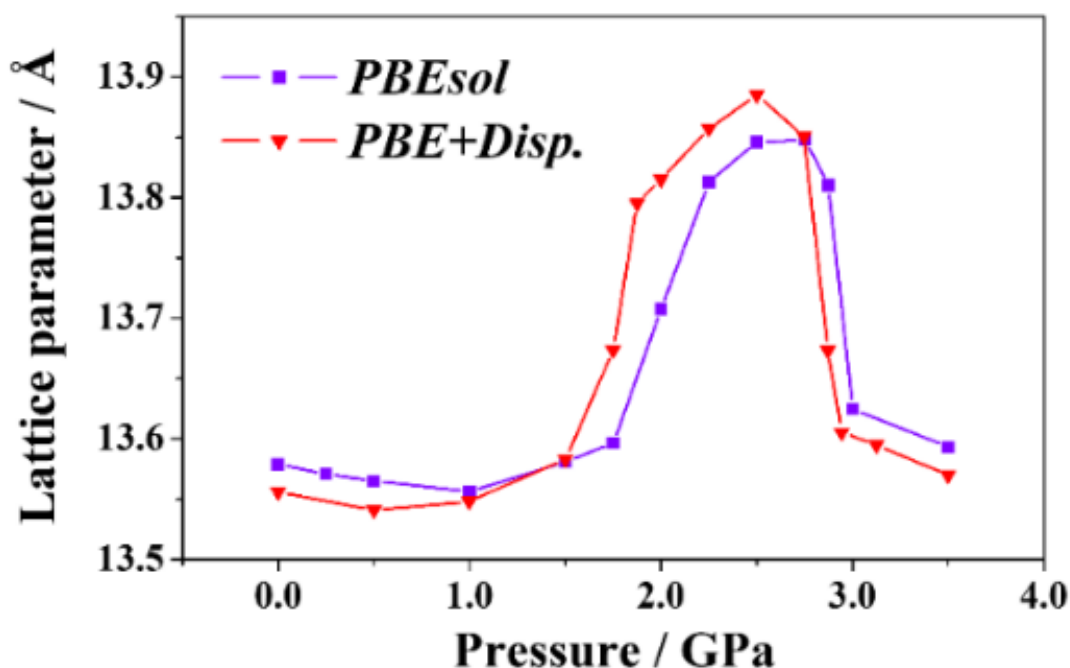


**Figure 16.** Comparison of the computed  $a$  lattice parameter of ALPO-18 under the effect of different external isotropic pressures using the PBEsol functional and the PBE functional supplemented with dispersion corrections.

### 3.7. Effect of Hydration in the Mechanical Properties of ALPO-18

In this Section, the effect of the presence of water molecules adsorbed in the structural channels of ALPO-18 on the mechanical properties of this material is studied. This is relevant from the point of view of applications since if one desires to take advantage of the mechanical properties of ALPOs, such as their large incompressibility and ductility, the influence of water adsorption should be considered. If the impact in the elastic properties is large, hydration should be avoided as much as possible. The calculated lattice parameters of ALPO-18W are given in Table 1. The computed unit cell volume differs from the experimental value [11] by only 0.5%. The computed stiffness tensor and mechanical properties of ALPO-18W are reported in Tables 5 and 6, respectively, and the dependence of its mechanical properties on the orientation of the applied strain is shown in Figure S3. The unit cell volumes, lattice parameters and compressibilities of ALPO-18W under different isotropic pressures are shown in Figure S4 and given in Tables S24 and S25.

**Table 5.** Computed elastic constants of VPI-5 ( $C1m1$ ), ALPO-5 ( $Pcc2$ ), and ALPO-18W ( $P1$ ). All of the values are given in GPa.

$ij$	$C_{ij}$		
	VPI-5 $C1m1$	ALPO-5 $Pcc2$	ALPO-18W $P1$
11	69.66	120.90	92.30
22	68.50	127.95	103.17
33	79.68	193.34	103.75
44	18.75	26.30	25.58
55	19.61	26.04	24.06
66	19.38	25.61	25.81
12	31.53	67.01	37.53
13	14.04	60.75	42.27
14	0.0	0.0	-2.52
15	-0.05	0.0	-5.10
16	0.0	0.0	7.90
23	12.60	62.53	41.38
24	0.0	0.0	6.67
25	-0.20	0.0	-0.47
26	0.0	0.0	3.03
34	0.0	0.0	0.50
35	0.42	0.0	-3.83
36	0.0	0.0	-1.19
45	0.0	0.0	1.85
46	0.20	0.0	0.58
56	0.0	0.0	1.37

**Table 6.** Computed mechanical properties of VPI-5 ( $C1m1$ ), ALPO-5 ( $Pcc2$ ) and ALPO-18W ( $P1$ ). The values of the bulk, shear and Young's moduli ( $B$ ,  $G$  and  $E$ ) are given in in GPa. The single-crystal bulk moduli ( $B^{sc}$ ) are also given in the last row of the table for comparison.

Property	VPI-5 $C1m1$	ALPO-5 $Pcc2$	ALPO-18W $P1$
$B$	$37.06 \pm 0.81$	$88.62 \pm 0.37$	$58.82 \pm 0.94$
$G$	20.98	29.58	25.81
$E$	54.24	79.87	67.56
$\nu$	0.26	0.35	0.31
$D$	1.77	3.00	2.28
$D^I$	0.24	0.51	0.18
$H$	3.10	1.02	2.11
$A^U$	0.29	0.50	0.24
$B^{sc}$	$33.85 \pm 1.90$	$87.71 \pm 0.27$	$58.80 \pm 1.84$

Since ALPO-18 is triclinic, all of the elements of the matrix representation of its elastic tensor are non-vanishing and non-equivalent. As with ALPO-18, ALPO-18W is characterized by large bulk, Young's, and shear moduli. However, due to the adsorption of water molecules, the bulk and shear moduli of ALPO-18W become much smaller and larger, respectively, than those of ALPO-18. Consequently, although ALPO-18W is also ductile, the ductility index is smaller. Since the intrinsic ductility index ( $D^I$ ) is strongly correlated with Pugh's ratio [190], its value is reduced from 1.02 to 0.18. Therefore, hydration makes this material more compressible and less ductile. The universal anisotropy index is very small,  $A^U = 0.24$ , as with the other ALPO materials. As expected from the small elastic anisotropy index, the dependence of the mechanical properties on the direction of the applied strain is smooth. No preferred directions for fracture or shear failures nor negative Poisson's ratios are observed.

In a recent work [100], a strong reduction of the NLC effect in titanium oxalate dihydrate was also found as a result of water molecule adsorption, although the NLC effect in this microporous metal organic framework does not disappear completely. In contrast, for some microporous zeolites and MOFs [56,57,98,99], water intrusion leads to a strong increase of the unit-cell volume and NLC effects. The strong influence of the presence of guest molecules in the structural channels of porous materials in their mechanical properties has been found by several research groups in previous works [87,88,337]. In fact, Terracina et al. [88], showed that the main source of structural instability in the MOF HKUST-1 during compaction was the presence water molecules adsorbed by the powdered samples and a new tableting method preserving the crystal structure and porosity of the pristine powders was reported. The influence of guest molecule adsorption in the elastic properties of microporous materials is highly dependent on the material under study and the type of interaction between the molecules with the walls of the channels and between the molecules themselves. The presence of water in contact with the material may increase the internal tensions, lead to phase transformations or even be the origin of crack propagation and fracture [238]. The important NLC effect induced by water or guest molecule intrusion should be distinguished from the conventional NLC phenomenon, encountered for ALPO-18 in this paper, due to the need of specifying the origin of pressure and the requirement of the description of the interaction of a variable number of guess molecules with the material for his theoretical study. It is a common belief that the absorption of water molecules in the channels of a microporous material should reduce its compressibility due to the stiffening of the structure due to increased density [338]. However, the opposite is true in ALPO-18. The counterintuitive softening upon adsorption of guest molecules in microporous materials was first observed by Mouhat et al. [339] and Canepa et al. [340]. It is difficult to find an explanation for the softening in ALPO-18 based on the changes in the chemical bonding due to the drastic geometric rearrangement occurring upon water absorption. This requires a further study which is out of the scope of the present work.

The great influence of water adsorption in the structure of ALPO-18, underlines the need of using non-hydrous pressure transmitting media (PTM) to measure their compressibilities or experimental methods which are not based in the use of DAC in order to study its full tensorial elasticity. The compressibility of hydrated ALPO-5 [165–167] material was measured experimentally using DACs and different pressure transmitting media. The measured compressibilities were highly dependent of the PTM used. Furthermore, the compressibilities measured using the same PTM vary significantly from one study to another. For example, the volumetric compressibilities of ALPO-5W using a 16:3:1 methanol-ethanol-water (MEW) mixture as PTM measured by Kim et al. [166] and Lotti et al. [167] were 19.8 and 45.0 TPa<sup>-1</sup> (corresponding to measured bulk moduli of 50.5(7) and 22.2(9) GPa), respectively. For VPI-5W, Alabarse et al. [168], using silicone oil as PTM, obtained of volumetric compressibility of 41.2 Tpa<sup>-1</sup> ( $B = 24.3(5)$  Gpa). The present results for anhydrous VPI-5 and ALPO-5 and the experimental results for VPI-5W and ALPO-5W show that, as for ALPO-18, the influence of the presence of water in the channels of these materials in the elastic properties are substantial. Again, the use of complementary experimental methods not based in the use of DAC with a PTM for the study of the full tensorial elasticity of these materials is suggested.

### 3.8. Effect of Aging in the Elastic Properties of VPI-5

De Oñate Martínez et al. [5], noted that the space symmetry of VPI-5 depends on the method of preparation of this material and that aging also leads to space symmetry variations. Clearly, the origin of this effect is the small differences in the relative thermodynamic stabilities of the different crystal structures of ALPO materials [341,342]. Therefore, to assess the influence of aging, the monoclinic  $C1m1$  crystal structure reported by De Oñate Martínez et al. [5] obtained from an aged sample of anhydrous VPI-5 was employed in order to compute its mechanical properties. The computed lattice parameters are given in Table S26 of the SM and the calculated stiffness tensor and mechanical properties are

given in Tables 5 and 6, respectively. The dependence of its mechanical properties on the direction of the applied strain is shown in Figure S5. The bulk modulus for the monoclinic structure of VPI-5 diminishes significantly with respect to that for hexagonal VPI-5 (from 60.5 to 37.1 GPa) and, consequently, the ductility index is largely reduced (from 2.66 to 1.77). The elastic anisotropy in monoclinic VPI-5 ( $A^U = 0.24$ ) is smaller than in hexagonal VPI-5 ( $A^U = 0.66$ ). Although the directional dependence of the elastic properties for the monoclinic structure are significantly modified, the axial symmetry around  $z$  axis is conserved (Figure S5B) and no preferred directions for fracture and shear failure are observed. Therefore, aging in VPI-5, as hydration in ALPO-18, reduces its incompressibility and ductility. The computed unit-cell volume, lattice parameters and compressibilities of monoclinic VPI-5 as a function of the external isotropic pressure are shown in Figure S6 and given in Tables S27 and S28 of the SM. While the linear compressibilities of hexagonal VPI-5 remains small as pressure increases, the same is not true for the monoclinic structure.

### 3.9. Effect of Pressure Polymorphism

#### 3.9.1. VPI-5

Since in this paper we are interested in studying the behavior of ALPO materials under the effect of pressure, the relative thermodynamic stability of the  $P6_3cm4$  and  $C1m1$  [5] structures of VPI-5 under pressure was investigated. Both crystal structures were fully optimized under the effect of different external isotropic pressures and the corresponding enthalpies were determined. As shown in Figure S7 of the SM, the X-ray diffraction patterns of both structures at zero pressure are remarkably similar. The positions of the main reflections in the X-ray diffraction patterns of both structures are reported in Tables S2 and S29, respectively. The computed unit cell volumes and enthalpies are compared in Figure 17. In this figure the volumes and enthalpies of the  $P6_3cm$  structure have been doubled since the unit-cell of the  $C1m1$  structure is twice as large as the hexagonal unit cell. As can be seen, while the enthalpies of both structures are very close at zero pressure, the monoclinic structure is increasingly more stable as pressure increases. The difference of the enthalpies of both polymorphs, 0.3 kJ per formula unit at zero pressure, becomes 28.6 kJ at  $P = 5.0$  GPa. Therefore, the VPI-5 monoclinic polymorph appears to be significantly more stable than the hexagonal one at high pressure conditions. The transition pressure between these structures is conditioned by thermodynamic and kinetic considerations [343]. In the initial studies concerning the structures of ALPO materials [344], great effort was devoted to the identification of the symmetry of their structures. Present results show that the difficulty in the identification, is further complicated by pressure polymorphism. At the same time, the results point to a form of obtaining monoclinic VPI-5 by submitting hexagonal VPI-5 to high isotropic pressures. As was shown in Section 3.8, the hexagonal-monoclinic polymorphic transformation reduces the incompressibility and ductility of VPI-5 substantially. It should be noted that an additional monoclinic  $C1m1$  structure for VPI-5 under pressure was also recently obtained by Fabbiani et al. [345] with a volume four times that of the hexagonal structure and two times that of the monoclinic structure reported by De Oñate Martínez et al. [5]. As shown in Table S30, the X-ray diffraction pattern derived from the structure of De Oñate Martínez et al. [5] is nearly the same as that derived from this structure, the difference in the positions of the main reflections being lower than  $0.1^\circ$ . This structure was obtained under the effect of isotropic pressure, in agreement with the present results favoring the monoclinic structures under pressure.

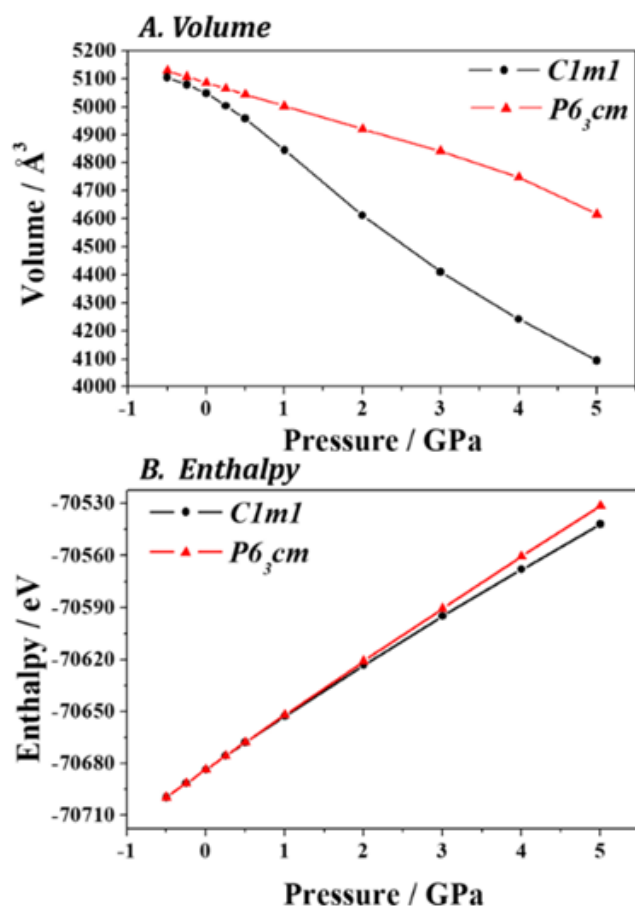


**Figure 17.** Comparison of the unit-cell volumes (A) and enthalpies (B) of the  $P6_3cm_2$  and  $C1m1_2$  crystal structures of VPI-5 under different isotropic pressures.

### 3.9.2. ALPO-5

For ALPO-5, the relative thermodynamic stability of the  $Pcc_2$  [8] and  $P6cc$  [9] structures under pressure was investigated. Figure S8 of the SM shows the great similarity of X-ray diffraction patterns of both structures at zero pressure. The positions of the main reflections in the X-ray diffraction patterns of both structures are given in Tables S4 and S31, respectively. The unit cell volumes and enthalpies associated with both structures under the effect different external pressure are compared in Figure 18. The volumes and enthalpies of the  $P6cc$  structure were doubled in Figure 18 (the orthorhombic unit cell is twice as large as the hexagonal one). Both structures are nearly degenerate at zero pressure. However, the orthorhombic structure is increasingly more stable as the pressure increases. The enthalpy difference becomes 12.1 kJ per formula unit ( $AlPO_4$ ) at  $P = 5.0$  GPa. The hexagonal-orthorhombic polymorphism in the anhydrous and hydrated forms of ALPO-5 is a long-standing problem [8,9,346–356]. The presence of one or another polymorph is not only dependent on the temperature but also on the method used for the synthesis of this compound [356]. The results obtained here show that the orthorhombic structure is the high-pressure polymorph. The orthorhombic structure should be obtainable submitting the hexagonal polymorph to high pressure. Similarly, the synthesis of ALPO-5 at sufficiently high pressure should favor the production of the orthorhombic form, independently of the synthetic method employed.

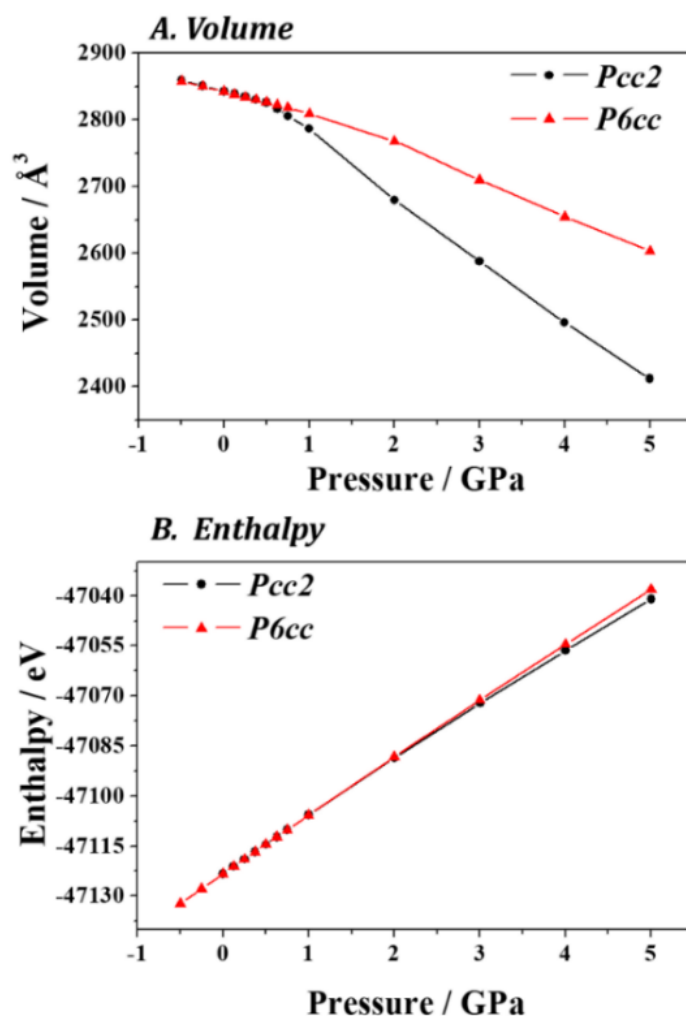


**Figure 18.** Comparison of the unit-cell volumes (A) and enthalpies (B) of the *Pcc2* and *P6cc* crystal structures of ALPO-5 under different isotropic pressures.

The computed lattice parameters of the *Pcc2* structure [8] at zero pressure are given in Table S26 of the SM. The calculated stiffness tensor and mechanical properties are reported in Tables 5 and 6, respectively. The dependence of its mechanical properties on the direction of the applied strain is shown in Figure S9. In contrast with the result obtained for VPI-5 in previous Section, the variation of the elastic properties for the orthorhombic structure with respect to those of the hexagonal one is exceedingly small. For example, the bulk modulus for the hexagonal polymorph,  $B = 88.2$  GPa, becomes 88.6 GPa. The intrinsic ductility index,  $D^I = 0.51$ , is unchanged. The directional dependence of the elastic properties for the two polymorphs is quite similar. The axial symmetry around the  $z$  axis for the hexagonal structure is slightly distorted in the orthorhombic polymorph (Figure S9B). Consequently, the impact of pressure polymorphism in the mechanical properties of ALPO-5 at zero pressure is very small. The computed unit-cell volumes, lattice parameters, and compressibilities of orthorhombic ALPO-5 as a function of the applied isotropic pressure are displayed in Figure S10 and given in Tables S32 and S33 of the SM. Although the influence of the pressure polymorphism in the elastic properties of ALPO-5 is small, the linear compressibilities along  $a$  and  $c$  directions and the volumetric compressibility of the orthorhombic polymorph are strongly affected by the increase of pressure. Only the linear compressibility  $b$  direction remains nearly constant under pressure with a value close to  $k_b = 5 \text{ TPa}^{-1}$ .

### 3.10. Comparison with Experimental Data

There are very few data to compare the results of the present paper with experimental data [165–172]. They are mostly for hydrated ALPO materials and limited to compressibility values measured using the DAC technique using a given PTM. There appears to exist a large difference between the experimental values of the compressibility measured using this technique and the theoretical results for empty porous structures. The same is true for the experimental results obtained with and without a PTM [150], using two different PTMs or from two different studies using the same PTM [166–168]. For different PTMs, involving different molecules, the collisions of molecules with the surfaces of the material considered produce different effects. In many cases, pressure induced transitions and pressure induced amorphizations (PIA) appear at very different pressures for different PTMs [166–168]. For instance, for ALPO-5W [166], a PIA was observed at 15.9 GPa using liquid nitrogen as PTM and at 8.5 GPa using silicone oil (non-pore-penetrating PTM). For dense crystal structures accurate values of the compressibilities are generally obtained [314]. The measurements performed for some ALPO materials indicate large compressibilities. For example, for a crystalline sample of dehydrated VPI-5, Alabarse et al. [169] using a DAC with silicone oil observed a pressure induced phase transition to ALPO-8 beginning at 0.8 GPa, which do not appear from the theoretical calculations, obtained a compressibility of  $k = 80.6 \text{ TPa}^{-1}$  (bulk modulus  $B = 12.4(2) \text{ GPa}$ ) for VPI-5 from a fit to a second order Birch–Murnaghan (2-BM) equation of state (EOS) from pressure–volume data below 1.6 GPa and the same value for ALPO-8 from data below 3.4 GPa. For dehydrated ALPO-17, Alabarse et al. [171] using a DAC with silicone oil observed a pressure induced amorphization beginning at 1 GPa and obtained a compressibility of  $k = 32 \text{ TPa}^{-1}$  (bulk modulus  $B = 31.2(5) \text{ GPa}$ ) from a fit to a 3-BM EOS from pressure–volume data below 3.1 GPa. The results obtained in this work showed that the compressibilities obtained from fits to a BM EOS are highly dependent on the pressure range used in the fits and that many pressure-volume data points should be used to obtain reliable compressibilities. Furthermore, the emergence of pressure induced amorphizations should influence substantially in the measured compressibilities due to the reduction of the volume involved in the pore collapse. NLC phenomena were also observed for ALPO materials in previous works. However, the NLC effects observed were much less significant than that found for ALPO-18 in this work. For ALPO-17, Alabarse et al. [171], found a small increase of the  $a$  lattice parameter near the PIA associated to the pore collapse. Likewise, for ALPO-5W, Kim et al. [166] found that  $a$  lattice expands at small pressures before it starts to contract using a MEW mixture as a PTM (probably due to molecule pore intrusion).

The results obtained using theoretical techniques are unique. The underlying reason for the different theoretical and experimental results based in DAC must be the different origin of pressure in these experimental techniques (collisional mechanism) and in the theoretical calculations. In the theoretical calculations, the pressure is defined in terms of the stress tensor and the elastic properties are determined from the stress tensor resulting from an applied strain and the action of molecules over the material is not invoked. The data presented in this paper are rigorous quantum mechanical results and were fully revised and carried out twice to check their reproducibility. Furthermore, the compressibilities obtained from the computed elastic tensors and fits of computed pressure-volume data are in excellent agreement. Thus, it is concluded that the data obtained from the theoretical calculations and experimental measurements using DAC correspond to different physical quantities for highly porous materials. To obtain a better agreement between theoretical and experimental results, either experimental measurements not based in DAC or quantum molecular dynamic calculations with specific solvents simulating the effect of the different PTMs should be carried out. The effect of temperature should also be investigated since the present theoretical results correspond to zero temperature.

#### 4. Conclusions

In this work, the crystal structures, mechanical properties, and compressibility functions of five important anhydrous microporous aluminophosphate materials have been determined using first principles methods based on density functional theory. The calculated crystal structures and associated X-ray diffraction patterns are in good agreement with their experimental counterparts. The elastic tensors of all of these materials have been reported and the mechanical stability of their structures has been confirmed. A detailed mechanical characterization is performed, and a rich set of mechanical properties was derived. This set includes the bulk, shear and Young's moduli, as well as ductility, hardness, and elastic anisotropy indices. The elastic behavior of the five materials shares many common mechanical properties such as high incompressibility, ductility, and low elastic anisotropy. Their intrinsic ductility indices are in the same range as that for common metals. The analysis of the dependence of the mechanical properties of ALPOs in the orientation of the applied strain, show that they are resistant with respect to the application of external isotropic and uniaxial pressures and shear stresses. A smooth directional dependence is found in all of the cases and no special directions for material fracture or shear instability are encountered. The only previous study from which some clue about the incompressibility of ALPO materials was found is the work by Polisi et al. [210] where the dehydration mechanism of hydrated ALPO-5 was studied. The small volume change of this material under the effect of temperature led these authors to state that ALPO-5 was one of the most rigid zeolite frameworks. While this finding concerns only the thermal behavior of hydrated ALPO-5, the present results show that high incompressibility is a general property of anhydrous ALPO materials under the effect of pressure.

The crystal structures of all of the materials were completely optimized under the effect of different isotropic pressures and the linear and volumetric compressibilities were determined. At zero pressure, the ALPO materials have small linear compressibilities along the three crystallographic directions. The tridimensional incompressibility of ALPO-5, ALPO-18 and ALPO-31 is notable since the compressibilities along the three principal directions are lower or close to  $5 \text{ TPa}^{-1}$ . The incompressibility ALPO-8 and ALPO-31 materials is lost at high pressures. ALPO-18 displays an extremely anomalous mechanical behavior at relatively low external pressures. It exhibits a large negative linear compressibility effect between  $P = 1.21$  and  $P = 2.70$  GPa. The minimum value of the compressibility along  $[1 0 0]$  direction,  $k_a = -30.9 \text{ TPa}^{-1}$ , is encountered at  $P = 2.04$  GPa. The NLC phenomenon in this material can be rationalized using the empty channel structural mechanism. The width and height of main 8-MR channels expanding along  $[0 0 1]$  increase and decrease substantially under increasing pressure. The widening of the channels along  $[1 0 0]$ , coinciding with the direction of minimum compressibility in ALPO-18, leads to the increase of the  $a$  lattice parameter and to the NLC effect in this material. Furthermore, ALPO-18 exhibits the anisotropic negative volumetric compressibility effect for uniaxial pressures applied along the  $[1 0 0]$  direction.

The effect of water molecule adsorption in the channels of ALPO-18 in its elastic properties is assessed by studying the mechanical behavior of the hydrated ALPO-18 material (ALPO-18W). ALPO-18W is much more compressible and less ductile than ALPO-18 and does not present the NLC effect found in ALPO-18. The effect of aging and pressure polymorphism in the mechanical properties of VPI-5 and ALPO-5 is also studied. As hydration, aging and pressure polymorphism leads to significant variations in the elastic properties of VPI-5 and reduces its incompressibility and ductility. For ALPO-5, pressure polymorphism has only a small impact in its elasticity at zero pressure but a large influence at high pressure.

**Supplementary Materials:** The following supporting information can be downloaded at: <https://www.mdpi.com/article/10.3390/solids3030032/s1>, The Supplementary Information associated with this article contains: (a) material data and calculation parameters; (b) interatomic distances and angles; (c) positions of the main reflections in the X-ray diffraction patterns; (d) unit-cell volumes, lattice parameters and compressibilities under isotropic and anisotropic pressures.

**Author Contributions:** Conceptualization: F.C.; investigation: F.C., Á.L. and V.T.; writing—original draft: F.C.; writing—review and editing: F.C., Á.L. and V.T. All authors have read and agreed to the published version of the manuscript.

**Funding:** This work was financially supported by the Ministry of Science, Innovation and Universities (project PGC2018-094814-B-C21). One of the authors (VT) was supported by the Ministry of Science, Innovation and Universities within the Project FIS2016-77726-C3-1-P.

**Data Availability Statement:** Not available.

**Acknowledgments:** Supercomputer time by the CTI-CSIC center is gratefully acknowledged. We want to thank A.M. Fernández for reading the manuscript and many helpful comments.

**Conflicts of Interest:** The authors declare that they have no known competing financial interest or personal relationship that could have appeared to influence the work reported in this paper.

## References

1. Wright, P.A. *Microporous Framework Solids*; RSC Publishing: Cambridge, UK, 2008.
2. Davis, M.E.; Garces, J.; Saldarriaga, C.; Crowder, C. A molecular sieve with eighteen-membered rings. *Nature* **1988**, *331*, 698–699. [[CrossRef](#)]
3. McCusker, L.B.; Baerlocher, C.; Jahn, E.; Bülow, M. The Triple Helix inside the Large-Pore Aluminophosphate Molecular Sieve VPI-5. *Zeolites* **1991**, *11*, 308–313. [[CrossRef](#)]
4. Poojary, D.M.; Perez, D.M.; Clearfield, J.O. Crystal Structures of Dehydrated VPI-5 and H1 Aluminum Phosphates from X-ray Powder Data. *J. Phys. Chem. C* **1992**, *96*, 7709–7714. [[CrossRef](#)]
5. De Oñate Martínez, J.; McCusker, L.B.; Baerlocher, C. Characterization and Structural Analysis of Differently Pre-pared Samples of Dehydrated VPI-5. *Microporous Mesoporous Mater.* **2000**, *34*, 99–113. [[CrossRef](#)]
6. Dessau, R.M.; Schlenker, J.L.; Higgins, J.B. Structure Determination and Rietveld Refinement of Aluminophosphate Molecular Sieve AlPO<sub>4</sub>-8. *Zeolites* **1990**, *10*, 522–524. [[CrossRef](#)]
7. Richardson, J.W.; Vogt, E.T.C. Structure determination and rietveld refinement of aluminophosphate molecular sieve AlPO<sub>4</sub>-8. *Zeolites* **1992**, *12*, 13–19. [[CrossRef](#)]
8. Mora, A.J.; Fitch, A.N.; Cole, M.; Goyal, R.; Jones, R.H.; Jobic, H.C.; Carr, S.W. The Structure of the Calcined Aluminophosphate AlPO<sub>4</sub>-5 Determined by High Resolution X-Ray and Neutron Powder Diffraction. *J. Mater. Chem.* **1996**, *6*, 1831–1835. [[CrossRef](#)]
9. Klap, G.J.; van Koningsveld, H.; Graafsma, H.; Schreurs, A.M.M. Absolute Configuration and Domain Structure of AlPO<sub>4</sub>-5 Studied by Single Crystal X-ray Diffraction. *Microporous Mesoporous Mater.* **2000**, *38*, 403–412. [[CrossRef](#)]
10. Simmen, A.; McCusker, L.B.; Baerlocher, C.W.; Meier, W. The Structure Determination and Rietveld Refinement of the Aluminophosphate AlPO<sub>4</sub>-18. *Zeolites* **1991**, *11*, 654–661. [[CrossRef](#)]
11. Poulet, G.; Tuelm, A.; Sautet, P.A. Combined Experimental and Theoretical Evaluation of the Structure of Hydrated Microporous Aluminophosphate AlPO<sub>4</sub>-18. *J. Phys. Chem. B* **2005**, *109*, 22939–22946. [[CrossRef](#)]
12. Bennett, J.M.; Kirchner, R.M. The Structure of Calcined AlPO<sub>4</sub>-31: A New Framework Topology Containing One-Dimensional 12-Ring Pores. *Zeolites* **1992**, *12*, 338–342. [[CrossRef](#)]
13. Endregard, M.; Nicholson, D.G.; Stocker, M.; Beagle, B. Cobalticinium Ions Adsorbed on Large-pore Aluminophosphate VPI-5 Studied by X-Ray Absorption, <sup>13</sup>C Solid-state NMR and FTIR Spectroscopy. *J. Mater. Chem.* **1995**, *5*, 485–491. [[CrossRef](#)]
14. Endregard, M.; Nicholson, D.G.; Stocker, M.; Lamb, G.J. Adsorption and Thermal Decomposition of Cobalticinium Ions on AlPO<sub>4</sub>-5 Studied by X-Ray Absorption Spectroscopy, <sup>13</sup>C Solid-State NMR and FTIR. *J. Mater. Chem.* **1995**, *5*, 785–791. [[CrossRef](#)]
15. Parton, R.F.; Thibault-Starzyk, F.; Reynders, R.A.; Grobet, P.J.; Jacobs, P.A.; Bezoukhanova, C.P.; Sun, W.; Wu, Y. Stacked Phthalocyanines in VPI-5 Pores as Evidenced by CPDOR <sup>1</sup>H<sup>27</sup>Al NMR. *Mol. Catal. A* **1995**, *97*, 183–186. [[CrossRef](#)]
16. Kärger, J.; Keller, W.; Pfeifer, H.; Ernst, S.; Weitkamp, J. Unexpectedly Low Translational Mobility of Methane and Tetrafluoromethane in the Large-Pore Molecular Sieve VPI-5. *Microporous Mater.* **1995**, *3*, 401–408. [[CrossRef](#)]
17. Jin, Y.M.; Chon, H. A Novel Method for Encapsulation of Dyes into AlPO<sub>4</sub>-8 Molecular Sieve. *Chem. Commun.* **1996**, *1996*, 135–136. [[CrossRef](#)]
18. Ganschow, M.; Schulz-Ekloff, G.; Wark, M.; Wendschuh-Josties, M.; Wöhrle, D. Microwave-Assisted Preparation of Uniform Pure and Dye-Loaded AlPO<sub>4</sub>-5 Crystals with Different Morphologies for Use as Microlaser Systems. *J. Mater. Chem.* **2001**, *11*, 1823–1827. [[CrossRef](#)]
19. Gonzalez-Platas, J.; Breton, J.; Girardet, C. Physisorption in a Molecular Helicoidal Cavity: Application to AlPO<sub>4</sub>-5. *Langmuir* **1995**, *11*, 197–203. [[CrossRef](#)]

20. Hartmann, M.; Kevan, L. Generation of Ion-Exchange Capacity by Silicon Incorporation into the Aluminophosphate VPI-5/ $\text{AlPO}_4$ -5 Molecular Sieve System. *J. Chem. Soc. Faraday Trans.* **1996**, *92*, 3661–3667. [[CrossRef](#)]
21. Garcia-Carmona, J.; Fanovich, M.A.; Llibre, J.; Rodriguez-Clemente, R.; Domingo, C. Processing of Microporous VPI-5 Molecular Sieve by Using Supercritical  $\text{CO}_2$ : Stability and Adsorption Properties. *Microporous Mesoporous Mater.* **2000**, *54*, 127–137. [[CrossRef](#)]
22. Van Heyden, H.; Mintova, S.; Bein, T.  $\text{AlPO}_4$ -18 Nanocrystals Synthesized Under Microwave Irradiation. *J. Mater. Chem.* **2006**, *16*, 514–518. [[CrossRef](#)]
23. Shutilov, A.; Grenev, I.V.; Kikhtyanin, O.V.; Gavrilov, V.Y. Adsorption of Molecular Hydrogen on Aluminophosphate Zeolites at 77 K. *Kinet. Catal.* **2012**, *53*, 137–144. [[CrossRef](#)]
24. Weiß, O.; Loerke, J.; Wüstefeld, U.; Marlow, F.; Schüth, F.J. Host-Guest Interactions and Laser Activity in  $\text{AlPO}_4$ -5/Laser Dye Composites. *J. Solid State Chem.* **2002**, *67*, 302–309. [[CrossRef](#)]
25. Yao, M.; Wang, T.; Yao, Z.; Duan, D.; Chen, S.; Liu, Z.; Liu, R.; Lu, S.; Yuan, Y.; Zou, B.; et al. Pressure-Driven Topological Transformations of Iodine Confined in One-Dimensional Channels. *J. Phys. Chem. C* **2013**, *117*, 25052–25058. [[CrossRef](#)]
26. Guo, J.; Wang, C.; Xu, J.; Deng, J.; Yan, R.P.; Sharma, R.; Xu, R. Encapsulation of Bulky Solvent Molecules into the Channels of Aluminophosphate Molecular Sieve and its Negative Influence on the Thermal Stability of Open-Framework. *Inorg. Chem. Commun.* **2018**, *91*, 67–71. [[CrossRef](#)]
27. Carreon, M.L.; Li, S.; Carreon, M.A.  $\text{AlPO}_4$ -18 Membranes for  $\text{CO}_2/\text{CH}_4$  Separation. *Chem. Commun.* **2012**, *48*, 2310–2312. [[CrossRef](#)]
28. Wu, T.; Lucero, J.; Zong, Z.; Elsaidi, S.K.; Thallapally, P.K.; Carreon, M.A. Microporous Crystalline Membranes for Kr/Xe Separation: Comparison Between  $\text{AlPO}_4$ -18, SAPO-34, and ZIF-8. *ACS Appl. Nano Mater.* **2018**, *1*, 463–470. [[CrossRef](#)]
29. Wang, B.; Gao, F.; Zhang, F.; Xing, W.; Zhou, R. Highly Permeable and Oriented  $\text{AlPO}_4$ -18 Membranes Prepared Using Directly Synthesized Nanosheets for  $\text{CO}_2/\text{CH}_4$  Separation. *J. Mater. Chem. A* **2019**, *7*, 13164–13172. [[CrossRef](#)]
30. Tang, Z.K.; Sun, H.D.; Wang, J.; Li, J.C. Silver oxalate: Mechanical properties and extreme negative mechanical phenomena. *Appl. Phys. Lett.* **1998**, *73*, 2287–2289. [[CrossRef](#)]
31. Launois, P.; Moret, R.; Le Bolloc'h, D.; Albouya, P.A.; Tang, Z.K.; Li, G. Carbon Nanotubes Synthesised in Channels of  $\text{AlPO}_4$ -5 Single Crystals: First X-ray Scattering Investigations. *Solid State Commun.* **2000**, *116*, 99–103. [[CrossRef](#)]
32. Li, Z.M.; Tang, Z.K.; Liu, H.J.; Wang, N.; Chan, C.T.; Saito, R.; Okada, S.; Li, G.D.; Chen, J.S.; Nagasawa, N.; et al. Polarized Absorption Spectra of Single-Walled 4 Å Carbon Nanotubes Aligned in Channels of an  $\text{AlPO}_4$ -5 Single Crystal. *Phys. Rev. Lett.* **2001**, *87*, 127401. [[CrossRef](#)] [[PubMed](#)]
33. Li, G.D.; Tang, Z.K.; Wang, N.; Chen, J.S. Structural Study of the 0.4-nm Single-Walled Carbon Nanotubes Aligned in Channels of  $\text{AlPO}_4$ -5 crystal. *Carbon* **2002**, *40*, 917–921.
34. Zhai, J.P.; Tang, Z.K.; Li, Z.M.; Li, I.L.; Jiang, F.Y.; Shen, P.; Hu, X. Carbonization Mechanism of Tetrapropylammonium-hydroxide in Channels of  $\text{AlPO}_4$ -5 Single Crystals. *Chem. Mater.* **2006**, *18*, 1505–1511. [[CrossRef](#)]
35. Zhai, J.P.; Li, Z.M.; Liu, H.J.; Li, I.L.; Sheng, P.; Hu, H.J.; Tang, Z.K. Catalytic Effect of Metal Cations on the Formation of Carbon Nanotubes inside the Channels of  $\text{AlPO}_4$ -5 crystal. *Carbon* **2006**, *44*, 1151–1157. [[CrossRef](#)]
36. Yang, W.; Sun, W.; Zhao, S.; Yin, X. Single-Walled Carbon Nanotubes Prepared in Small  $\text{AlPO}_4$ -5 and CoAPO-5 Molecular Sieves by Low-Temperature Hydrocracking. *Microporous Mesoporous Mater.* **2016**, *219*, 87–92. [[CrossRef](#)]
37. Concepcion, P.; Lopez Nieto, J.M. Novel Synthesis of Vanadium Cobalt Aluminophosphate Molecular Sieve of AEI Structure (VCoAPO-18) and its Catalytic Behavior for Ethane Oxidation. *Catal. Commun.* **2001**, *2*, 363–367. [[CrossRef](#)]
38. Concepcion, P.; Blasco, T.; Lopez Nieto, J.M.; Vidal-Moya, A.; Martinez-Arias, A. Preparation, Characterization and Reactivity of V- and/or Co-Containing  $\text{AlPO}_4$ -18 Materials (VCoAPO-18) in the Oxidative Dehydrogenation of Ethane. *Microporous Mesoporous Mater.* **2004**, *67*, 215–227. [[CrossRef](#)]
39. Dai, W.; Li, N.; Guan, N.; Hunger, M. Unexpected Methanol-to-Olefin Conversion Activity of Low-Silica Aluminophosphate Molecular Sieves. *Catal. Commun.* **2011**, *16*, 124–127. [[CrossRef](#)]
40. Liu, D.; Zhang, B.; Liu, X.; Li, J. Cyclohexane Oxidation over AFI Molecular Sieves: Effects of Cr, Co Incorporation and Crystal Size. *Catal. Sci. Technol.* **2015**, *5*, 3394–3402. [[CrossRef](#)]
41. Preeth, M.E.; Umasankari, A.; Rekha, C.H.; Palanichamy, P.; Sivakumar, T.; Pandurangan, A. Selective Oxidation of Cyclohexane to KA Oil Over Ce- $\text{AlPO}_4$ -18 Molecular Sieves. *Int. J. Eng. Technol.* **2018**, *7*, 352–354. [[CrossRef](#)]
42. Chen, J.; Thomas, J.M.; Wright, P.A. Silicoaluminophosphate Number Eighteen (SAPO-18): A New Microporous Solid Acid Catalyst. *Catal. Lett.* **1994**, *28*, 241–248. [[CrossRef](#)]
43. Thomas, J.M.; Greaves, G.N.; Sanka, G.; Wright, P.A.; Chen, J.; Dent, A.J.; Marchese, L. On the Nature of the Active Site in a CoAPO-18 Solid Acid Catalyst. *Angew. Chem. Int. Ed.* **1994**, *33*, 1871–1873. [[CrossRef](#)]
44. Zubowa, H.L.; Richter, M.; Roost, U.; Parlitz, B.; Fricke, R. Synthesis and Catalytic Properties of Substituted  $\text{AlPO}_4$ -31 Molecular Sieves. *Catal. Lett.* **1993**, *19*, 67–79. [[CrossRef](#)]
45. Chen, Y.; Zhang, D.; Li, F.; Gao, F.; Feng, C.; Wen, S.; Ruan, S. Humidity Sensor Based on  $\text{AlPO}_4$ -5 Zeolite with High Responsivity and its Sensing Mechanism. *Sens. Actuators B* **2015**, *212*, 242–247. [[CrossRef](#)]
46. Ristic, A.; Logar, N.Z.; Henninger, S.K.; Kaucic, V. The Performance of Small-Pore Microporous Aluminophosphates in Low-Temperature Solar Energy Storage: The Structure–Property Relationship. *Adv. Funct. Mater.* **2012**, *22*, 1952–1957. [[CrossRef](#)]
47. Henninger, S.K.; Schmidt, F.P.; Henning, H.M. Water Adsorption Characteristics of Novel Materials for Heat Transformation Applications. *Applied Thermal Eng.* **2010**, *30*, 1692–1702. [[CrossRef](#)]

48. Henninger, S.K.; Schmidt, F.P.; Henning, H.M. Characterisation and Improvement of Sorption Materials with Molecular Modeling for the Use in Heat Transformation Applications. *Adsorption* **2011**, *17*, 833–843. [[CrossRef](#)]
49. Henninger, S.K.; Jeremias, F.; Kummer, H.; Schossig, P.; Henning, H.M. Novel Sorption Materials for Solar Heating and Cooling. *Energy Procedia* **2012**, *30*, 279–288. [[CrossRef](#)]
50. Khosrovani, N.; Sleight, A.W. Flexibility of Network Structures. *J. Solid State Chem.* **1996**, *121*, 2–11. [[CrossRef](#)]
51. Grima, J.N.; Jackson, R.; Alderson, A.; Evans, K.E. Do Zeolites Have Negative Poisson's Ratios? *Adv. Mater.* **2000**, *12*, 1912–1918. [[CrossRef](#)]
52. Grima, J.N.; Gatt, R.; Zammit, V.; Williams, J.J.; Evans, K.E.; Alderson, A.; Walton, R.I. Natrolite: A Zeolite with Negative Poisson's Ratios. *J. Appl. Phys.* **2007**, *101*, 086102. [[CrossRef](#)]
53. Sanchez-Valle, C.; Lethbridge, Z.A.D.; Sinogeikin, S.V.; Williams, J.J.; Walton, R.I.; Evans, K.E.; Bass, J.D. Negative Poisson's Ratios in Siliceous Zeolite MFI-Silicalite. *J. Chem. Phys.* **2008**, *128*, 184503. [[CrossRef](#)] [[PubMed](#)]
54. Sanchez-Valle, C.; Sinogeikin, V.; Lethbridge, Z.A.D.; Walton, R.I.; Smith, C.W.; Evans, K.E.; Bass, J.D. Brillouin Scattering Study on the Single Crystal of Natrolite and Analcime Zeolites. *J. Appl. Phys.* **2005**, *98*, 53508. [[CrossRef](#)]
55. Eroshenko, V.; Regis, R.C.; Soulard, M.; Patarin, J. Energetics: A New Field of Applications for Hydrophobic Zeolites. *J. Am. Chem. Soc.* **2001**, *123*, 8129–8130. [[CrossRef](#)] [[PubMed](#)]
56. Lee, Y.; Hriljac, J.A.; Vogt, T.; Parise, J.B.; Artioli, G. Phase Transition of Zeolite Rho at High-Pressure. *J. Am. Chem. Soc.* **2001**, *123*, 12732–12733. [[CrossRef](#)]
57. Lee, Y.; Vogt, T.; Hriljac, J.A.; Parise, J.B.; Artioli, G. Pressure-Induced Volume Expansion of Zeolites in the Natrolite Family. *J. Am. Chem. Soc.* **2002**, *124*, 5466–5475. [[CrossRef](#)]
58. Gatta, G.D.; Lee, Y. Zeolites at high pressure: A review. *Mineral. Mag.* **2014**, *78*, 267–291. [[CrossRef](#)]
59. Arletti, R.; Ferro, O.; Quartieri, S.; Sani, A.; Tabacchi, G.; Vezzolini, G. Structural Deformation Mechanisms of Zeolites under Pressure. *Am. Mineral.* **2003**, *88*, 1416–1422. [[CrossRef](#)]
60. Astala, R.; Auerbach, S.M.; Monson, P.A. Density Functional Theory Study of Silica Zeolite Structures: Stabilities and Mechanical Properties of SOD, LTA, CHA, MOR, and MFI. *J. Phys. Chem. B* **2004**, *108*, 9208–9215. [[CrossRef](#)]
61. Astala, R.; Auerbach, S.M.; Monson, P.A. Normal mode approach for predicting the mechanical properties of solids from first principles: Application to compressibility and thermal expansion of zeolites. *Phys. Rev. B* **2005**, *71*, 014112. [[CrossRef](#)]
62. Sartbaeva, A.; Wells, S.A.; Tracy, M.M.J.; Thorpe, M.F. The flexibility window in zeolites. *Nat. Mater.* **2006**, *5*, 962–965. [[CrossRef](#)] [[PubMed](#)]
63. Fletcher, R.E.; Wells, S.A.; Leung, K.M.; Edwards, P.P.; Sartbaeva, A. Intrinsic flexibility of porous materials; theory, modelling and the flexibility window of the EMT zeolite framework. *Acta Crystallogr. B* **2015**, *71*, 641–647. [[CrossRef](#)] [[PubMed](#)]
64. Coudert, F.X. Systematic investigation of the mechanical properties of pure silicazeolites: Stiffness, anisotropy, and negative linear compressibility. *Phys. Chem. Chem. Phys.* **2013**, *15*, 16012–16018. [[CrossRef](#)]
65. Evans, J.D.; Coudert, F.X. Predicting the Mechanical Properties of Zeolite Frameworks by Machine Learning. *Chem. Mater.* **2017**, *29*, 7833–7839. [[CrossRef](#)]
66. Gaillac, R.; Chibani, S.; Coudert, F.X. Speeding up discovery of auxetic zeolite frameworks by machine learning. *Chem. Mater.* **2020**, *32*, 2653–2663. [[CrossRef](#)]
67. Santoro, M.; Veremeienko, V.; Polisi, M.; Fantini, R.; Alabarse, F.; Arletti, R.; Quatieri, S.; Svitlyk, V.; Van der Lee, A.; Rouquette, J.; et al. Insertion and Confinement of H<sub>2</sub>O in Hydrophobic Siliceous Zeolites at High Pressure. *J. Phys. Chem. C* **2019**, *123*, 17432–17439. [[CrossRef](#)]
68. Bahr, D.F.; Reid, J.A.; Mook, W.M.; Bauer, C.A.; Stumpf, R.; Skulan, A.J.; Moody, N.R.; Simmons, B.A.; Shindel, M.M.; Allendorf, M.D. Mechanical properties of cubic zinc carboxylate IRMOF-1 metal-organic framework crystals. *Phys. Rev. B* **2007**, *76*, 184106. [[CrossRef](#)]
69. Chapman, K.W.; Halder, G.J.; Chupas, P.J. Pressure-Induced Amorphization and Porosity Modification in a Metal–Organic Framework. *J. Am. Chem. Soc.* **2009**, *131*, 17546–17547. [[CrossRef](#)]
70. Fairen-Jimenez, D.; Moggach, S.A.; Wharmby, T.; Wright, P.A.; Parsons, S.; Düren, S. Opening the Gate: Framework Flexibility in ZIF-8 Explored by Experiments and Simulations. *J. Am. Chem. Soc.* **2011**, *133*, 8900–8902. [[CrossRef](#)]
71. Li, W.; Probert, M.R.; Kosa, M.; Bennett, T.D.; Thirumurugan, A.; Burwood, R.P.; Parinello, M.; Howard, J.A.; Cheetham, A.K. Negative Linear Compressibility of a Metal–organic Framework. *J. Am. Chem. Soc.* **2012**, *134*, 11940–11943. [[CrossRef](#)]
72. Wu, H.; Yildirim, T.; Zhou, W.J. Exceptional Mechanical Stability of Highly Porous Zirconium Metal–Organic Framework UiO-66 and Its Important Implications. *J. Phys. Chem. Lett.* **2013**, *4*, 925–930. [[CrossRef](#)]
73. Ortiz, A.U.; Boutin, A.; Fuchs, A.H.; Coudert, F.X. Anisotropic Elastic Properties of Flexible Metal–Organic Frameworks: How Soft are Soft Porous Crystals? *Phys. Rev. Lett.* **2012**, *109*, 195502. [[CrossRef](#)] [[PubMed](#)]
74. Ortiz, A.U.; Boutin, A.; Fuchs, A.H.; Coudert, F.X. Organic Frameworks with Wine-Rack Motif: What Determines their Flexibility and Elastic Properties? *J. Chem. Phys.* **2013**, *138*, 174703. [[CrossRef](#)]
75. Ortiz, A.U.; Boutin, A.; Fuchs, A.H.; Coudert, F.X. Investigating the Pressure-Induced Amorphization of Zeolitic Imidazolate Framework ZIF-8: Mechanical Instability Due to Shear Mode Softening. *J. Phys. Chem. Lett.* **2013**, *4*, 1861–1865. [[CrossRef](#)] [[PubMed](#)]
76. Coudert, F.X. Responsive Metal–Organic Frameworks and Framework Materials: Under Pressure, Taking the Heat, in the Spotlight, with Friends. *Chem. Mater.* **2015**, *27*, 1905–1916. [[CrossRef](#)]

77. Cai, W.; Katrusiak, A. Giant negative linear compression positively coupled to massive thermal expansion in a metal–organic framework. *Chem. Commun.* **2014**, *5*, 4337–4342. [[CrossRef](#)]
78. Cai, W.; Gładysiak, A.; Anioła, M.; Smith, V.J.; Barbour, L.J.; Katrusiak, A. Giant Negative Area Compressibility Tunable in a Soft Porous Framework Material. *J. Am. Chem. Soc.* **2015**, *137*, 9296–9301. [[CrossRef](#)]
79. Serra-Crespo, P.; Dikhtiarenko, A.; Stavitski, E.; Juan-Alcañiz, J.; Kapteijn, F.; Coudert, F.X.; Gascon, J. Experimental evidence of negative linear compressibility in the MIL-53 metal–organic framework family. *CrystEngComm* **2015**, *17*, 276–280. [[CrossRef](#)]
80. Tan, J.C.; Bennett, T.D.; Cheetham, A.K. Chemical structure, network topology, and porosity effects on the mechanical properties of Zeolitic Imidazolate Frameworks. *Proc. Natl. Acad. Sci. USA* **2010**, *107*, 9938–9943. [[CrossRef](#)]
81. Tan, J.C.; Cheetham, A.K. Mechanical properties of hybrid inorganic–organic framework materials: Establishing fundamental structure–property relationships. *Chem. Soc. Rev.* **2011**, *40*, 1059–1080. [[CrossRef](#)]
82. Tan, J.C.; Civalieri, B.; Lin, C.C.; Valenzano, L.; Galvelis, R.; Chen, P.F.; Bennett, T.D.; Mellot-Draznieks, C.; Zicovich-Wilson, C.M.; Cheetham, A.K. Exceptionally Low Shear Modulus in a Prototypical Imidazole-Based Metal–Organic Framework. *Phys. Rev. Lett.* **2012**, *108*, 095502. [[CrossRef](#)] [[PubMed](#)]
83. Ryder, M.R.; Tan, J.C. Explaining the mechanical mechanisms of zeolitic metal–organic frameworks: Revealing auxeticity and anomalous elasticity. *Dalton Trans.* **2016**, *45*, 4154–4161. [[CrossRef](#)] [[PubMed](#)]
84. Yot, P.G.; Boudene, Z.; Macia, J.; Granier, D.; Vanduyfhuys, L.; Verstraelen, T.; Speybroeck, V.V.; Devic, T.; Serre, C.; Ferey, G.; et al. Metal–organic frameworks as potential shock absorbers: The case of the highly flexible MIL-53(Al). *Chem. Commun.* **2014**, *50*, 9462–9464. [[CrossRef](#)] [[PubMed](#)]
85. Banlusan, K.; Antillon, E.; Strachan, A. Mechanisms of Plastic Deformation of Metal–Organic Framework-5. *J. Phys. Chem. C* **2015**, *119*, 25845–25852. [[CrossRef](#)]
86. Banlusan, K.; Amornkitbamrung, V. J Effects of Free Volume on Shock-Wave Energy Absorption in A Metal–Organic Framework: A Molecular Dynamics Investigation. *Phys. Chem. C* **2020**, *124*, 17027–17038. [[CrossRef](#)]
87. Fraux, G.; Coudert, F.X.; Boutin, A.; Fuchs, A.H. Forced intrusion of water and aqueous solutions in microporous materials: From fundamental thermodynamics to energy storage devices. *Chem. Soc. Rev.* **2017**, *46*, 7421–7437. [[CrossRef](#)]
88. Terracina, A.; Todaro, M.; Mazaj, M.; Agnello, S.; Gelardi, F.M.; Buscarino, G. Unveiled the Source of the Structural Instability of HKUST-1 Powders upon Mechanical Compaction: Definition of a Fully Preserving Tableting Method. *J. Phys. Chem. C* **2019**, *123*, 1730–1741. [[CrossRef](#)]
89. Redfern, L.R.; Robison, L.; Wasson, M.C.; Goswami, S.; Lyu, J.; Islamoglu, T.; Chapman, K.W.; Farha, O.K. Isolating the Role of the Node-Linker Bond in the Compression of UiO-66 Metal–Organic Frameworks. *J. Am. Chem. Soc.* **2019**, *141*, 4365–4371. [[CrossRef](#)]
90. Moghadam, P.Z.; Rogge, S.M.; Li, A.; Chow, C.M.; Wieme, J.; Moharrami, N.; Aragones-Anglada, M.; Conduit, G.; Gomez-Gualdrón, D.A.; Van Speybroeck, V.; et al. Structure-Mechanical Stability Relations of Metal–Organic Frameworks via Machine Learning. *Matter* **2019**, *19*, 219–234. [[CrossRef](#)]
91. Zhou, X.; Miao, Y.; Suslick, K.S.; Dlott, D.D. Mechanochemistry of Metal–Organic Frameworks under Pressure and Shock. *Acc. Chem. Res.* **2020**, *53*, 2806–2815. [[CrossRef](#)]
92. Zeng, Q.; Wang, K.; Qiao, Y.; Li, X.; Zou, B. Negative Linear Compressibility Due to Layer Sliding in a Layered Metal–Organic Framework. *J. Phys. Chem. Lett.* **2017**, *8*, 1436–1441. [[CrossRef](#)] [[PubMed](#)]
93. Zeng, Q.; Wang, K.; Zou, B. Large Negative Linear Compressibility in InH(BDC)<sub>2</sub> from Framework Hinging. *J. Am. Chem. Soc.* **2017**, *139*, 15648–15651. [[CrossRef](#)]
94. Zeng, Q.; Wang, K.; Zou, B. Negative Linear Compressibility Response to Pressure in Multitype Wine-Rack Metal–Organic Frameworks. *ACS Mater. Lett.* **2020**, *2*, 291–295. [[CrossRef](#)]
95. Yan, Y.; O'Connor, A.E.; Kanthasamy, G.; Atkinson, G.; Allan, D.R.; Blake, A.J.; Schroder, M. Unusual and Tunable Negative Linear Compressibility in the Metal–Organic Framework MFM-133(M) (M = Zr, Hf). *J. Am. Chem. Soc.* **2018**, *140*, 3952–3958. [[CrossRef](#)] [[PubMed](#)]
96. Feng, G.; Zhang, W.; Dong, L.; Li, W.; Cai, W.; Wei, W.; Ji, L.; Lin, Z.; Lu, P. Negative area compressibility of a hydrogen bonded two-dimensional material. *Chem. Sci.* **2019**, *10*, 1309–1315. [[CrossRef](#)] [[PubMed](#)]
97. Chen, Z.; Xu, B.; Li, Q.; Meng, Y.; Quan, Z.; Zou, B. Selected Negative Linear Compressibilities in the Metal–Organic Framework of [Cu(4,4'-bpy)<sub>2</sub>(H<sub>2</sub>O)<sub>2</sub>]-SiF<sub>6</sub>. *Inorg. Chem.* **2020**, *59*, 1715–1722. [[CrossRef](#)]
98. Zajdel, P.; Chorążewski, M.; Leão, J.B.; Jensen, G.V.; Bleuel, M.; Zhang, H.F.; Feng, T.; Luo, D.; Li, M.; Lowe, A.R.; et al. Inflation Negative Compressibility during Intrusion–Extrusion of a Non-Wetting Liquid into a Flexible Nanoporous Framework. *Phys. Chem. Lett.* **2021**, *12*, 4951–4957. [[CrossRef](#)]
99. Tortora, M.; Zajdel, P.; Lowe, A.R.; Chorążewski, M.; Leão, J.B.; Jensen, G.V.; Bleuel, M.; Giacomello, M.; Casciola, C.M.; Meloni, S.; et al. Giant Negative Compressibility by Liquid Intrusion into Superhydrophobic Flexible Nanoporous Frameworks. *Nano Lett.* **2021**, *21*, 2848–2853. [[CrossRef](#)]
100. Colmenero, F. Negative Linear Compressibility in Nanoporous Metal–Organic Frameworks Rationalized by the Empty Channel Structural Mechanism. *Phys. Chem. Chem. Phys.* **2021**, *23*, 8508–8524. [[CrossRef](#)]
101. Colmenero, F.; Lobato, A.; Timón, V. Compressing the Channels in the Crystal Structure of Copper Squarate Metal–Organic Framework. *Solids* **2022**, *3*, 374–384. [[CrossRef](#)]
102. Zeng, Q.; Wang, K.; Zou, B. Near Zero Area Compressibility in a Perovskite-Like Metal–Organic Frameworks [C(NH<sub>2</sub>)<sub>3</sub>][Cd(HCOO)<sub>3</sub>]. *ACS Appl. Mater. Interfaces* **2018**, *10*, 23481–23484. [[CrossRef](#)] [[PubMed](#)]

103. Yu, Y.; Zeng, Q.; Chen, Y.; Jiang, L.; Wang, K.; Zou, B. Extraordinarily Persistent Zero Linear Compressibility in Metal-Organic Framework MIL-122(In). *ACS Mater. Lett* **2020**, *2*, 519–523. [[CrossRef](#)]
104. Zhang, X.; Sui, Z.; Xu, B.; Yue, S.; Luo, Y.; Zhan, W.; Liu, B.A. Mechanically strong and highly conductive graphene aerogel and its use as electrodes for electrochemical power source. *J. Mater. Chem.* **2011**, *21*, 6494–6497. [[CrossRef](#)]
105. Mecklenburg, M.; Schuchardt, A.; Mishra, Y.K.; Kaps, S.; Adelung, R.; Lotnyk, A.; Kienle, L.; Schulte, K. Aerographite: Ultra Lightweight, Flexible Nanowall, Carbon Microtube Material with Outstanding Mechanical Performance. *Adv. Mater.* **2012**, *24*, 3486–3490. [[CrossRef](#)]
106. Worsley, M.A.; Kucheyev, S.O.; Mason, H.E.; Merrill, M.D.; Mayer, B.P.; Lewicki, J.; Valdez, C.A.; Suss, M.E.; Stadermann, M.; Pauzaskie, M.J.; et al. Mechanically robust 3D graphene macroassembly with high surface area. *Chem. Commun.* **2012**, *48*, 8428–8430. [[CrossRef](#)] [[PubMed](#)]
107. Hu, H.; Zhao, Z.; Wan, W.; Gogotsi, Y.; Qiu, J. Ultralight and Highly Compressible Graphene Aerogels. *Adv. Mater.* **2013**, *25*, 2219–2223. [[CrossRef](#)]
108. Zhu, C.; Han, T.Y.; Duoss, E.B.; Golobic, A.M.; Kuntz, J.; Spadaccini, C.M.; Worsley, M.A. Highly compressible 3D periodic graphene aerogel microlattices. *Nat. Commun.* **2015**, *6*, 6962. [[CrossRef](#)]
109. Lei, J.; Liu, Z. The structural and mechanical properties of graphene aerogels based on Schwarz-surface-like graphene models. *Carbon* **2018**, *130*, 741–748. [[CrossRef](#)]
110. Wu, Y.; Yi, N.; Huang, L.; Zhang, T.; Fang, S.; Chang, H.; Li, N.; Oh, J.; Lee, J.A.; Kozlov, M. Three-dimensionally bonded spongy graphene material with super compressive elasticity and near-zero Poisson's ratio. *Nat. Commun.* **2015**, *6*, 6141. [[CrossRef](#)]
111. Chen, B.; Ma, Q.; Tan, C.; Lim, T.T.; Huang, L.; Zhang, H. Carbon-Based Sorbents with Three-Dimensional Architectures for Water Remediation. *Small* **2015**, *11*, 3319–3336. [[CrossRef](#)]
112. Xu, X.; Zhang, Q.; Yu, Y.; Chen, W.; Hu, H.; Li, H. Naturally Dried Graphene Aerogels with Superelasticity and Tunable Poisson's Ratio. *Adv. Mater.* **2016**, *28*, 9223–9230. [[CrossRef](#)] [[PubMed](#)]
113. Robertson, M.C.; Mokaya, R. Microporous activated carbon aerogels via a simple subcritical drying route for CO<sub>2</sub> capture and hydrogen storage. *Microporous Mesoporous Mater.* **2013**, *179*, 151–156. [[CrossRef](#)]
114. Patil, S.P.; Shendye, P.; Markert, B. Molecular investigation of mechanical properties and fracture behavior of graphene aerogel. *J. Phys. Chem. B* **2020**, *124*, 6132–6139. [[CrossRef](#)] [[PubMed](#)]
115. Patil, S.P.; Kulkarni, A.; Markert, B. Shockwave response of graphene aerogels: An all-atom simulation study. *Comput. Mater. Sci.* **2021**, *189*, 110252. [[CrossRef](#)]
116. Cho, H.J.; Kim, I.D.; Jung, S.M. Multifunctional Inorganic Nanomaterial Aerogel Assembled into fSWNT Hydrogel Platform for Ultrasensitive NO<sub>2</sub> Sensing. *ACS Appl. Mater. Interfaces* **2020**, *12*, 10637–10647. [[CrossRef](#)]
117. Barthelet, K.; Marrot, J.; Riou, D.; Férey, G. A Breathing Hybrid Organic-Inorganic Solid with Very Large Pores and High Magnetic Characteristics. *Angew. Chem. Int. Ed.* **2022**, *41*, 281–284. [[CrossRef](#)]
118. Bradshaw, D.; Claridge, J.B.; Cussen, E.J.; Prior, T.J.; Rosseinsky, M. Design, Chirality, and Flexibility in Nanoporous Molecule-Based Materials. *J. Acc. Chem. Res.* **2005**, *38*, 273–282. [[CrossRef](#)]
119. Serre, C.; Mellot-Draznieks, C.; Surble, C.; Audebrand, N.; Filinchuk, Y.; Férey, G. Role of Solvent-Host Interactions That Lead to Very Large Swelling of Hybrid Frameworks. *Science* **2007**, *315*, 1828–1831. [[CrossRef](#)]
120. Férey, G.; Serre, C. Large breathing effects in three-dimensional porous hybrid matter: Facts, analyses, rules and consequences. *Chem. Soc. Rev.* **2009**, *38*, 1380–1399. [[CrossRef](#)]
121. Sato, H.; Kosaka, W.; Matsuda, R.; Hori, A.; Hijikata, Y.; Belosludov, R.V.; Sakaki, S.; Takata, M.; Kitagawa, S. Self-Accelerating CO Sorption in a Soft Nanoporous Crystal. *Science* **2014**, *343*, 167–170. [[CrossRef](#)]
122. Sanchez-Gonzalez, E.; Mileo, P.G.M.; Sagastuy-Breña, M.; Raziell-Alvarez, J.; Reynolds, J.E.; Villarreal, A.; Gutierrez-Alejandre, A.; Ramirez, J.; Balmaseda, J.; González-Zamora, E.; et al. Highly reversible sorption of H<sub>2</sub>S and CO<sub>2</sub> by an environmentally friendly Mg-based MOF. *J. Mater. Chem. A* **2018**, *6*, 16900–16909. [[CrossRef](#)]
123. Remy, T.; Baron, G.V.; Denayer, J.F.M. Modeling the Effect of Structural Changes during Dynamic Separation Processes on MOFs. *Langmuir* **2011**, *27*, 13064–13071. [[CrossRef](#)] [[PubMed](#)]
124. Remy, T.; Ma, L.; Maes, M.; De Vos, D.E.; Baron, G.V.; Denayer, J.F.M. Vapor-Phase Adsorption and Separation of Ethylbenzene and Styrene on the Metal–Organic Frameworks MIL-47 and MIL-53(Al). *Ind. Eng. Chem. Res.* **2012**, *51*, 14824–14833. [[CrossRef](#)]
125. Horcajada, P.; Serre, C.; Maurin, G.; Ramsahye, N.A.; Balas, F.; Vallet-Regi, M.; Sebban, M.; Taulelle, F.; Férey, G. Flexible Porous Metal-Organic Frameworks for a Controlled Drug Delivery. *J. Am. Chem. Soc.* **2008**, *130*, 6774–6780. [[CrossRef](#)]
126. Millange, F.; Serre, C.; Guillou, N.; Férey, G.; Walton, R.I. Structural Effects of Solvents on the Breathing of Metal–Organic Frameworks: An In Situ Diffraction Study. *Angew. Chem. Int. Ed.* **2008**, *47*, 4100–4105. [[CrossRef](#)] [[PubMed](#)]
127. Allendorf, M.D.; Houk, R.J.T.; Andruszkiewicz, L.; Talin, A.; Pikarsky, J.; Choudhury, A.; Gall, K.A.; Hesketh, P.J. Stress-induced chemical detection using flexible metal-organic frameworks. *J. Am. Chem. Soc.* **2008**, *130*, 14404–14405. [[CrossRef](#)] [[PubMed](#)]
128. Yot, P.G.; Vanduyfhuys, L.; Alvarez, E.; Rodriguez, J.; Itié, J.P.; Fabry, P.; Guillou, N.; Devic, T.; Beurroies, I.; Llewellyn, P.L.; et al. Metal–Organic Frameworks as Potential Shock Absorbers: The Case of The Highly Flexible MIL-53(Al). *Chem. Sci.* **2016**, *7*, 446–450. [[CrossRef](#)]
129. Baughman, R.H.; Stafstrom, S.; Cui, C.; Dantas, S.O. Compressibilities in One or More Dimensions. *Science* **1998**, *279*, 1522–1524. [[CrossRef](#)]

130. Lakes, R.S.; Wojciechowski, K.W. Negative Compressibility, Negative Poisson's Ratio and Stability. *Phys. Stat. Sol. B* **2008**, *245*, 545–551. [[CrossRef](#)]
131. Cairns, A.B.; Goodwin, A.L. Negative Linear Compressibility. *Phys. Chem. Chem. Phys.* **2015**, *17*, 20449–20465. [[CrossRef](#)]
132. Xie, Y.M.; Yang, X.; Shen, J.; Yan, X.; Ghaedizadeh, A.; Rong, J.; Huang, X.; Zhou, S. Designing orthotropic materials for negative or zero compressibility. *Int. J. Solids Struct.* **2014**, *51*, 4038–4051. [[CrossRef](#)]
133. Jiang, X.; Yang, Y.; Molokeev, M.S.; Gong, L.; Liang, F.; Wang, S.; Liu, L.; Wu, X.; Li, X.; Wu, S.; et al. Zero Linear Compressibility in Nondense Borates with a “Lu-Ban Stool”-Like Structure. *Adv. Mater.* **2018**, *30*, 1801313. [[CrossRef](#)]
134. Jiang, X.; Molokeev, M.S.; Dong, L.; Dong, Z.; Wang, N.; Kang, L.; Li, X.; Li, Y.; Tian, C.; Peng, S.; et al. Anomalous mechanical materials squeezing three-dimensional volume compressibility into one dimension. *Nat. Commun.* **2020**, *11*, 5593. [[CrossRef](#)] [[PubMed](#)]
135. Wang, L.; Dove, M.T.; Shi, J.; Sun, B.; Hu, D.; Wang, D. Adjustable uniaxial zero thermal expansion and zero linear compressibility in unique hybrid semiconductors: The role of the organic chain. *Dalton Trans.* **2020**, *49*, 719–728. [[CrossRef](#)] [[PubMed](#)]
136. Lakes, R.S. Foam Structures with a Negative Poisson's Ratio. *Science* **1987**, *235*, 1038–1040. [[CrossRef](#)] [[PubMed](#)]
137. Wojciechowski, K.W. Constant thermodynamic tension Monte Carlo studies of elastic properties of a two-dimensional system of hard cyclic hexamers. *Mol. Phys.* **1987**, *61*, 1247–1258. [[CrossRef](#)]
138. Lakes, R.S. Negative-Poisson's-Ratio Materials: Auxetic Solids. *Annu. Rev. Mater. Res.* **2017**, *47*, 63–81. [[CrossRef](#)]
139. Evans, K.E.; Alderson, A. Auxetic Materials: Functional Materials and Structures from Lateral Thinking! *Adv. Mater.* **2000**, *12*, 617–628. [[CrossRef](#)]
140. Spinks, G.M.; Wallace, G.G.; Fifield, L.S.; Dalton, L.R.; Mazzoldi, A.; De Rossi, D.; Khayrullin, I.I.; Baughman, R.H. Pneumatic Carbon Nanotube Actuators. *Adv. Mater.* **2002**, *14*, 1728–1732. [[CrossRef](#)]
141. Nicolaou, Z.G.; Motter, A.E. Mechanical Metamaterials with Negative Compressibility Transitions. *Nat. Mater.* **2012**, *11*, 608–613. [[CrossRef](#)]
142. Cairns, A.B.; Catafesta, J.; Levelut, C.; Rouquette, J.; Lee, A.; Peters, V.D.; Thompson, A.L.; Dmitriev, V.; Haines, J.; Goodwin, A.L. Giant Negative Linear Compressibility in Zinc Dicyanoaurate. *Nat. Mater.* **2013**, *12*, 212–216. [[CrossRef](#)] [[PubMed](#)]
143. Fang, N.; Xi, D.; Xu, J.; Ambati, M.; Srituravanich, W.; Sun, C.; Zhang, X. Ultrasonic metamaterials with negative modulus. *Nat. Mater.* **2006**, *5*, 452–456. [[CrossRef](#)] [[PubMed](#)]
144. Aliev, A.V.; Oh, J.; Kozlov, M.E.; Kuznetsov, A.A.; Fang, S.; Fonseca, A.F.; Ovalle, R.; Lima, M.D.; Haque, M.H.; Gartstein, Y.N.; et al. Giant-Stroke, Superelastic Carbon Nanotube Aerogel Muscles. *Science* **2009**, *323*, 1575–1578. [[CrossRef](#)]
145. Uhoya, W.; Tsoi, G.; Vohra, Y.K.; McGuire, M.A.; Sefat, A.S.; Sales, B.C.; Mandrus, D.; Weir, S.T. anomalous Compressibility Effects and Superconductivity of  $\text{EuFe}_2\text{As}_2$  under High Pressures. *J. Phys. Cond. Matter.* **2010**, *22*, 292202. [[CrossRef](#)] [[PubMed](#)]
146. Alderson, A.; Rasburn, J.; Ameer-Beg, S.; Mullarkey, P.G.; Perrie, W.; Evans, K.E. An auxetic filter: A tuneable filter displaying enhanced size selectivity or defouling properties. *Ind. Eng. Chem. Res.* **2000**, *39*, 654–665. [[CrossRef](#)]
147. Alderson, A.; Rasburn, J.; Evans, K.E.; Grima, J.N. Modelling of the mechanical and mass transport properties of auxetic molecular sieves: An idealised organic (polymeric honeycomb) host–guest system. *Membr. Technol.* **2001**, *137*, 6–8. [[CrossRef](#)]
148. Rasburn, J.; Alderson, A.; Ameer-Beg, S.; Mullarkey, P.G.; Perrie, W.; Evans, K.E.; Perrie, W.; Evans, K.E. Auxetic structures for variable permeability systems. *AIChE J.* **2001**, *47*, 2623–2626. [[CrossRef](#)]
149. Greaves, G.N.; Meneau, F.; Sapelkin, A.; Colyer, L.M.; Gwynn, I.; Wade, S.; Sankar, G. The Rheology of Collapsing Zeolites Amorphized by Temperature and Pressure. *Nat. Mater.* **2003**, *2*, 622–628. [[CrossRef](#)]
150. Haines, J.; Levelut, C.; Isambert, A.; Hebert, P.; Kohara, S.; Keen, D.A.; Hamouda, T.; Andraul, D. Topologically Ordered Amorphous Silica Obtained from the Collapsed Siliceous Zeolite, Silicalite-1-F, A Step toward Perfect Glasses. *J. Am. Chem. Soc.* **2009**, *131*, 12333–12338. [[CrossRef](#)]
151. Wang, L.; Wang, W.; Chen, L.; Shen, Z. Formation of a unique glass by spark plasma sintering of a zeolite. *J. Mater. Res.* **2009**, *24*, 3241–3245. [[CrossRef](#)]
152. Moggach, S.A.; Bennett, T.D.; Cheetham, A.K. The Effect of Pressure on ZIF-8: Increasing Pore Size with Pressure and the Formation of a High-Pressure Phase at 1.47 GPa. *Angew. Chem.* **2009**, *121*, 7221–7223. [[CrossRef](#)]
153. Hwang, G.C.; Shin, T.J.; Blom, D.A.; Vogt, T.; Lee, Y. Pressure-Induced Amorphization of Small Pore Zeolites—The Role of Cation-H<sub>2</sub>O Topology and Antiglass Formation. *Sci. Rep.* **2015**, *5*, 15056. [[CrossRef](#)] [[PubMed](#)]
154. Santoro, M.; Gorelli, F.; Haines, J.; Cambon, O.; Levelut, C.; Garbarino, G. Silicon carbonate phase formed from carbon dioxide and silica under pressure. *Proc. Natl. Acad. Sci. USA* **2011**, *108*, 7689–7692. [[CrossRef](#)] [[PubMed](#)]
155. Santoro, M.; Gorelli, F.A.; Bini, R. Carbon enters silica forming a cristobalite-type CO<sub>2</sub>-SiO<sub>2</sub> solid solution. *Nat. Commun.* **2013**, *4*, 1557. [[CrossRef](#)] [[PubMed](#)]
156. Santoro, M.; Gorelli, F.; Bini, R.; Salamat, A.; Garbarino, G.; Levelut, C.; Cambon, O.; Haines, J. High-Pressure Synthesis of a Polyethylene/Zeolite Nano-Composite Material. *Nat. Commun.* **2014**, *5*, 3761. [[CrossRef](#)]
157. Jorda, J.F.; Rey, F.; Sastre, G.; Valencia, S.; Palomino, M.; Corma, A.; Segura, A.; Errandonea, D.; Lacomba, R.; Manjon, F.J.; et al. Synthesis of a Novel Zeolite through a Pressure-Induced Reconstructive Phase Transition Process. *Angew. Chem. Int. Ed.* **2013**, *125*, 10652–10656. [[CrossRef](#)]
158. Zhou, R.; Qu, B.; Dai, J.; Zeng, X.C. Unravelling the crystal structure of the high-pressure phase of silicon carbonate. *Phys. Rev. X* **2014**, *4*, 011030.

159. Marques, M.; Morales-Garcia, A.; Menendez, J.M.; Baonza, V.G.; Recio, J.M. A novel crystalline SiCO compound. *Phys. Chem. Chem. Phys.* **2015**, *17*, 25055–25060. [[CrossRef](#)]
160. Santamaria-Perez, D.; Marqueño, T.; MacLeod, S.; Ruiz-Fuertes, J.; Daisenberger, D.; Chuliá-Jordan, R.; Errandonea, D.; Jordá, J.L.; Rey, F.; McGuire, C.; et al. Structural Evolution of CO<sub>2</sub>-Filled Pure Silica LTA Zeolite under High- Pressure High-Temperature Conditions. *Chem. Mater.* **2017**, *29*, 4502–4510. [[CrossRef](#)]
161. Marqueño, T.; Santamaria-Perez, D.; Ruiz-Fuertes, J.; Chuliá-Jordán, R.; Jordá, J.L.; Rey, F.; McGuire, C.; Kavner, A.; MacLeod, A.S.; Daisenberger, D.; et al. An Ultrahigh CO<sub>2</sub>-Loaded Silicalite-1 Zeolite: Structural Stability and Physical Properties at High Pressures and Temperatures. *Inorg. Chem.* **2018**, *57*, 6447–6455. [[CrossRef](#)]
162. Thibaud, J.M.; Rouquette, J.; Hermet, P.; Dziubek, K.; Gorelli, M.; Santoro, M.; Garbarino, G.; Alabarse, F.G.; Cambon, O.; Di Renzo, F.; et al. Saturation of the Siliceous Zeolite TON with Neon at High Pressure. *J. Phys. Chem. C* **2017**, *121*, 4283–4292. [[CrossRef](#)]
163. Tan, C.; Liu, Z.; Yonezawa, Y.; Sukenaga, S.; Ando, M.; Shibata, H.; Sasaki, Y.; Okubo, T.; Wakihara, T. Unique Crystallization Behavior in Zeolite Synthesis under External High Pressures. *Chem. Commun.* **2020**, *56*, 2811–2814. [[CrossRef](#)]
164. Deneyer, A.; Ke, J.; Devos, M.; Dusselier, M. Zeolite Synthesis under Nonconventional Conditions: Reagents, Reactors, and Modi Operandi. *Chem. Mater.* **2020**, *32*, 4884–4919. [[CrossRef](#)]
165. Lv, H.; Yao, M.; Li, Q.; Liu, R.; Liu, B.; Lu, S.; Jiang, L.; Cui, W.; Liu, Z.; Liu, J.; et al. The structural stability of AlPO<sub>4</sub>-5 zeolite under pressure: Effect of the pressure transmission medium. *J. Appl. Phys.* **2012**, *111*, 112615. [[CrossRef](#)]
166. Kim, T.; Lee, Y.; Jang, Y.N.; Shin, J.; Hong, S.B. Contrasting high-pressure compression behaviors of AlPO<sub>4</sub>-5 and SSZ-24 with the same AFI framework topology. *Microporous Mesoporous Mater.* **2013**, *169*, 42–46. [[CrossRef](#)]
167. Lotti, P.; Gatta, G.D.; Comboni, D.; Merlini, M.; Pastero, L.; Hanfland, M. AlPO<sub>4</sub>-5 zeolite at high pressure: Crystal-fluid interaction and elastic behavior. *Microporous Mesoporous Mater.* **2016**, *228*, 158–167. [[CrossRef](#)]
168. Alabarse, F.G.; Silly, G.; Haidoux, A.; Levelut, C.; Bourgogne, D.; Flank, A.M.; Lagarde, P.; Pereira, A.S.; Bantignies, J.L.; Cambon, O.; et al. Effect of H<sub>2</sub>O on the Pressure-Induced Amorphization of AlPO<sub>4</sub>-54·xH<sub>2</sub>O. *Phys. Chem. C* **2014**, *118*, 3651–3663. [[CrossRef](#)]
169. Alabarse, F.G.; Brubach, J.; Roy, P.; Haidoux, A.; Levelut, C.; Bantignies, J.L.; Cambon, O.; Haines, J. AlPO<sub>4</sub>-54 – AlPO<sub>4</sub>-8 Structural Phase Transition and Amorphization under High Pressure. Mechanism of H<sub>2</sub>O Insertion and Chemical Bond Formation in AlPO<sub>4</sub>-54·xH<sub>2</sub>O at High Pressure. *J. Phys. Chem. C* **2015**, *119*, 7771–7779. [[CrossRef](#)]
170. Alabarse, F.G.; Rouquette, J.; Coasne, B.; Haidoux, A.; Paulmann, C.; Cambon, O.; Haines, J. Mechanism of H<sub>2</sub>O insertion and chemical bond formation in AlPO<sub>4</sub>(4)-54·xH<sub>2</sub>O at high pressure. *J. Am. Chem. Soc.* **2015**, *137*, 584–587. [[CrossRef](#)]
171. Alabarse, F.G.; Silly, G.; Brubach, J.B.; Roy, P.; Haidoux, A.; Levelut, C.; Bantignies, J.B.; Kohara, S.; Floch, S.L.; Cambon, O.; et al. Anomalous Compressibility and Amorphization in AlPO<sub>4</sub>-17, the Oxide with the Highest Negative Thermal Expansion. *Phys. Chem. C* **2017**, *121*, 6852–6863. [[CrossRef](#)]
172. Alabarse, F.G.; Joseph, B.; Lausi, A.; Haines, J. Effect of H<sub>2</sub>O on the Pressure-Induced Amorphization of Hydrated AlPO<sub>4</sub>-17. *Molecules* **2019**, *24*, 2864. [[CrossRef](#)] [[PubMed](#)]
173. Domenico, S.N. Elastic properties of unconsolidated porous sand reservoirs. *Geophysics* **1977**, *42*, 1339–1368. [[CrossRef](#)]
174. Eberhart-Phillips, D.; Han, D.; Zoback, M. Empirical relationships among seismic velocity, effective pressure, porosity, and clay content in sandstone. *Geophysics* **1989**, *54*, 82–89. [[CrossRef](#)]
175. Thomsen, L. Elastic Anisotropy Due to Aligned Cracks in Porous Rock. *Geophys. Prospect.* **1995**, *3*, 805–829. [[CrossRef](#)]
176. Dvorkin, J.; Nur, A. Elasticity of high-porosity sandstones: Theory for two North Sea data sets. *Geophysics* **1996**, *61*, 1363–1370. [[CrossRef](#)]
177. Nur, A.; Mavko, G.; Dvorkin, J.; Galmudi, D. Diagnosing high-porosity sandstones: Strength and permeability from porosity and velocity. *Lead. Edge* **1998**, *17*, 357–362. [[CrossRef](#)]
178. Schön, J.H. Chapter 6 Elastic Properties. In *Physical Properties of Rocks, A Workbook. Handbook of Petroleum Exploration and Production*; Schön, J.H., Ed.; Elsevier: Amsterdam, The Netherlands, 2011; Volume, 8, pp. 149–243.
179. Alonso, E.E.; Vaunat, J.; Gens, A. Modelling the mechanical behaviour of expansive clays. *Eng. Geol.* **1999**, *54*, 173–183. [[CrossRef](#)]
180. Åkesson, A.; Kristensson, O. Mechanical modeling of MX-80—Development of constitutive laws. *Phys. Chem. Earth* **2008**, *33*, S504–S507. [[CrossRef](#)]
181. Tisato, N.; Marelli, S. Laboratory measurements of the longitudinal and transverse wave velocities of compacted bentonite as a function of water content, temperature, and confining pressure. *J. Geophys. Res. Solid Earth* **2013**, *118*, 3380–3393. [[CrossRef](#)]
182. Keller, L.M. Porosity anisotropy of Opalinus Clay: Implications for the poroelastic behaviour. *Geophys. J. Int.* **2017**, *208*, 1443–1448. [[CrossRef](#)]
183. Kenigsberg, A.R.; Rivière, J.; Marone, C.; Saffer, D.M. Evolution of Elastic and Mechanical Properties during Fault Shear: The Roles of Clay Content, Fabric Development, and Porosity. *J. Geophys. Res. Solid Earth* **2019**, *124*, 10968–10982. [[CrossRef](#)]
184. Kenigsberg, A.R.; Rivière, J.; Marone, C.; Saffer, D.M. The Effects of Shear Strain, Fabric, and Porosity Evolution on Elastic and Mechanical Properties of Clay-Rich Fault Gouge. *J. Geophys. Res. Solid Earth* **2020**, *125*, e2019JB018612. [[CrossRef](#)]
185. Liu, K.; Sheng, J.; Zhang, Z. A simulation study of the effect of clay swelling on fracture generation and porosity change in shales under stress anisotropy. *Eng. Geol.* **2020**, *278*, 105829. [[CrossRef](#)]
186. Sveinsson, H.A.; Ning, F.; Cao, P.; Fang, B.; Malthe-Sørensen, A. Grain-Size-Governed Shear Failure Mechanism of Polycrystalline Methane Hydrates. *J. Phys. Chem. C* **2021**, *125*, 10034–10042. [[CrossRef](#)]

187. Yu, C.; Ji, S.; Li, Q. Effects of porosity on seismic velocities, elastic moduli and Poisson's ratios of solid materials and rocks. *J. Rock Mech. Geotech. Eng.* **2016**, *8*, 35–49. [[CrossRef](#)]
188. Brantut, N.; Stefanou, I.; Sulem, J. Dehydration-induced instabilities at intermediate depths in subduction zones. *J. Geophys. Res. Solid Earth* **2017**, *122*, 6087–6107. [[CrossRef](#)]
189. Born, M. On the Stability of Crystal Lattices. *Math. Proc. Camb. Phil. Soc.* **1940**, *36*, 160–172. [[CrossRef](#)]
190. Milstein, F. Theoretical elastic behaviour of crystals at large strains. *J. Mater. Sci.* **1980**, *15*, 1071–1084. [[CrossRef](#)]
191. Karki, B.B.; Ackland, G.J.; Crain, J. Elastic instabilities in crystals from ab initio stress–strain relations. *J. Phys. Condens. Matter* **1997**, *9*, 8579–8589. [[CrossRef](#)]
192. Mouhat, F.; Coudert, F.X. Necessary and Sufficient Elastic Stability Conditions in Various Crystal Systems. *Phys. Rev. B* **2014**, *90*, 224104. [[CrossRef](#)]
193. Gao, F. Hardness estimation of complex oxide materials. *Phys. Rev. B* **2004**, *69*, 094113. [[CrossRef](#)]
194. Šimůnek, A.; Vackář, J. Hardness of Covalent and Ionic Crystals: First-Principle Calculations. *Phys. Rev. Lett.* **2006**, *96*, 085501. [[CrossRef](#)] [[PubMed](#)]
195. Niu, H.; Wei, P.; Sun, Y.; Chen, C.X.; Franchini, C.; Li, D.; Li, Y. Electronic, optical, and mechanical properties of superhard cold-compressed phases of carbon. *Appl. Phys. Lett.* **2011**, *99*, 031901. [[CrossRef](#)]
196. Chen, X.Q.; Niu, H.; Li, D.; Li, Y. Modeling Hardness of Polycrystalline Materials and Bulk Metallic Glasses. *Intermetallics* **2011**, *19*, 1275–1281. [[CrossRef](#)]
197. Liu, X.; Wang, H.; Wang, W.; Fu, Z. Simple Method for the Hardness Estimation of Inorganic Crystals by the Bond Valence Model. *Inorg. Chem.* **2016**, *55*, 11089–11095. [[CrossRef](#)]
198. Pugh, S.F. Relations between the Elastic Moduli and the Plastic Properties of Polycrystalline Pure Metals. *Philos. Mag.* **1954**, *45*, 823–843. [[CrossRef](#)]
199. Pettifor, D.G. Theoretical predictions of structure and related properties of intermetallics. *Mater. Sci. Technol.* **1992**, *8*, 345–349. [[CrossRef](#)]
200. Niu, H.; Chen, X.Q.; Liu, P.; Xing, W.; Cheng, X.; Li, D.; Li, Y. Extra-electron induced covalent strengthening and generalization of intrinsic ductile-to-brittle criterion. *Sci. Rep.* **2012**, *2*, 718. [[CrossRef](#)]
201. Bouhadda, Y.; Djella, S.; Bououdina, M.; Fenineche, N.; Boudouma, Y. Structural and Elastic Properties of LiBH<sub>4</sub> for Hydrogen Storage Applications. *J. Alloys Compd.* **2012**, *534*, 20–24. [[CrossRef](#)]
202. Gschneidner, K.; Russell, A.; Pecharsky, A.; Morris, J.; Zhang, Z.; Lograsso, T.; Hsu, D.; Lo, H.C.; Ye, Y.; Slager, A.; et al. A family of ductile intermetallic compounds. *Nat. Mater.* **2003**, *2*, 587–591. [[CrossRef](#)]
203. Ritchie, R.O. The conflicts between strength and toughness. *Nat. Mater.* **2011**, *10*, 817–822. [[CrossRef](#)] [[PubMed](#)]
204. Hwang, E.; Cuddy, E.; Lin, J.; Kaufman, J.L.; Shaw, A.; Conway, P.L.J.; Pribram-Jones, A.; Laws, K.J.; Bassman, L. Predicting ductility in quaternary -like alloys. *Phys. Rev. Mater.* **2021**, *5*, 033604. [[CrossRef](#)]
205. Zener, C. *Elasticity and Anelasticity of Metals*; University of Chicago Press: Chicago, IL, USA, 1948.
206. Chung, D.H.; Buessem, W.R. The Elastic Anisotropy of Crystals. *J. Appl. Phys.* **1967**, *38*, 2010–2012. [[CrossRef](#)]
207. Tvergaard, V.; Hutchinson, J.H. Microcracking in ceramics induced by thermal expansion or elastic anisotropy. *J. Am. Ceram. Soc.* **1988**, *71*, 157–166. [[CrossRef](#)]
208. Ravindran, P.; Fast, L.; Korzhavyi, P.A.; Johansson, B.; Wills, J.; Eriksson, O. Density Functional Theory for Calculation of Elastic Properties of Orthorhombic Crystals: Application to TiSi<sub>2</sub>. *J. Appl. Phys.* **1997**, *84*, 4891–4904. [[CrossRef](#)]
209. Ledbetter, H.; Migliori, A.A. A general elastic-anisotropy measure. *J. Appl. Phys.* **2006**, *100*, 063516. [[CrossRef](#)]
210. Lloveras, P.; Castan, T.; Porta, M.; Planes, A.; Saxena, A. Influence of Elastic Anisotropy on Structural Nanoscale Textures. *Phys. Rev. Lett.* **2008**, *100*, 165707. [[CrossRef](#)]
211. Kube, C.M. Elastic anisotropy of crystals. *AIP Adv.* **2016**, *6*, 095209. [[CrossRef](#)]
212. Ranganathan, S.I.; Ostoja-Starzewski, M. Universal Elastic Anisotropy Index. *Phys. Rev. Lett.* **2008**, *101*, 055504. [[CrossRef](#)]
213. Curtin, W.A. Theory of Mechanical Properties of Ceramic-Matrix Composites. *J. Am. Ceram. Soc.* **1991**, *74*, 2837–2845. [[CrossRef](#)]
214. Coleman, J.N.; Khan, U.; Blau, W.J.; Gun'ko, Y.K. Small but strong: A review of the mechanical properties of carbon nanotube-polymer composites. *Carbon* **2006**, *44*, 1624–1652. [[CrossRef](#)]
215. Salvetat, J.P.; Briggs, G.A.D.; Bonard, J.M.; Bacsá, R.R.; Kulik, A.J.; Stöckli, T.; Burnham, N.A.; Forró, L. Elastic and Shear Moduli of Single-Walled Carbon Nanotube Ropes. *Phys. Rev. Lett.* **1999**, *82*, 944–947. [[CrossRef](#)]
216. Kis, A.; Csányi, G.; Salvetat, J.P.; Lee, T.N.; Couteau, E.; Kulik, A.J.; Benoit, W.; Brugger, J.; Forró, L. Reinforcement of single-walled carbon nanotube bundles by intertube bridging. *Nat. Mater.* **2004**, *3*, 153–157. [[CrossRef](#)] [[PubMed](#)]
217. Beyer, T.; Day, G.M.; Price, S.L. The prediction, morphology, and mechanical properties of the polymorphs of paracetamol. *J. Am. Chem. Soc.* **2001**, *123*, 5086–5094. [[PubMed](#)]
218. Reddy, C.M.; Basavoju, S.; Desiraju, G.R. Structural basis for bending of organic crystals. *Chem. Commun.* **2005**, *2005*, 2439–2441. [[CrossRef](#)] [[PubMed](#)]
219. Reddy, C.M.; Krishna, G.R.; Ghosh, S. Mechanical properties of molecular crystals—Applications to crystal engineering. *CrytEngComm* **2010**, *12*, 2296–2314. [[CrossRef](#)]
220. Raju, K.B.; Ranjan, S.; Vishnu, V.S.; Bhattacharya, M.; Bhattacharya, B.; Mukhopadhyay, A.K.; Reddy, C.M. Rationalizing Distinct Mechanical Properties of Three Polymorphs of a Drug Adduct by Nanoindentation and Energy Frameworks Analysis: Role of Slip Layer Topology and Weak Interactions. *Cryt. Growth Des.* **2018**, *8*, 3927–3937. [[CrossRef](#)]

221. Fabbiani, F.P.A.; Pulham, C.R. High-pressure studies of pharmaceutical compounds and energetic materials. *Chem. Soc. Rev.* **2006**, *35*, 932–942. [[CrossRef](#)]
222. Fabbiani, F.P.A.; Allan, D.R.; David, W.I.F.; Davidson, A.J.; Lennie, A.R.; Parsons, S.; Pulham, C.R.; Warren, J.E. High-pressure studies of pharmaceuticals: An exploration of the behavior of piracetam. *Cryst. Growth Des.* **2007**, *7*, 1115–1124. [[CrossRef](#)]
223. Neumann, M.A.; Van de Streek, J.; Fabbiani, F.P.A.; Hidber, P.; Grassmann, O. Combined crystal structure prediction and high-pressure crystallization in rational pharmaceutical polymorph screening. *Nat. Commun.* **2015**, *6*, 7793. [[CrossRef](#)]
224. Meier, M.; John, E.; Wieckhusen, D.; Wirth, W.; Peukert, W. Influence of mechanical properties on impact fracture: Prediction of the milling behaviour of pharmaceutical powders by nanoindentation. *Powder Technol.* **2009**, *188*, 301–313. [[CrossRef](#)]
225. Karki, S.; Friščić, T.; Fábíán, L.; Laity, P.R.; Day, G.M.; Jones, W. Improving Mechanical Properties of Crystalline Solids by Cocrystal Formation: New Compressible Forms of Paracetamol. *Adv. Mater.* **2009**, *21*, 3905–3909. [[CrossRef](#)]
226. Varughese, S.; Kiran, M.S.R.N.; Solanko, K.A.; Bond, A.D.; Ramamurty, U.; Desiraju, G.R. Interaction anisotropy and shear instability of aspirin polymorphs established by nanoindentation. *Chem. Sci.* **2011**, *2*, 2236–2242. [[CrossRef](#)]
227. SeethaLekshmi, S.; Kiran, M.S.R.N.; Ramamurty, U.; Varughese, S. Molecular basis for the mechanical response of sulfa drug crystals. *Chem. Eur. J.* **2019**, *25*, 526–537. [[CrossRef](#)] [[PubMed](#)]
228. Egar, M.; Janković, B.; Lah, N.; Ilić, I.; Srčić, S. Nanomechanical properties of selected single pharmaceutical crystals as a predictor of their bulk behaviour. *Pharm. Res.* **2015**, *3*, 469–481. [[CrossRef](#)] [[PubMed](#)]
229. Azuri, I.; Meirzadeh, E.; Here, D.; Cohen, S.R.; Rappe, A.; Lahav, M.; Lubomirsky, I.; Kronik, L. Unusually Large Young's Moduli of Amino Acid Molecular Crystals. *Angew. Chem. Int. Ed.* **2015**, *54*, 13566–13570. [[CrossRef](#)]
230. Rupasinghe, T.M.; Hutchins, K.M.; Bandaranayake, B.S.; Ghorai, S.; Karunatilake, C.; Bučar, D.K.; Swenson, D.C.; Arnold, M.A.; MacGillivray, L.R.; Tivanski, A.V. Mechanical Properties of a Series of Macro- and Nanodimensional Organic Cocrystals Correlate with Atomic Polarizability. *J. Am. Chem. Soc.* **2015**, *137*, 12768–12771. [[CrossRef](#)]
231. Mohamed, M.R.; Mishra, M.K.; Al Harbi, L.M.; Al Ghamdic, M.S.; Ramamurty, U. Anisotropy in the mechanical properties of organic crystals: Temperature dependence. *RSC Adv.* **2015**, *5*, 64156–64162. [[CrossRef](#)]
232. Mishra, M.K.; Mishra, K.; Narayan, A.; Reddy, C.M.; Vangala, V.R. Structural Basis for Mechanical Anisotropy in Polymorphs of a Caffeine–Glutaric Acid Cocrystal. *Cryst. Growth Des.* **2020**, *20*, 6306–6315. [[CrossRef](#)]
233. Mishra, M.K.; Sun, C.C. Conformation Directed Interaction Anisotropy Leading to Distinct Bending Behaviors of Two ROY Polymorphs. *Cryst. Growth Des.* **2020**, *20*, 4764–4769. [[CrossRef](#)]
234. Jain, A.; Shah, H.S.; Johnson, P.R.; Narang, A.S.; Morris, K.R.; Haware, R.V. Crystal anisotropy explains structure-mechanics impact on tableting performance of flufenamic acid polymorphs. *Eur. J. Pharm. Biopharm.* **2018**, *132*, 83–92. [[CrossRef](#)] [[PubMed](#)]
235. Singaraju, A.B.; Bahl, D.; Wang, C.; Swenson, D.C.; Sun, C.C.; Stevens, L.L. Molecular Interpretation of the Compaction Performance and Mechanical Properties of Caffeine Cocrystals: A Polymorphic Study. *Mol. Pharmaceutics* **2020**, *17*, 21–31. [[CrossRef](#)] [[PubMed](#)]
236. Zhang, K.; Sun, C.C.; Liu, Y.; Wang, C.; Shi, P.; Xu, J.; Wu, S.; Gong, J. Fabrication of a microcapsule extinguishing agent with a core–shell structure for lithium-ion battery fire safety. *Chem. Mater.* **2021**, *33*, 1053–1060. [[CrossRef](#)]
237. Vaksler, Y.; Idrissi, A.; Urzhuntseva, V.V.; Shishkina, S.V. Quantum Chemical Modeling of Mechanical Properties of Aspirin Polymorphic Modifications. *Cryst. Growth Des.* **2021**, *21*, 2176–2186. [[CrossRef](#)]
238. Wang, L.; Wang, C.; Wu, S.; Fan, Y.; Li, X. Influence of the mechanical properties of biomaterials on degradability, cell behaviors and signaling pathways: Current progress and challenges. *Biomater. Sci.* **2020**, *8*, 2714–2733. [[CrossRef](#)]
239. Mitragotri, M.; Llahann, J. Physical approaches to biomaterial design. *Nat. Mater.* **2009**, *8*, 15–23. [[CrossRef](#)]
240. Jahan, A.; Ismail, M.Y.; Sapuan, S.; Mustapha, F. Material screening and choosing methods—A review. *Mater. Des.* **2010**, *31*, 696–705. [[CrossRef](#)]
241. Li, Z.; Nevitt, M.N.; Ghose, S. Elastic constants of sodalite Na<sub>4</sub>Al<sub>3</sub>Si<sub>3</sub>O<sub>12</sub>Cl. *Appl. Phys. Lett.* **1989**, *55*, 1730–1731. [[CrossRef](#)]
242. Lethbridge, Z.A.D.; Walton, R.I.; Bosak, A.; Krisch, M. Single-crystal elastic constants of the zeolite analcime measured by inelastic X-ray scattering. *Chem. Phys. Lett.* **2009**, *471*, 286–289. [[CrossRef](#)]
243. Williams, J.J.; Evans, K.E.; Walton, R.I. On the elastic constants of the zeolite chlorosodalite. *Appl. Phys. Lett.* **2006**, *88*, 021914. [[CrossRef](#)]
244. Birch, F. The Velocity of Compressional Waves in Rocks to 10 Kilobars, Part 1. *J. Geophys. Res.* **1960**, *65*, 1083–1102. [[CrossRef](#)]
245. Neighbours, J.R.; Schacher, G.E. Determination of Elastic Constants from Sound-Velocity Measurements in Crystals of General Symmetry. *J. Appl. Phys.* **1967**, *38*, 5366–5375. [[CrossRef](#)]
246. Christensen, N.I. Poisson's ratio and crustal seismology. *J. Geophys. Res.* **1996**, *101*, 3139–3156. [[CrossRef](#)]
247. Li, B.; Liebermann, R.C. Study of the Earth's Interior Using Measurements of Sound Velocities in Minerals by Ultrasonic Interferometry. *Phys. Earth Planet. Int.* **2014**, *233*, 135–153. [[CrossRef](#)]
248. Bosak, A.; Serrano, J.; Krisch, M.; Watanabe, K.; Taniguchi, T.; Kanda, H. Elasticity of hexagonal boron nitride: Inelastic x-ray scattering measurements. *Phys. Rev. B* **2006**, *73*, 041402. [[CrossRef](#)]
249. Bosak, A.; Krisch, M.; Mohr, M.; Maultzsch, J.; Thomsen, C. Elasticity of single-crystalline graphite: Inelastic x-ray scattering study. *Phys. Rev. B* **2007**, *75*, 153408. [[CrossRef](#)]
250. Diddens, I.; Murphy, B.; Krisch, M.; Müller, M. Anisotropic Elastic Properties of Cellulose Measured Using Inelastic X-ray Scattering. *Macromolecules* **2008**, *41*, 9755–9759. [[CrossRef](#)]

251. Kiefte, H.3; Breckon, S.; Penney, R.; Clouter, M. Elastic constants of ammonia by Brillouin spectroscopy. *J. Chem. Phys.* **1985**, *83*, 4738–4743. [CrossRef]
252. Bass, J.D. Elasticity of grossular and spessartite garnets by Brillouin spectroscopy. *J. Geophys. Res.* **1989**, *94*, 7621–7628. [CrossRef]
253. Bezacier, L.; Reynard, B.; Cardon, H.; Montagnac, G.; Bass, J.D. High-pressure elasticity of serpentine and seismic properties of the hydrated mantle wedge. *J. Geophys. Res. Solid Earth* **2013**, *118*, 527–535. [CrossRef]
254. Oliver, W.C.; Pharr, G.M. An improved technique for determining hardness and elastic modulus using load and displacement sensing indentation experiments. *J. Mater. Res.* **2004**, *19*, 3–20. [CrossRef]
255. Lin, J.; Shu, X.F.; Dong, J.X. The synthesis and mechanical properties of large zeolite sodalite single crystals. *Stud. Surf. Sci. Catal. A* **2005**, *158*, 231–238.
256. Brabec, L.; Bohac, P.; Stranyanek, M.; Ctvrtlik, R.; Kocirik, M. Hardness and elastic modulus of silicalite-1 crystal twins. *Microporous Mesoporous Mater.* **2006**, *94*, 226–233. [CrossRef]
257. Johnson, M.C.; Wang, J.; Li, Z.; Lew, C.M.; Yan, Y. Effect of calcination and polycrystallinity on mechanical properties of nanoporous MFI zeolites. *Mater. Sci. Eng. A* **2007**, *456*, 58–63. [CrossRef]
258. Eslava, S.; Zhang, L.; Esconjauregui, S.; Yang, J.; Baklanov, K.M.; Saiz, M.R. Metal-organic framework ZIF-8 films as low- $\kappa$  dielectrics in microelectronics. *Chem. Mater.* **2013**, *25*, 27–33. [CrossRef]
259. Zeng, Z.; Tan, J.C. AFM Nanoindentation to Quantify Mechanical Properties of Nano- and Micron-Sized Crystals of a Metal-Organic Framework Material. *ACS Appl. Mater. Interfaces* **2017**, *9*, 39839–39854. [CrossRef]
260. Boissiere, C.; Grosso, D.; Lepoutre, S.; Nicole, L.; Bruneau, A.B.; Sanchez, C. Porosity and mechanical properties of mesoporous thin films assessed by environmental ellipsometric porosimetry. *Langmuir* **2005**, *21*, 12362–12371. [CrossRef] [PubMed]
261. Devine, S.D.; Robinson, W.H. Piezoelectric method of determining mechanical properties of a small sandwich specimen at 30 to 200 kHz. *J. Appl. Phys.* **1977**, *48*, 1437. [CrossRef]
262. Woldenden, A.; Harmouche, M.R. Elastic constants of silver as a function of temperature. *J. Mater. Sci.* **1993**, *28*, 1015–1018. [CrossRef]
263. Ganesan, V.V.; Dhanasekaran, M.; Thangavel, N.; Dhathathreyan, A. Elastic compliance of fibrillar assemblies in type I collagen. *Biophys. Chem.* **2018**, *240*, 15–24. [CrossRef]
264. Kiely, E.; Zwane, R.; Fox, R.; Reilly, A.M.; Guerin, S. Density functional theory predictions of the mechanical properties of crystalline materials. *CrystEngComm* **2021**, *23*, 5697–5710. [CrossRef]
265. Chaudhuri, M.M. The deformation stress of highly brittle explosive crystals from real contact area measurements. *J. Mater. Sci.* **1984**, *19*, 3028–3042. [CrossRef]
266. Wang, Z.; Lambros, J.; Lobo, R.F. Micromechanical compressive response of a zeolite single crystal. *J. Mater. Sci.* **2002**, *37*, 2491–2499. [CrossRef]
267. Singh, A.K. X-ray diffraction from solids under nonhydrostatic compression—Some recent studies. *J. Phys. Chem. Solids* **2004**, *65*, 1589–1596. [CrossRef]
268. Singh, A.K.; Andrault, D.; Bouvier, P. X-ray diffraction from stishovite under nonhydrostatic compression to 70 GPa: Strength and elasticity across the tetragonal  $\rightarrow$  orthorhombic transition. *Phys. Earth Planet. Inter.* **2012**, *208–209*, 1–10. [CrossRef]
269. Duwal, S.; Yoo, C.S. Shear-Induced Isostructural Phase Transition and Metallization of Layered Tungsten Disulfide under Nonhydrostatic Compression. *J. Phys. Chem. C* **2016**, *120*, 5101–5107. [CrossRef]
270. Liu, B.; Lin, J.; Gao, Y.; Ma, Y.; Zhou, P.; Han, D.; Gao, C. Metallization of Molybdenum Diselenide under Nonhydrostatic Compression. *J. Phys. Chem. C* **2021**, *125*, 5412–5416. [CrossRef]
271. Day, G.M.; Price, S.L.; Leslie, M. Elastic Constant Calculations for Molecular Organic Crystals. *Cryst. Growth Des.* **2001**, *1*, 13–27. [CrossRef]
272. Han, S.S.; Goddard, W.A., III. Metal-Organic Frameworks Provide Large Negative Thermal Expansion Behavior. *J. Phys. Chem. C* **2007**, *11*, 15185–15191. [CrossRef]
273. Wan, C.; Sun, C.C. Superior Plasticity and Tabletability of Theophylline Monohydrate. *Mol. Pharm.* **2019**, *16*, 1732–1741.
274. Stixrude, L.; Cohen, R.E.; Singh, D.J. Iron at high pressure: Linearized-augmented-plane-wave computations in the generalized-gradient approximation. *Phys. Rev. B* **1994**, *50*, 6442–6445. [CrossRef] [PubMed]
275. Karki, B.; Stixrude, L.; Wentzcovitch, R.M. High-pressure elastic properties of major materials of Earth's mantle from first principles. *Rev. Geophys.* **2001**, *39*, 507–534. [CrossRef]
276. De Jong, M.; Chen, W.; Angsten, T.; Jain, A.; Notestine, R.; Gamst, A.; Sluiter, M.; Ande, C.K.; van der Zwaag, S.; Plata, J.J.; et al. Charting the complete elastic properties of inorganic crystalline compounds. *Sci. Data* **2015**, *2*, 150009. [CrossRef] [PubMed]
277. Chibani, S.; Coudert, F.X. Systematic exploration of the mechanical properties of 13621 inorganic compounds. *Chem. Sci.* **2019**, *10*, 8589–8599. [CrossRef]
278. Payne, M.C.; Teter, M.P.; Ailan, D.C.; Arias, A.; Joannopoulos, J.D. Iterative Minimization Techniques for ab Initio Total-Energy Calculations: Molecular Dynamics and Conjugate Gradients. *Rev. Mod. Phys.* **1992**, *64*, 1045–1097. [CrossRef]
279. MaterialsStudio. Available online: <https://3dsbiovia.com/products/collabo-rative-science/biovia-materials-studio/> (accessed on 15 June 2021).
280. Clark, S.J.; Segall, M.D.; Pickard, C.J.; Hasnip, P.J.; Probert, M.I.J.; Refson, K.; Payne, M.C. First principles methods using CASTEP. *Z. Kristallogr.* **2005**, *220*, 567–570. [CrossRef]

281. Perdew, J.P.; Burke, K.; Ernzerhof, M. Generalized Gradient Approximation Made Simple. *Phys. Rev. Lett.* **1996**, *77*, 3865–3868. [[CrossRef](#)]
282. Perdew, J.P.; Ruzsinszky, A.; Csonka, G.I.; Vydrov, O.A.; Scuseria, G.E.; Constantin, L.A.; Zhou, X.; Burke, K. Restoring the Density-Gradient Expansion for Exchange in Solids and Surfaces. *Phys. Rev. Lett.* **2008**, *100*, 136406. [[CrossRef](#)]
283. Grimme, S. Semiempirical GGA-type Density Functional Constructed with a Long-Range Dispersion Correction. *J. Comput. Chem.* **2006**, *27*, 1787–1799. [[CrossRef](#)]
284. Bonales, L.J.; Colmenero, F.; Cobos, J.; Timón, V. Spectroscopic Raman characterization of rutherfordine: A combined DFT and experimental study. *Phys. Chem. Chem. Phys.* **2016**, *18*, 16575–16584. [[CrossRef](#)]
285. Colmenero, F.; Bonales, L.J.; Cobos, J.; Timón, V. Density Functional Theory Study of the Thermodynamic and Raman Vibrational Properties of  $\gamma$ -UO<sub>3</sub> Polymorph. *J. Phys. Chem. C* **2017**, *121*, 14507–14516. [[CrossRef](#)]
286. Colmenero, F.; Bonales, L.J.; Cobos, J.; Timón, V. Thermodynamic and Mechanical Properties of the Rutherfordine Mineral Based on Density Functional Theory. *J. Phys. Chem. C* **2017**, *121*, 5994–6001. [[CrossRef](#)]
287. Weck, P.F.; Gordon, M.; Greathouse, J.A.; Bryan, C.E.; Meserole, S.P.; Rodriguez, M.A.; Payne, M.C.; Kim, E.J. Infrared and Raman Spectroscopy of  $\alpha$ -ZrW<sub>2</sub>O<sub>8</sub>: A Comprehensive Density Functional Perturbation Theory and Experimental Study. *J. Raman Spectrosc.* **2018**, *49*, 1373–1384. [[CrossRef](#)]
288. Colmenero, F.; Plášil, J.; Sejkora, J. The crystal structures and mechanical properties of the uranyl carbonate minerals roubaultite, fontanite, sharpite, widemannite, grimselite and čejkaite. *Inorg. Chem. Front.* **2020**, *7*, 4197–4221. [[CrossRef](#)]
289. Colmenero, F. Thermodynamic properties of the uranyl carbonate minerals roubaultite, fontanite, widemannite, grimselite, čejkaite and bayleyite. *Inorg. Chem. Front.* **2020**, *7*, 4160–4179. [[CrossRef](#)]
290. Colmenero, F.; Timón, V. Mechanical anomalies in mercury oxalate and the deformation of the mercury cube coordination environment under pressure. *Appl. Phys. A* **2021**, *127*, 395. [[CrossRef](#)]
291. Troullier, N.; Martins, J.L. Efficient Pseudopotentials for Plane-Wave Calculations. *Phys. Rev. B* **1991**, *43*, 1993–2006. [[CrossRef](#)]
292. Pfrommer, B.G.; Cote, M.; Louie, S.G.; Cohen, M.L. Relaxation of Crystals with the Quasi-Newton Method. *J. Comput. Phys.* **1997**, *131*, 233–240. [[CrossRef](#)]
293. Downs, R.T.; Bartelmehs, K.L.; Gibbs, G.V.; Boisen, M.B. Interactive software for calculating and displaying X-ray or neutron powder diffractometer patterns of crystalline materials. *Am. Mineral.* **1993**, *78*, 1104–1107.
294. Nye, J.F. *Physical Properties of Crystals*; Clarendon: Oxford, UK, 1976.
295. Yu, R.; Zhu, J.; Ye, H.Q. Calculations of Single-Crystal Elastic Constants Made Simple. *Comput. Phys. Commun.* **2010**, *181*, 671–675. [[CrossRef](#)]
296. Nielsen, O.H.; Martin, R.M. Quantum-mechanical theory of stress and force. *Phys. Rev. B* **1985**, *32*, 3780–3791. [[CrossRef](#)] [[PubMed](#)]
297. Colmenero, F.; Bonales, L.J.; Cobos, J.; Timón, V. Structural, mechanical and vibrational study of uranyl silicate mineral soddyite by DFT calculations. *J. Solid. State Chem.* **2017**, *253*, 249–257. [[CrossRef](#)]
298. Colmenero, F.; Bonales, L.J.; Timón, V.; Cobos, J. Structural, mechanical and Raman spectroscopic characterization of the layered uranyl silicate mineral, uranophane- $\alpha$ , by density functional theory methods. *Clay Miner.* **2018**, *53*, 377–392. [[CrossRef](#)]
299. Colmenero, F.; Cobos, J.; Timón, V. Periodic Density Functional Theory Study of the Structure, Raman Spectrum, and Mechanical Properties of Schoepite Mineral. *Inorg. Chem.* **2018**, *57*, 4470–4481. [[CrossRef](#)] [[PubMed](#)]
300. Colmenero, F.; Fernández, A.M.; Cobos, J.; Timón, V. Becquerelite mineral phase: Crystal structure and thermodynamic and mechanical stability by using periodic DFT. *RSC Adv.* **2018**, *8*, 24599–24616. [[CrossRef](#)]
301. Colmenero, F.; Plášil, J.; Sejkora, J. The layered uranyl silicate mineral uranophane- $\beta$ : Crystal structure, mechanical properties, Raman spectrum and comparison with the  $\alpha$ -polymorph. *Dalton Trans.* **2018**, *48*, 16722–16736. [[CrossRef](#)]
302. Colmenero, F.; Plášil, J.; Cobos, J.; Sejkora, J.; Timón, V.; Čejka, J.; Bonales, L.J. Crystal structure, hydrogen bonding, mechanical properties and Raman spectrum of the lead uranyl silicate monohydrate mineral kasolite. *RSC Adv.* **2019**, *9*, 15323–15334. [[CrossRef](#)]
303. Colmenero, F.; Plášil, J.; Cobos, J.; Sejkora, J.; Timón, V.; Čejka, J.; Fernández, A.M.; Petříček, V. Structural, mechanical, spectroscopic and thermodynamic characterization of the copper-uranyl tetrahydroxide mineral vandenbrandeite. *RSC Adv.* **2019**, *9*, 40708–40726. [[CrossRef](#)]
304. Colmenero, F.; Plášil, J.; Němec, I. Uranosphaerite: Crystal structure, hydrogen bonding, mechanics, infrared and Raman spectroscopy and thermodynamics. *J. Phys. Chem. Solids* **2020**, *141*, 109400. [[CrossRef](#)]
305. Colmenero, F.; Plášil, J.; Škácha, P. The magnesium uranyl tricarbonat octadecahydrate mineral, bayleyite: Periodic DFT study of its crystal structure, hydrogen bonding, mechanical properties and infrared spectrum. *Spectrochim. Acta A* **2020**, *234*, 118216. [[CrossRef](#)]
306. Colmenero, F.; Plášil, J.; Timón, V.; Čejka, J. Full crystal structure, hydrogen bonding and spectroscopic, mechanical and thermodynamic properties of mineral uranopilite. *RSC Adv.* **2020**, *10*, 31947–31960. [[CrossRef](#)]
307. Colmenero, F. Anomalous mechanical behavior of the deltic, squaric and croconic cyclic oxocarbon acids. *Mater. Res. Express* **2019**, *6*, 045610. [[CrossRef](#)]
308. Colmenero, F. Mechanical properties of anhydrous oxalic acid and oxalic acid dihydrate. *Phys. Chem. Chem. Phys.* **2019**, *21*, 2673–2690. [[CrossRef](#)] [[PubMed](#)]
309. Colmenero, F. Negative area compressibility in oxalic acid dihydrate. *Mater. Lett.* **2019**, *245*, 25–28. [[CrossRef](#)]

310. Colmenero, F. Organic acids under pressure: Elastic properties, negative mechanical phenomena and pressure induced phase transitions in the lactic, maleic, succinic and citric acids. *Mater. Adv.* **2020**, *1*, 1399–1426. [[CrossRef](#)]
311. Colmenero, F.; Cobos, J.; Timón, V. Negative linear compressibility in uranyl squarate monohydrate. *J. Phys. Cond. Matter.* **2019**, *31*, 175701. [[CrossRef](#)]
312. Colmenero, F.; Timón, V. Extreme negative mechanical phenomena in the zinc and cadmium anhydrous metal oxalates and lead oxalate dihydrate. *J. Mater. Sci.* **2020**, *55*, 218–236. [[CrossRef](#)]
313. Colmenero, F. Silver oxalate: Mechanical properties and extreme negative mechanical phenomena. *Adv. Theor. Simul.* **2019**, *2*, 1900040. [[CrossRef](#)]
314. Colmenero, F.; Jiang, X.; Li, X.; Li, Y.; Lin, Z. Negative area compressibility in silver oxalate. *J. Mater. Sci.* **2021**, *56*, 269–277. [[CrossRef](#)]
315. Baroni, S.; Giannozzi, P.; Testa, A. Elastic Constants of Crystals from Linear-Response Theory. *Phys. Rev. Lett.* **1987**, *59*, 2662–2665. [[CrossRef](#)]
316. Wu, X.; Vanderbilt, D.; Hamann, D.R. Systematic treatment of displacements, strains, and electric fields in density-functional perturbation theory. *Phys. Rev. B* **2005**, *72*, 035105. [[CrossRef](#)]
317. Wentzcovitch, R.M.; Wu, Z.Q.; Carrier, P. Thermodynamic properties and phase relations in mantle minerals investigated by first principles quasiharmonic theory. *Rev. Mineral. Geochem.* **2010**, *71*, 99–128. [[CrossRef](#)]
318. Wu, Z.Q.; Wentzcovitch, R.M. Quasiharmonic thermal elasticity of crystals: An analytical approach. *Phys. Rev. B* **2011**, *83*, 184115. [[CrossRef](#)]
319. Parrinello, J.; Rahman, A. Strain fluctuations and elastic constants. *J. Chem. Phys.* **1982**, *76*, 2662–2666. [[CrossRef](#)]
320. Ray, J.R. Comput. Ensembles and Computer Simulation Calculation of Response Functions. *Phys. Rep.* **1988**, *8*, 109–152.
321. Wojciechowski, K.W.; Tretiakov, K.V. Quick and accurate estimation of the elastic constants using the minimum image method. *Comp. Phys. Commun.* **1999**, *121–122*, 528–530. [[CrossRef](#)]
322. Van Workum, K.V.; De Pablo, J. Local elastic constants in thin films of an fcc crystal. *Phys. Rev. E* **2003**, *67*, 011505. [[CrossRef](#)]
323. Voyiatzis, E. Mechanical properties and elastic constants of atomistic systems through the stress-fluctuation formalism. *Comput. Phys. Commun.* **2013**, *184*, 27–33. [[CrossRef](#)]
324. Marmier, A.; Lethbridge, Z.A.D.; Walton, R.I.; Smith, C.; Parker, S.C.; Evans, K.E. ELAM: A computer program for the analysis and representation of anisotropic elastic properties. *Comput. Phys. Commun.* **2010**, *181*, 2102–2115. [[CrossRef](#)]
325. Lowenstein, W. The distribution of aluminum in the tetrahedra of silicates and aluminates. *Am. Mineral.* **1954**, *39*, 91–96.
326. Davis, M.E.; Hathaway, P.E.; Montes, C. Zeolites and molecular sieves: Not just ordinary catalysts. *Zeolites* **1980**, *9*, 436–439. [[CrossRef](#)]
327. Voigt, W. *Lehrbuch der Kristallphysik*; Teubner: Leipzig, Germany, 1962.
328. Reuss, A.Z. Berechnung der Fließgrenze von Mischkristallen auf Grund der Plastizitätsbedingung für Einkristalle. *Angew. Math. Mech.* **1929**, *9*, 49–58. [[CrossRef](#)]
329. Hill, R. The Elastic Behaviour of a Crystalline Aggregate. *Proc. Phys. Soc. Lond. A* **1952**, *65*, 349–354. [[CrossRef](#)]
330. Weck, P.F.; Kim, E.; Buck, E.C. On the mechanical stability of uranyl peroxide hydrates: Implications for nuclear fuel degradation. *RSC Adv.* **2015**, *5*, 79090–79097. [[CrossRef](#)]
331. Colmenero Ruiz, F. Theoretical Studies of the Structural, Mechanic and Raman Spectroscopic Properties of Uranyl Containing Minerals. In *Minerals*; Essa, K.S., Ed.; InTechOpen: London, UK, 2018; Chapter 4; pp. 65–94.
332. Angel, R.J. Equations of State. *Rev. Mineral. Geochem.* **2000**, *41*, 35–60. [[CrossRef](#)]
333. Lacivita, V.; D’Arco, P.; Mustapha, S.; Bernardes, D.F.; Dovesi, R.; Erba, A.; Rérat, M. Ab initio compressibility of metastable low albite: Revealing a lambda-type singularity at pressures of the Earth’s upper mantle. *Phys. Chem. Miner.* **2020**, *47*, 45. [[CrossRef](#)]
334. Evans, K.E. Auxetic polymers: A new range of materials. *Endeavour* **1991**, *15*, 170–174. [[CrossRef](#)]
335. Colmenero, F.; Sejkora, J.; Plášil, J. Crystal Structure, Infrared Spectrum and Elastic Anomalies in Taperssuatsiaite. *Sci. Rep.* **2020**, *10*, 7510. [[CrossRef](#)]
336. Baughman, R.H.; Fonseca, A.F. Straining to expand entanglements. *Nat. Mater.* **2015**, *15*, 7–8. [[CrossRef](#)] [[PubMed](#)]
337. Bryukhanov, I.A.; Rybakov, A.A.; Larin, A.V.; Trubnikov, D.N.; Vercauteren, D.P. The role of water in the elastic properties of aluminosilicate zeolites: DFT investigation. *J. Mol. Model.* **2017**, *23*, 68. [[CrossRef](#)] [[PubMed](#)]
338. Coasne, B.; Haines, J.; Levelut, C.; Cambon, O.; Santoro, M.; Gorelli, F.; Garbarino, G. Enhanced mechanical strength of zeolites by adsorption of guest molecules. *Phys. Chem. Chem. Phys.* **2011**, *13*, 20096–20099. [[CrossRef](#)] [[PubMed](#)]
339. Mouhat, F.; Bousquet, D.; Boutin, A.; du Bourg, L.B.; Coudert, F.X.; Fuchs, A.H. Softening upon Adsorption in Microporous Materials: A Counterintuitive Mechanical Response. *J. Phys. Chem. Lett.* **2015**, *6*, 4265–4269. [[CrossRef](#)] [[PubMed](#)]
340. Canepa, P.; Tan, K.; Du, Y.; Lu, H.; Chabal, Y.J.; Thonhauser, T. Structural, elastic, thermal, and electronic responses of small-molecule-loaded metal–organic framework materials. *J. Mater. Chem. A* **2015**, *3*, 986–995. [[CrossRef](#)]
341. Hu, Y.; Navrotsky, A. Thermochemical Study of the Relative Stability of Dense and Microporous Aluminophosphate Frameworks. *Chem. Mater.* **1995**, *7*, 1816–1823. [[CrossRef](#)]
342. Navrotsky, A.; Petrovic, I.; Hu, Y.; Chen, C.Y.; Davis, M.E. Little energetic limitation to microporous and mesoporous materials. *Microporous Mater.* **1995**, *4*, 95–98. [[CrossRef](#)]
343. Boldyreva, E. High-Pressure Polymorphs of Molecular Solids: When Are They Formed, and When Are They Not? Some Examples of the Role of Kinetic Control. *Cryst. Growth Des.* **2007**, *7*, 1662–1668. [[CrossRef](#)]

344. Henson, N.J.; Cheetham, A.K.; Gale, J.D. Computational Studies of Aluminum Phosphate Polymorphs. *Chem. Mater.* **1995**, *8*, 664–670. [[CrossRef](#)]
345. Fabbiani, M.; Polisi, M.; Fraisse, B.; Arletti, R.; Santoro, M.; Alabarse, F.; Haines, J. An in-situ x-ray diffraction and infrared spectroscopic study of the dehydration of AlPO<sub>4</sub>-54. *Solid State Sci.* **2020**, *108*, 106378. [[CrossRef](#)]
346. Bennett, J.M.; Cohen, J.P.; Flanigen, E.M.; Pluth, J.J.; Smith, J.V. Aluminophosphate molecular sieve AlPO<sub>4</sub>-11: Partial refinement from powder data using a pulsed neutron source. *ACS Symp. Ser.* **1983**, *218*, 109–118. [[CrossRef](#)]
347. Richardson, J.M.; Pluth, J.J.; Smith, J.V. Structure determination and rietveld refinement of aluminophosphate molecular sieve AlPO<sub>4</sub>-8. *Acta Crystallogr. C* **1987**, *43*, 1469–1472. [[CrossRef](#)]
348. Ohnishi, N.; Qiu, S.; Teresaki, O.; Kajitani, T.; Hiraga, K. Hexagonal-orthorhombic phase transformation of AlPO<sub>4</sub>-5 aluminophosphate molecular sieve. *Microporous Mater.* **1993**, *2*, 73–74. [[CrossRef](#)]
349. Ikeda, T.; Miyazawa, K.; Izumi, F.; Huang, Q.; Santoro, A.J. Structural study of the aluminophosphate AlPO<sub>4</sub>-5 by neutron powder diffraction. *J. Phys. Chem. Solids* **1999**, *60*, 1531–1535. [[CrossRef](#)]
350. Polisi, M.; Arletti, R.; Quartieri, S.; Pastero, L.; Giacobbe, C.; Vezzalini, G. Dehydration mechanism of AlPO<sub>4</sub>-5: A high-resolution synchrotron X-ray powder diffraction study. *Microporous Mesoporous Mater.* **2018**, *261*, 137–143. [[CrossRef](#)]
351. Xu, J.; Liu, Y.; Huang, Y.J. Ultrafast crystallization of AlPO<sub>4</sub>-5 molecular sieve in a deep eutectic solvent. *Phys. Chem. C* **2021**, *125*, 8876–8889. [[CrossRef](#)]
352. Xu, J.; Chen, L.; Zeng, D.; Yang, J.; Zhang, M.; Ye, C.; Deng, J. Solid-state NMR of silicoaluminophosphate molecular sieves and aluminophosphate materials. *J. Phys. Chem. B* **2007**, *111*, 7105–7113. [[CrossRef](#)]
353. Fan, F.; Feng, Z.; Sun, K.; Guo, W.; Guo, Q.; Song, Y.; Li, W.; Li, C. In situ UV Raman spectroscopic study on the synthesis mechanism of AlPO-5. *Angew. Chem. Int. Ed.* **2009**, *121*, 8899–8903. [[CrossRef](#)] [[PubMed](#)]
354. Shi, Y.; Liu, G.; Wang, L.; Zhang, X. Ionothermal synthesis of phase pure AlPO<sub>4</sub>-5 using a series of tri-substituted imidazolium bromides. *Microporous Mesoporous Mater.* **2014**, *193*, 1–6. [[CrossRef](#)]
355. Chen, B.; Kirby, C.W.; Huang, Y. Investigation of Crystallization of Molecular Sieve AlPO<sub>4</sub>-5 by the Dry Gel Conversion Method. *J. Phys. Chem. C* **2009**, *113*, 15868–15876. [[CrossRef](#)]
356. Sheng, N.; Chu, Y.; Xin, S.; Wang, Q.; Yi, X.; Feng, Z.; Meng, X.; Liu, X.; Deng, F.; Xiao, F.S. Microwave Assisted Green Synthesis, Characterisation of Alanine Templated Aluminophosphate Zeolite and Study of Its Application as Adsorbent. *J. Am. Chem. Soc.* **2016**, *138*, 6171–6176. [[CrossRef](#)]